PONTIFICIA UNIVERSIDAD CATÓLICA DEL PERÚ

Escuela de Posgrado

ON THE FUNDAMENTAL ABSORPTION OF EXCITONIC AND NON-EXCITONIC SEMICONDUCTORS: An Optoelectronic and Thermal Approach

Tesis para obtener el grado académico de Doctor en Física que presenta:

Kevin Angello Lizárraga Olivares

Asesor:

Prof. Dr. Jorge Andrés Guerra Torres

Jurado:

Prof. Dr. Francisco De Zela

Prof. Dr. Leandro Tessler

Dr. Lars Korte

Dr. Florian Ruske

Lima, 2023

Informe de Similitud

Yo, Jorge Andrés Guerra Torres, docente de la Escuela de Posgrado de la Pontificia Universidad Católica del Perú, asesor(a) de la tesis titulada *On the fundamental absorption of excitonic and non-excitonic semiconductors: an optoelectronic and thermal approach*, del autor Kevin Angello Lizárraga Olivares,

dejo constancia de lo siguiente:

- El mencionado documento tiene un índice de puntuación de similitud de 12%. Así lo consigna el reporte de similitud emitido por el software *Turnitin* el 19/07/2023.

- He revisado con detalle dicho reporte y la Tesis o Trabajo de Suficiencia Profesional, y no se advierte indicios de plagio.

- Las citas a otros autores y sus respectivas referencias cumplen con las pautas académicas.

Lima, 24/07/2023

……………………………………………………………………………………..

Jorge Andrés Guerra Torres	
DNI: 46163725	Firma
ORCID: 0000-0002-1734-6660	

I pour my heart out in dedicating this work to my family, who has been my constant source of inspiration and support. My mother, whose unwavering belief in me has propelled me to strive for the impossible. My father, whose unwavering dedication and love have guided me through every step of this journey. My sisters, whose boundless empathy has been a beacon of light during the most challenging of times. And, to my closest friends, whose insightful conversations about the mysteries of the universe and the depths of humanity have enriched my life beyond measure. This work is a testament to their unwavering love and support, and for that, I am forever grateful.

Acknowledgements

I humbly extend my deepest gratitude to my cherished friends and collaborators, without whom the fruition of this project would have remained unattainable. Their unwavering support and guidance have been instrumental in navigating through the uncharted territories of this research endeavor. Furthermore, I am indebted to them for their invaluable contributions, which have expanded my knowledge beyond the scope of this thesis.

I would like to express my sincere appreciation to Msc. P. Llontop, for his insightful discussions regarding the potential applicability of the models presented in this thesis, applied to perovskites and TCO's. To Msc. L. A. Enrique, for his active role in testing new models on excitonic materials. To Msc. A. Tejada, for his contribution in familiarizing me with the ellipsometry technique and the SpectraRay software. To Msc. M. Piñeiro, for his collaborations on TCO materials, a topic that surpasses the scope of this thesis. To Msc. E. Serquen, for his work and insightful discussions on site locations on rare earths, as well as his instruction in techniques such as photoluminescence and Raman scattering.

I am also grateful to Msc. E. Perez, for his involvement in the development of the models and his collaboration on the effective mass project. To Msc. L. Sanchez and Msc. F. Bravo, for their thought-provoking discussions on chemical and material synthesizing techniques like magnetron sputtering. To Msc. E. Ventura and Msc. A. Dávila, for entrusting me with the honor of advising and guiding them in their master thesis projects, which relate to thermal-optical properties and amorphous silicon simulations.

To Dr. L. Korte, for his assistance and insightful discussions in the development of the ongoing papers. Finally, I would like to extend my profound appreciation to Dr. A. Guerra, for his exceptional guidance and leadership through the topics that were in line with my interests. His immeasurable support, empathy, and enthusiasm in advising, not only on physics-related topics, but also in real-life situations are a true testament to his remarkable character. I am indebted to his trust in completing the PhD position, and his unwavering friendship, which I hope will endure long after the completion of this work.

Abstract

In the present work, we study the optical properties of semiconductors near the fundamental absorption taking into account disorder induced tail states. In particular, we pay special attention to GaAs and lead halide perovskites. We address existing models for the description of the absorption spectra, and extend them in the band fluctuations framework. We start with traditional semiconductors where we have developed our models inspired in Jellison-Modine procedure (Tauc-Lorentz model). These models are tested on direct, indirect and amorphous bandgap materials such as the ones of the group $III - V$ family. Later, we continue the discussion with the inclusion of the Sommerfeld enhancement factor for understanding the nature of excitonic semiconductors. Here, the Elliott model is modified through the band fluctuations procedure in order to obtain an analytic expression for the imaginary part of the electrical permittivity. This new model accurately describes the bandgap and binding energy of systems like GaAs, MAPbBr$_3$, MAPbI$_3$ and MAPbI$_{3-x}$Cl$_x$. Furthermore, the impact of the sample temperature on optical parameters such as the bandgap can provide information regarding the thermal expansion and the electron-phonon interaction in the solid. In particular, if the material exhibits a high electron-phonon coupling, like in the cases of the polar semiconductors, the model describing the exciton can no longer rely on the Hydrogen-like picture, but instead it must be computed with a theory considering exciton-polarons. In the latter case, the exciton is dressed by a cloud of phonons that lower its binding energy. Remarkably, our model for excitonic materials correctly predicts the exciton-polaron binding energies of lead halide perovskites and their carrier's effective masses. Lastly, we emphasize the powerful relation between the optical properties and the thermal properties. Notably, we found a good agreement among our predicted expressions, using the Debye's model, with other specific heat experimental results.

Key Words: Electrical permittivity, fundamental absorption, binding energy, exciton, phonon, polaron, band fluctuations, disorder, semiconductors, GaAs, InP, cSi, aSi, GaP, MAPbBr$_3$, MAPbI$_3$ and MAPbI$_{3-x}$Cl$_x$.

Table of contents

List of figures

List of tables

Chapter 1

Introduction

The primary goal of this thesis is to modify and extend current models that describe the optical properties of the different types of semiconductors. The reasons for the proposal of new models are, for instance, the lack of a model for the absorption edge of direct transitions materials, the determination of the Urbach tail, the shape of the absorption in high energy regions, and, the absence of an analytical expression for the absorption of excitonic materials.

I begin with the proposal of new models for the direct, indirect, and amorphous materials that accurately describe the fundamental and high absorption regions. These new models are inspired on the Tauc-Lorentz model, and, they are named accordingly as Ullrich-Lorentz, O'Leary-Lorentz, Band-Fluctuations-Lorentz (BFL) and Monolog-Lorentz.

The second stage of my project was to modify the Elliott's absorption model for excitonic materials. The new model follow the approach of the band-fluctuations model, producing an analytical expression that describes the discrete excitonic peak and continuum states observed in the absorption edge. This model is named as Elliott-Band-Fluctuations (EBF) and it was tested in tri-halide perovskite systems with great success.

The third stage of my research was devoted to model electronic and thermal properties of the semiconductors using the optical parameters obtained from the EBF model. Electronic properties such as the effective mass were calculated by inverting the Kane's model [73]. Whilst for the thermal properties, a description using the Debye's theory was used to grasp the concepts of specific heat, internal energy, Helmholtz free energy and entropy. Remarkably, our results are aligned with several reports, thus, suggesting an strong relation between the optical and electronic/thermal properties.

1.1   Optical Properties of Solids

The significance of the interaction between light and matter has been recognized for centuries, dating back to the use of precious metals for trade to nowadays the utilization of rubies and sapphires in high power solid state lasers [39]. In the past, reflection and transmission were the most intriguing optical properties, utilized in the form of mirrors made of metals and glasses to gauge object transparency.

Today, we possess a deeper understanding of these optical properties. We now comprehend that metals appear shiny due to the presence of free carriers, that glasses, commonly, are made of fused silica SiO_2, and that rubies and sapphires have the same composition of aluminum oxide, Al_2O_3, with impurities that give them their distinct colors. Mathematical description of optical properties began with Maxwell in the mid-1800s, as his equations enabled the expression of these properties in terms of electric and magnetic fields, allowing us to conceive the idea that these fields interact with ions, electrons, vibrations, and electronic density dislocations within materials.

Materials exhibit unique behaviors under the influence of light, which depend on their composition and stoichiometry. They can be classified into glasses, metals, insulators, and semiconductors. In the following we describe briefly some properties of each group of materials to later focus our attention in semiconductors.

The unique amorphous nature of glasses is what gives them their characteristic properties. Glasses have found new applications in the fiber industry. When glasses are doped with other materials or contain impurities, they can acquire different properties. For instance, when a semiconductor with a bandgap in the visible range is added during the deposition of fused silica, the resulting glass will exhibit enhanced reflectivity, as seen in the case of stained glass [39].

Metals manifest an exceptional degree of reflectance across the visible and infrared regions, below the plasma frequency located in the ultraviolet range. This trait arises from the polarization of free charges which obstructs the transmission of light within the medium. The abundance of free charges in metals enhances their electrical conductivity [29]. This feature is harnessed by the industry to produce, for instance, wires and gadgets. Additionally, their remarkable mechanical characteristics allow them to be extensively employed in the manufacturing of diverse structures, such as airplanes, vehicles, and machinery.

Insulators, in contrast to metals, possess a bandgap that separates the conduction and valence bands. This bandgap is so large that neither visible light nor thermal effects are capable of inducing excitations. For this reason, the main application of insulators is to control electrical breakdown phenomena. When the bandgap decreases in size, the line between an insulator and semiconductor becomes blurred. For instance, a mechanism for

electric transport, known as hopping, gets activated. This mechanism refers to the act of an excitation, such as an exciton, jumping across unit cells due to the tight binding nature of the material [39].

In particular, semiconductors are highly attractive for a wide range of modern technological applications. They exhibit transport properties that can be activated optically and thermally, even at room temperature. These unique features have made them the foundation of modern electronic and photovoltaic devices. One of the most prominent examples is silicon (Si), which is abundant, versatile, has a tunable bandgap, and exhibits solid nature in an oxygen atmosphere with a 4-bond structure that allows for high conductivity. This has enabled the development of an array of technologies for doped silicon, including transistors, integrated circuits, solar cells, silicones (silicon-oxygen polymers), sand (silica), clay (aluminium silicate), lasers (SiC), engine blocks, and machine tools (aluminium silicon and ferro silicon) [113].

There are a plethora of theories developed to understand the behavior of the aforementioned materials. These theories include fluid-based models for glasses, the free electron gas theory for metals, and the damped oscillator theory for semiconductors and insulators [65, 48, 29]. However, numerous other theories also exist, which explore the interactions between atoms and their surroundings. Although I have an insatiable desire to learn about all materials, this dissertation will specifically focus on the extensively researched category of semiconductors.

1.2   Semiconductors

In this section, we shall expound on the various classifications of semiconductors and outline the materials that were employed in this research. However, prior to delving into the subject matter, we must emphasize the rationale behind the need to explore alternative compounds to silicon, despite its status as one of the most superior semiconductors, as previously mentioned. The solution to this quandary is rooted in optoelectronics since silicon alone is very inefficient when emitting light due to the indirect nature of its bandgap. As a result, other types of semiconductors with direct bandgaps were sought after, leading to the discovery of diverse families such as the III-V and II-VI semiconductors, as depicted in Figure 1.1.

In the taxonomy of semiconductors, there exist elemental and compound classifications. The former comprises semiconductors located in groups III, IV, and V of the periodic table, such as the indirect bandgap elements silicon (Si) and germanium (Ge). On the other hand, compound semiconductors are further subdivided into binary, ternary, and quaternary compounds. The electronic orbitals of the atoms dictate that group III and V semiconductors
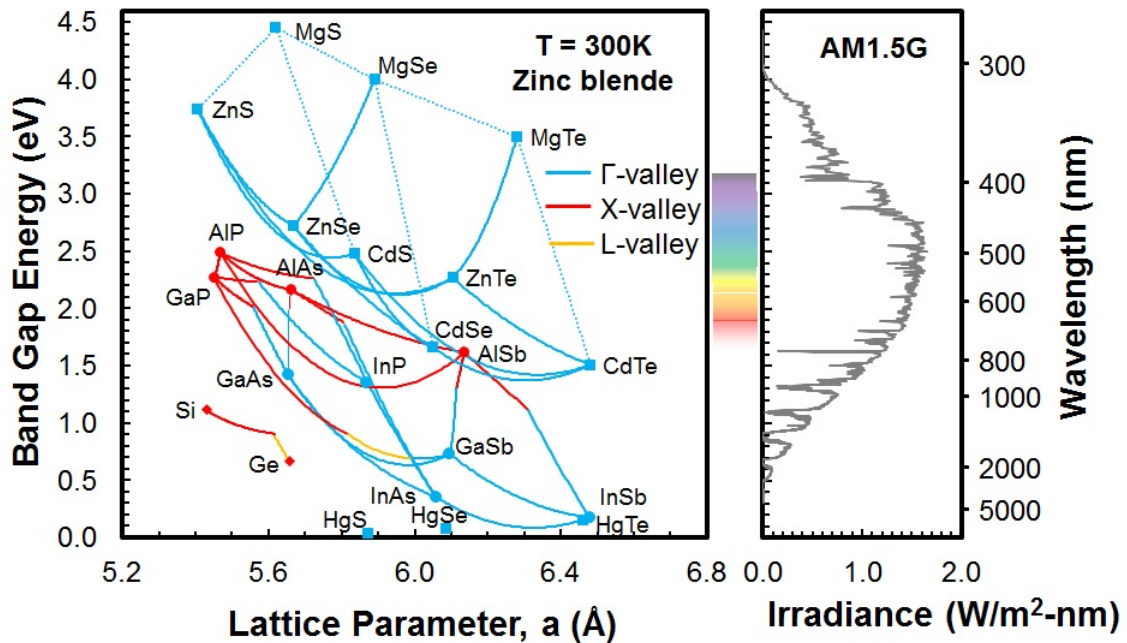
Fig. 1.1 Figure on the left shows the different bandgap values for the families of III-V and II-VI semiconductors plotted versus their lattice constant. Sky-blue lines and marks show direct transition materials (Γ-valley), while red and yellow represent indirect transitions (X and L - valley). The curved lines represent the change of the bandgap when stoichiometry changes. The right side of the image shows the standard solar spectrum irradiance (AM1.5G). From these two images, we can deduce that the desired material for PV technology would be a material that has small bandgap and behaves as direct transition material. This figures were extracted from [112].

can form covalent bonds, much like group II and VI. Examples of the former include gallium nitride (GaN), gallium arsenide (GaAs), indium phosphide (InP), and aluminum arsenide (AlAs), while the latter encompasses cadmium telluride (CdTe) and zinc selenide (ZnSe). Figure 1.1 illustrates the evolution of the bandgap versus the lattice constant for these families in the zinc blende structure. Direct semiconductors are depicted by sky blue lines, while indirect ones are represented by red and yellow colors. Group IV elements also form binary compounds, such as silicon carbide (SiC) or silicon germanium (SiGe). Lastly, larger compounds can be formed by manipulating the stoichiometry of the system. Examples of such compounds are aluminum gallium arsenide ($Al_xGa_{1-x}As$) and gallium indium arsenic phosphide ($Ga_xIn_{1-x}As_{1-y}P_y$) for ternary and quaternary compounds, respectively.

The optoelectronic applications of these semiconductors encompass a wide range of devices including light emitting diodes (LEDs), phototransistors, lasers, and solar cells (photodiodes). Despite the abundance of semiconductors with different bandgaps, only a

select few are economically viable and competitive in the ever-expanding market. Theories describing the properties of these semiconductor families are classified based on the type of interaction involved, namely electronic and vibrational processes. The former pertains to intraband and interband absorption, while the latter describes the interaction with vibrations or phonons.

The second chapter of this work will explore the models that explain interband transitions, mainly applied to the III-V semiconductor family. Additionally, within the electronic processes category, the phenomena of excitons, which are formed when electrons and holes interact, presents an interesting aspect. Materials with excitonic properties exhibit greater efficiencies in photo-current density, different transport mechanisms, and have inspired solar cells based on them [55]. Some examples of exciton-bearing materials include GaAs [158, 140], CdTe [140], ZnSe [140], perovskites [4], and organic compounds [55].

Perovskites refer to materials possessing a crystal structure of ABX_3. These materials have garnered considerable attention in photovoltaic technology due to their remarkable features such as excitonic absorption, low-cost production, tunable bandgap, and efficient carrier recombination. Apart from photovoltaic technology, perovskites are also employed in various applications including catalysis, fuel cells, electrochemical sensing, and piezoelectrics. The perovskite family based on methylammonium lead halide is particularly noteworthy due to its visible range bandgap and high efficiency in photovoltaics, which can reach up to 25% [200]. Despite their many advantages, perovskites are prone to instability resulting from defects and impurities during the preparation process and when exposed to humidity and atmospheric conditions. Therefore, studies on perovskite materials are ongoing.

One interesting characteristic of perovskites is their polar nature, which arises from the ionicity of the cores. The ionic fields of perovskites polarize the vibrations, causing a quasiparticle known as a polaron to form. In Chapter 3 and 4, we analyze the models relating to absorption caused by excitons and polarons, exploring their relevance to perovskite compounds.

In the subsequent section, we present a comprehensive discussion of the different optical phenomena in semiconductors, following the classification system outlined in [39] based on electronic and electron-phonon processes.

1.3   Electronic Processes

In semiconductors, the electromagnetic interactions between electrons and photons can be classified into two principal types: interband absorption and exciton formation. These

phenomena will be examined in the following discussion, followed by a brief analysis of the dielectric models that will be examined in chapters 2 and 3 to conclude this section.

1.3.1   Interband Absorption

In semiconductors, when photons of energy comparable to the bandgap are absorbed, this results in a conduction that arises not from the free carriers, but from optically excited ones. Photons excite electrons from occupied states in the valence band to unoccupied states in the conduction band, leaving behind a hole of positive electric charge with an effective mass equivalent to the curvature of the valence band. These transitions can be classified as direct or indirect depending on the assistance of a phonon. Direct transitions occur on the same k-vector of the Brillouin zone, whilst indirect transitions occur between different points in k-space as seen in figure 1.2a. Remarkably, the momentum of light is neglected in both transitions since the crystal momentum is approximately 1000 times larger than the wave vector of the photon [29].

The direct and indirect character of the fundamental transition can be directly analyzed through the band structure. Experimental studies, such as Angle Resolved Photoemission Spectroscopy (ARPES), reveal the Conduction Band Minimum (CBM) and the Valence Band Maximum (VBM), whose provide an accurate description of the bandgap [87]. Moreover, Density Functional Theory (DFT), which is based on first-principles calculations, offers a more detailed understanding of the band shape and spin-orbit coupling of the system. A comparison between both techniques is illustrated in Figure 1.2.

Transitions of high energy are dependent upon the disparity in energy levels between the conduction (c) and valence (v) bands, as well as the level of coupling between them, which is known as the dipole momentum matrix element, represented as $|\langle v| \hat{p} |c\rangle|^2$. This term depends on the symmetry of the transition and is a result of the Fermi's Golden Rule for the Coulomb interaction.

The described interband absorption can be studied by modeling the electrical permittivity. The theoretical models use an integration over the energy and the Joint Density Of States (JDOS) to model the imaginary part of the electrical permittivity. And, by using the Kramers-Kroning relations, one can obtain the real part of it [204]. The comparison of the data shape of the theoretical and experimental results provide us information about the energy bands at specific points in the Brillouin zone [29]. It is important to remark that the JDOS of our systems is of a 3D case, however, for other dimensionalities, such as 2D and 1D, the optical absorption will change. And, some properties like the exciton binding energy can be favored by this dimensional reduction due to the confinement effects [29].
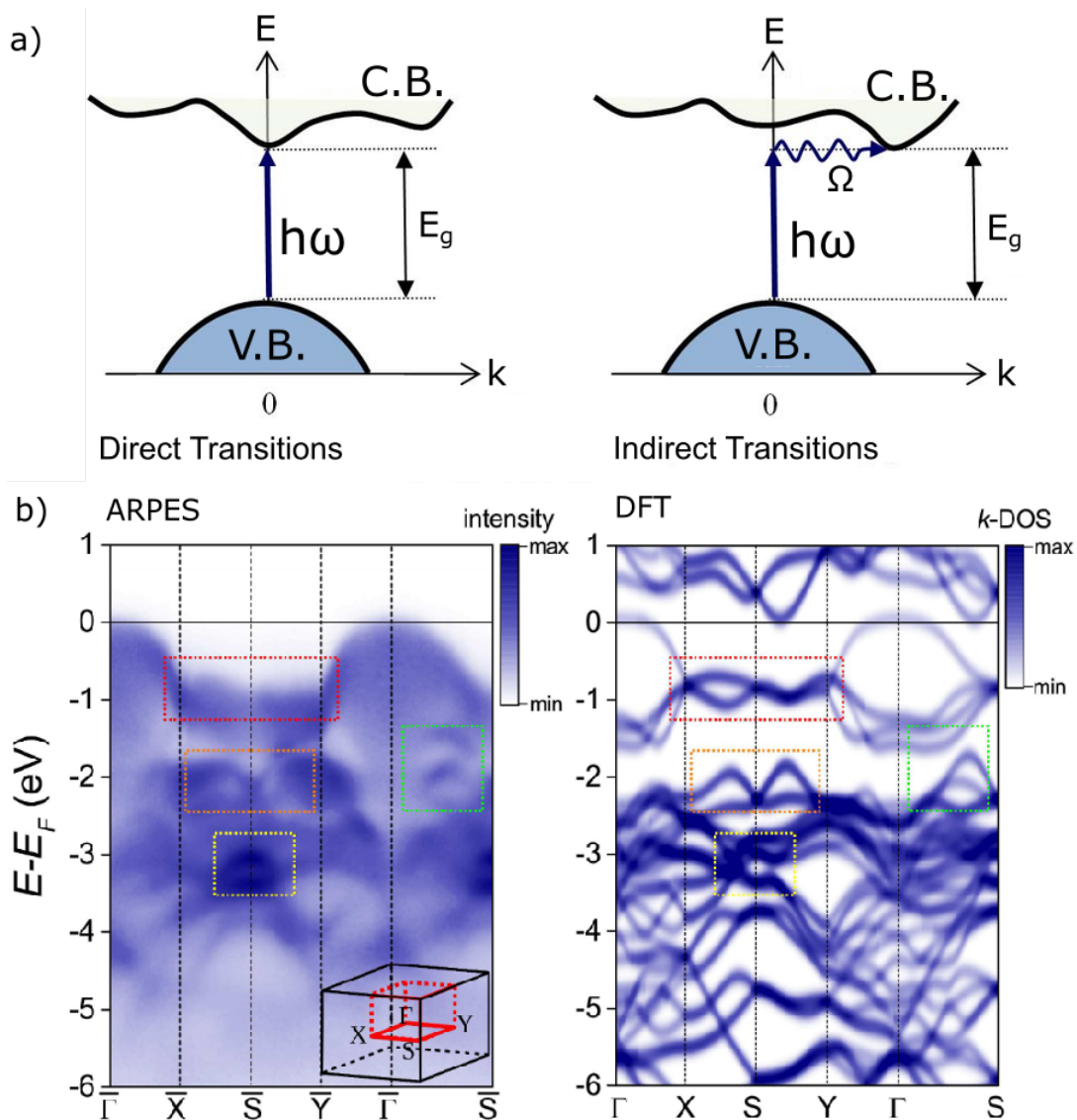
Fig. 1.2 Illustration of the direct and indirect interband absorption processes from the valence band (V.B.) to the conduction band (C.B.). bandgap is denoted by E_g, while the phonon momentum for indirect transitions is denoted by Ω. This figure was adapted from [208] (a). Band-structure obtained from the experimental technique Angle Resolved Photoemission Spectroscopy (ARPES) and the theoretical calculation obtained from first principles of $PdSe_2$ for comparison purposes. This image was adapted from [18] (b)

1.3.2 Excitons

Excitons are quasi-particles formed by a hole and an electron, attracted to each other by the Coulomb interaction. This attractive force arises when an electron in the valence band is excited to the conduction band, leaving behind a hole which the electron then is attracted to. The formation of excitons is dependent on the properties of the material and can result in

bound states, where the hole and electron are tightly coupled, or unbound states, where they are more widely separated.

The size of excitons can vary from extending over many unit cells to being confined to a single unit cell. The former, known as Wannier-Mott excitons, are typically found in semiconductors and have a small binding energy of $1 - 10$ meV. On the other hand, the latter, known as Frenkel excitons, are more characteristic of molecular or insulator systems and possess a higher binding energy of $0.1 - 1$ eV. These Frenkel excitons can be created by the interaction of free excitons with defects, resulting in states similar to hydrogen molecules with large binding energy. Despite their localized nature, Frenkel excitons can be transported through the lattice by hopping, as seen in molecular systems that use this mechanism to transport energy over long distances. One such example is the Davydov soliton, which is an exciton packet propagating along the protein α-helix self-trapped amide I [23].

Excitons are a fascinating phenomenon, however, the focus of this thesis is directed towards the free excitons known as Wannier-Mott excitons, which have the ability to move unrestrictedly throughout the crystal. The absorption in such systems is calculated with Fermi's golden rule applied to the simplest system of two opposite charges, the hydrogen atom wave functions. After the computation of the absorption, the Coulomb interaction, known as Sommerfeld enhancement factor, is observed to augment the absorption, as depicted in figure 1.3-c. This enhancement of absorption could augments the performance of the solar cell if the charges can be separated. For this reason, the presence of excitons holds paramount significance in contemporary photovoltaic technology. Furthermore, the energy levels of excitons are crucial in LEDs and lasers at low temperatures [29].

Device performance is suceptible to the temperature, where the phonon energy corresponds to $k_\beta T$. This implies that when phonons interact with excitons, they tend to dissociate them if the binding energy of the exciton is not greater than the thermal energy. However, if the binding energy is of the same order, then excitons remain stable at room temperature [39]. Thus, organic compounds and insulators are more likely to possess stable excitons at room temperature.

1.3.3   Optical experiments

Optical absorption and dispersion measurements can be conducted via two methods: spectrophotometry and spectroscopic ellipsometry. Spectrophotometry involves measuring the intensities of incident and reflected/transmitted light and analyzing the proportion of these to estimate the absorption coefficient of the system. In contrast, spectroscopic ellipsometry measures changes in the polarization of the incident light beam, which is a result of various phenomena such as reflection and transmission [48]. This polarization is then modeled by
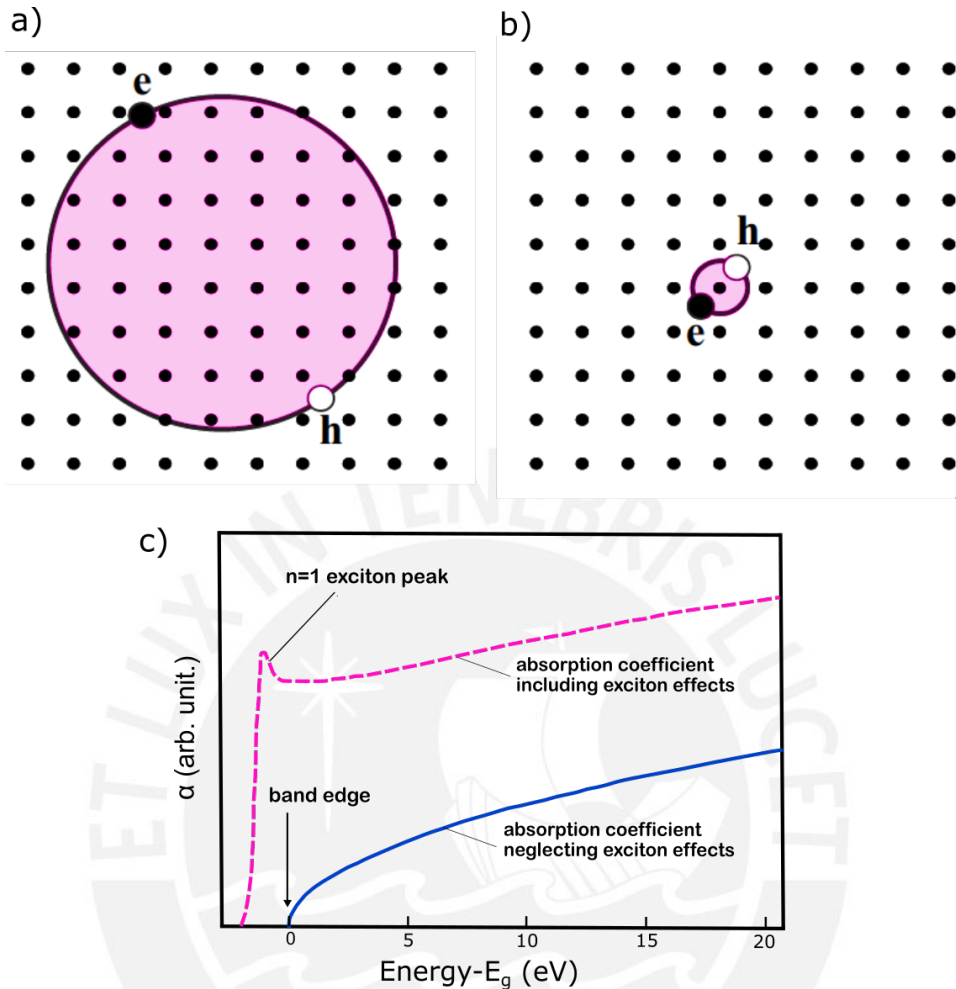
Fig. 1.3 Representation of a Wannier-Mott exciton which covers several unit cells and has lower binding energy (a). The tightly bound Frenkel exciton of the size of an unit cell (b). Figures (a) and (b) were adapted from [207]. Optical absorption is presented for cases when the excitonic effects are included (pink dashed line), and when neglecting them (blue line). Here, the band edge was located at zero and the first excitonic peak appears below it (c). This figure was reconstructed from [109]

constructing a system of the different layers of the material, allowing for the absorption to be determined.

Both methods have their own unique set of advantages and disadvantages. Spectophotometry is more straightforward in terms of data analysis, whereas ellipsometry requires a complete model for each material. Nonetheless, ellipsometry boasts higher precision and enables real-time measurements, including those related to thin-film growth and thermal oxidation [48]. Once the measurement is determined by either method, it is crucial to establish

an appropriate model for the electrical permittivity in order to derive quantities such as the bandgap, Urbach energy, exciton binding energy, and oscillator strengths.

Optical models for determining material parameters vary based on the spectral region of interest. For example, for the transparent region of the dielectric function, characterized by a near-zero ε_2 value, Sellmeier or Cauchy models are employed [48]. Free-carrier absorption, on the other hand, is preferably described by the Drude model or its variants [48], while the Tauc-Lorentz [165] and Cody-Lorentz [37] models are commonly utilized for the visible and UV regions. In the case of excitonic materials, the Elliott and Tanguy models [32, 207] are often employed. Despite the relative success of these models in estimating material parameters, such as the bandgap, they often display inconsistencies and impractical procedures when describing absorption globally. For example, the Tauc-Lorentz model can lead to a biased bandgap estimate due to the absence of Urbach tails, while the piecewiese expression of the Cody-Lorentz model can make it challenging to fit, in addition, both models are defined for amorphous and indirect materials only. The non-analyticity of the Elliott model can also result in significant computation times. Thus, the core of my work lays on developing models for a universal description of absorption coefficient near the absorption edge and higher absorption regions.

1.4 Phonon Processes

Phonons are quasiparticles resulting from the quantization of mechanical vibrations in a solid. Modes of vibration have resonant energies in the infrared absorption region and are segregated into acoustical (3) and optical branches ($3N - 3$, where N is the number of atoms in the unit cell). The former is of a mechanical nature, whereas the latter is connected with the polarization states of the crystal. For example, the sound velocity can be calculated from the dispersion relation of the acoustical branch near the Γ point. Moreover, depending on the type of vibrations, they can be categorized as transversal or longitudinal. By applying the Raman and Brillouin scattering techniques one can measure the frequencies of these phonons. In these methods, the scattering of light is measured by the excitation of the material following the incidence of light. Optical modes directly interact with light, and are commonly referred to as IR (or Raman) active. Furthermore, their selection rules can be theoretically derived by group theory. The polarization of optical phonons is evident in these setups, which allows for a deeper exploration of the phonon-photon states.

The phonon-photon interaction can be readily observed in the dispersion relations presented in figure 1.4. The linear dispersion of light in a given medium, denoted as $v = c/n$, intersects with the transverse-optical (TO) and longitudinal optical (LO) phonon branches.
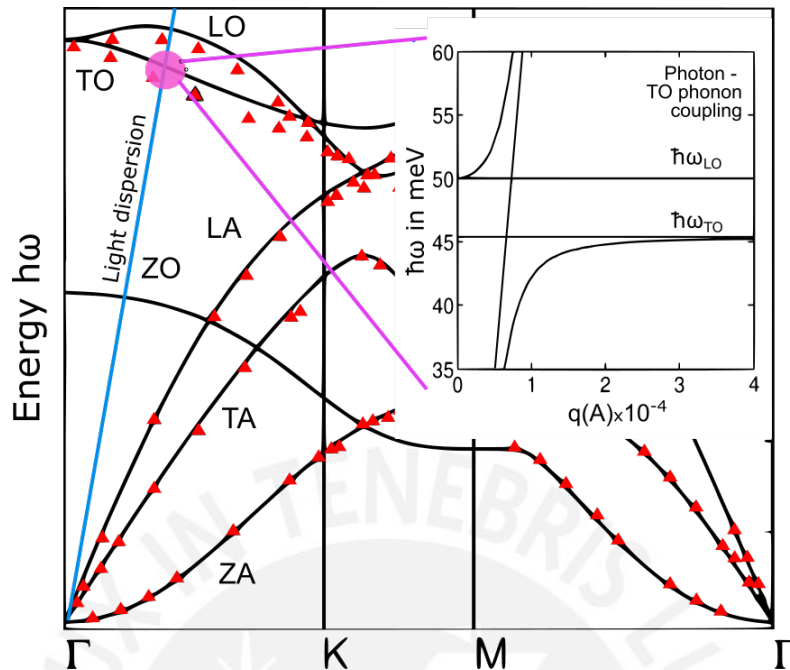
Fig. 1.4 Figure of an example of the phonon band structure. In this case, the the graphene were used as an example due to its detailed image resolution. Here the label "A" denotes the acoustical branches, while "O" denotes the optical ones. In addition, the dispersion of photons are shown as a blue line intersecting the TO branch. The crossing circle shown as magenta represent the new polariton state of the coupling. The inset enlarge this zone and show the actual dispersion relation of the polariton state. There is a forbidden band representing the zone for inaccessible states. This figure was adapted from references [70, 123]

However, only the TO phonons, due to their transverse nature, are capable of coupling with light. This intersection of the TO phonon and photon frequencies creates a quasiparticle state, commonly referred to as polariton. The dispersion thus consists of two polariton branches, as shown in the inset of figure 1.4. Notably, a forbidden gap emerges between the energies of the $\hbar\omega_{TO}$ and $\hbar\omega_{LO}$ phonons, implying that light cannot propagate in the media within this range of energies. Here, the lattice is saturated by the absorption of a large amount of light, resulting in total reflection [39]. Polar materials, which are typically composed of ionic crystals, exhibit this property with a strikingly high degree of reflection in the infrared region, particularly when the frequency approaches the transverse-optical (TO) phonon mode. The disparity in charges of the ions constituting the material permits it to become polarized in the presence of light, resulting in an asymmetric deformation of the electron clouds and consequent formation of "poles", or polar bonds. The interaction between phonons and photons is responsible for this lattice polarization, which is a manifestation of the interaction between particles. Moreover, the deformation of the lattice can interact with electrons to

give rise to polarons [39]. Further elaboration on the properties of polar materials will be provided in the subsequent section.

1.5 Polar Semiconductors

In this section, we briefly review on the classical model of a polar solid to grasp the mechanism of lattice polarization. We shall also provide a concise description of the interaction between lattice polarization and electrons/excitons. As previously mentioned, the hallmark of polar materials is their pronounced reflection in the infrared range, resulting from the saturation of light absorption by the lattice. This renders transmittance measurements meaningless for bulk materials in this energy range. However, if the dimensionality is reduced, the effect is mitigated, and light can pass through the material [39, 29]. Therefore, to comprehend these materials, it is necessary to develop a model that accounts for the high reflectivity in the forbidden gap.

The theory that describes the interaction between TO phonons and light is known as the semi-classical oscillator model. This model considers a system composed of a linear chain of unit cells that oscillate in the x and y directions, while the propagating wave moves in the z direction and interacts with a light wave (see figure 1.5-a). When the vibration wave and light wave have the same wave vector, resonance occurs. So, the problem is reduced to describe the motion of the displaced ions in the electromagnetic field of the liht wave (which for our convenience will be purely electrical). It's worth noting that at the LO phonon frequency, the motion of positive and negative ions is in opposite directions [39]. In terms of equations, this reads as:

$$m_+\frac{dx_+^2}{dt^2} = -k(x_+ - x_-) + qE(t) \tag{1.1}$$

$$m_-\frac{dx_-^2}{dt^2} = -k(x_- - x_+) - qE(t) \tag{1.2}$$

Here, m_+ and m_- are the masses of the two ions, k is the restoring constant of the medium, and $E(t)$ is the electric field of light. Also, the electric charge, $\pm q$, corresponds to the positive and negative ions, respectively. These equations can be expressed in terms of the reduced mass, $\mu = m_+ m_-/(m_+ + m_-)$, and the relative displacement of the ions, $x = x_+ - x_-$. As a consequence, the equation for the center of mass is:

$$\frac{d^2x}{dt^2} + \omega_{TO}^2 x = \frac{q}{\mu}E(t) \tag{1.3}$$
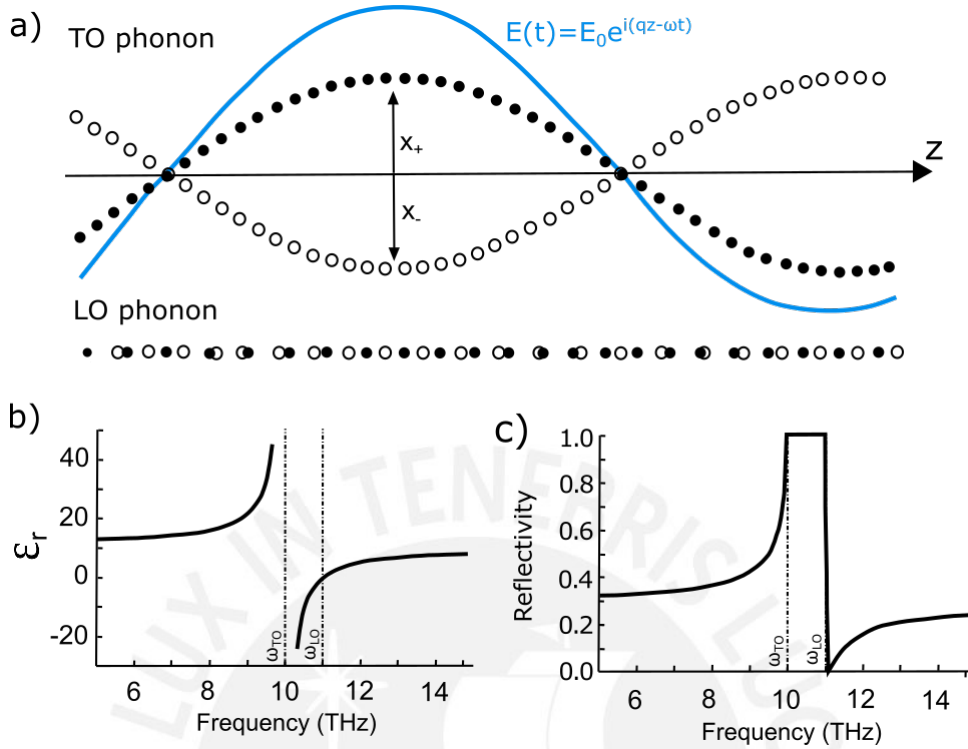
Fig. 1.5 Oscillations of the ions in the transversal and longitudinal optical modes. Phonon waves are propagating in the zth direction for both cases. In this case the transversal oscillations couple with light wave when they have the same frequency (a). Dielectric constant of polar/ionic materials is plotted in the infrared region. The dielectric constant is zero at the *LO* phonon frequency, while it diverges at the *TO* phonon frequency (b) [39]. Reflectivity of polar/ionic semiconductors which present values of 1 in the "restrahlen" band, meaning that no light can penetrate the material (c). These figures were reconstructed from reference [39]

Here the vibrational frequency, ω_{TO}^2 is K/μ, and $E(t)$ is the external electric field. Eq. 1.3 represents the undamped scenario, however, if the phonon lifetime is taken into consideration, a damping term, γ, proportional to the velocity of the relative displacement between ions included, i.e.,

$$\frac{d^2x}{dt^2} + \gamma\frac{dx}{dt} + \omega_{TO}^2 x = \frac{q}{\mu}E(t) \tag{1.4}$$

For the oscillatory electric field, $E(t) = E_0 e^{i\omega t}$, the solutions of this equation are well known in optics and can be found in Mark et al. [39] and Fujiwara et al. [48] under the name of the Lorentz model for a system of electrons that oscillates in a medium of low density. The result is written as:

$$\varepsilon_r(\omega) = 1 + \chi + \frac{Nq^2}{\varepsilon_0\mu}\frac{1}{\omega_{TO}^2 - \omega^2 - i\gamma\omega} \tag{1.5}$$

Here, N is the number of unit cells per unit volume, ε_0 is the vacuum permittivity, and χ is the non resonant susceptibility of the medium. Eq. 1.5 can be compacted by writing the static and high frequency dielectric constants, ε_s and ε_∞, respectively, i.e.,

$$\varepsilon_s = \varepsilon_r(\omega = 0) = 1 + \chi + \frac{Nq^2}{\varepsilon_0 \mu \omega_{TO}^2}, \tag{1.6}$$

and,

$$\varepsilon_{\omega=\infty} = \varepsilon_r(\infty) = 1 + \chi. \tag{1.7}$$

Hence, we are left with:

$$\varepsilon_r(\omega) = \varepsilon_\infty + (\varepsilon_s - \varepsilon_\infty)\frac{\omega_{TO}^2}{(\omega_{TO}^2 - \omega^2 - i\gamma\omega)} \tag{1.8}$$

It is worth noting that the dielectric constant at infinity corresponds to frequencies that are higher than the phonon resonance frequency, ω_{LO}, but lower than the natural frequency of electronic processes in the UV/VIS range. The dielectric function is plotted in figure 1.5-b, where the zero value at the energy of ω_{LO} is evident, along with the asymptotic growth of the resonance peak at the energy of ω_{TO}, and the negative values in the "restrahlen" band, the forbidden band between ω_{TO} and ω_{LO}. The reflectivity is also calculated from the dielectric constant, as shown in figure 1.5-c, which displays the high value between the transversal and longitudinal phonon frequencies.

    The point where the dielectric function is zero is named as longitudinal due to the wave behavior. Ordinarily, the values of ε are non-zero, which satisfies the condition of $k \cdot E = 0$ [39]. However, when ε becomes zero, the wave vector k and electric field E are no longer perpendicular. As a result, longitudinal waves are allowed [39]. In summary, the coupling of transverse oscillations of photons and TO phonons, leads to the polarization of unit cells in a transverse orientation for all frequencies except at ω_{LO}, where the polarization becomes longitudinal. A useful outcome of this model is the connection between TO and LO phonon energies through the Lyddane-Sachs-Teller (LST) relationship [39], given by:

$$\frac{\omega_{LO}^2}{\omega_{TO}^2} = \frac{\varepsilon_s}{\varepsilon_\infty}. \tag{1.9}$$

The relationship expressed in Equation 1.9 indicates that non-polar crystals have degenerate LO and TO phonon branches. In these materials, the LST factor is equal to one, implying that both LO and TO frequencies are the same at Γ, but they diverge as the crystal vector increases.

Having discussed lattice polarization, we can now turn our attention to the role of electrons in polar semiconductors.

1.5.1 Polarons

Polarization of the lattice can occur via many different processes, the aforementioned mechanism involving light is just one of them. In addition, thermal effects can activate the phonon modes to produce distortions as well. Likewise, electric currents can create alterations in the charge distribution, by attracting positive ions and repelling negative ones, a process that ends in a polarized crystal structure [29].

Phonons act as energy packets that are transmitted through the vibrations of ions in the cell, allowing the system's energy to increase or decrease. This means that they can be absorbed and emitted by electrons. And, in the weak coupling, this electron-phonon interaction is commonly known in literature as the Fröhlich interaction.

The picture of the electron-phonon interaction is presented in figure 1.6a. This figure describes the electron propagation through the polarized lattice. The electron's electric field creates a polarization of the phonons that will accompany the electron as it moves. This electron is dressed by the virtual phonons by constantly absorbing and emitting them, forming a new crystal excitation known as polaron [39, 29, 75]. Since the ions displacement is in the same direction as the electric field of the electron, we expect that LO phonons form the strongest coupling [39]. Of course, this idea is supported by the theoretical considerations, in which the TO phonons contribute less than LO ones due to its smaller electric field [76].

The electron-phonon interaction is present in polar and ionic semiconductors. The larger the ionicity of the system, the higher the strength of the electron-phonon interaction. This strength is measured in terms of the Fröhlich coupling constant α [46]. This interaction depends primarily on the band mass of the electron, the effective dielectric constant and the LO phonon energy. Polaronic effects increase when we pass from the III-V semiconductor family to the I-VII compound in the periodic table.

Formation of polarons can significantly affect measurements of the electron band mass and optical properties. In fact, experiments that measure the curvature of electron bands are actually measuring the effective mass of polarons rather than the rigid lattice value. For example, in GaAs, these effects can change the electron mass by 1%, while in AgCl, the difference can be as high as 50% [39]. In addition, the measurement of the optical bandgap shows a reduction due to the binding energy of the polaron, given by:

$$\Delta E_g = -\alpha \hbar \omega_{LO}.$$
(1.10)
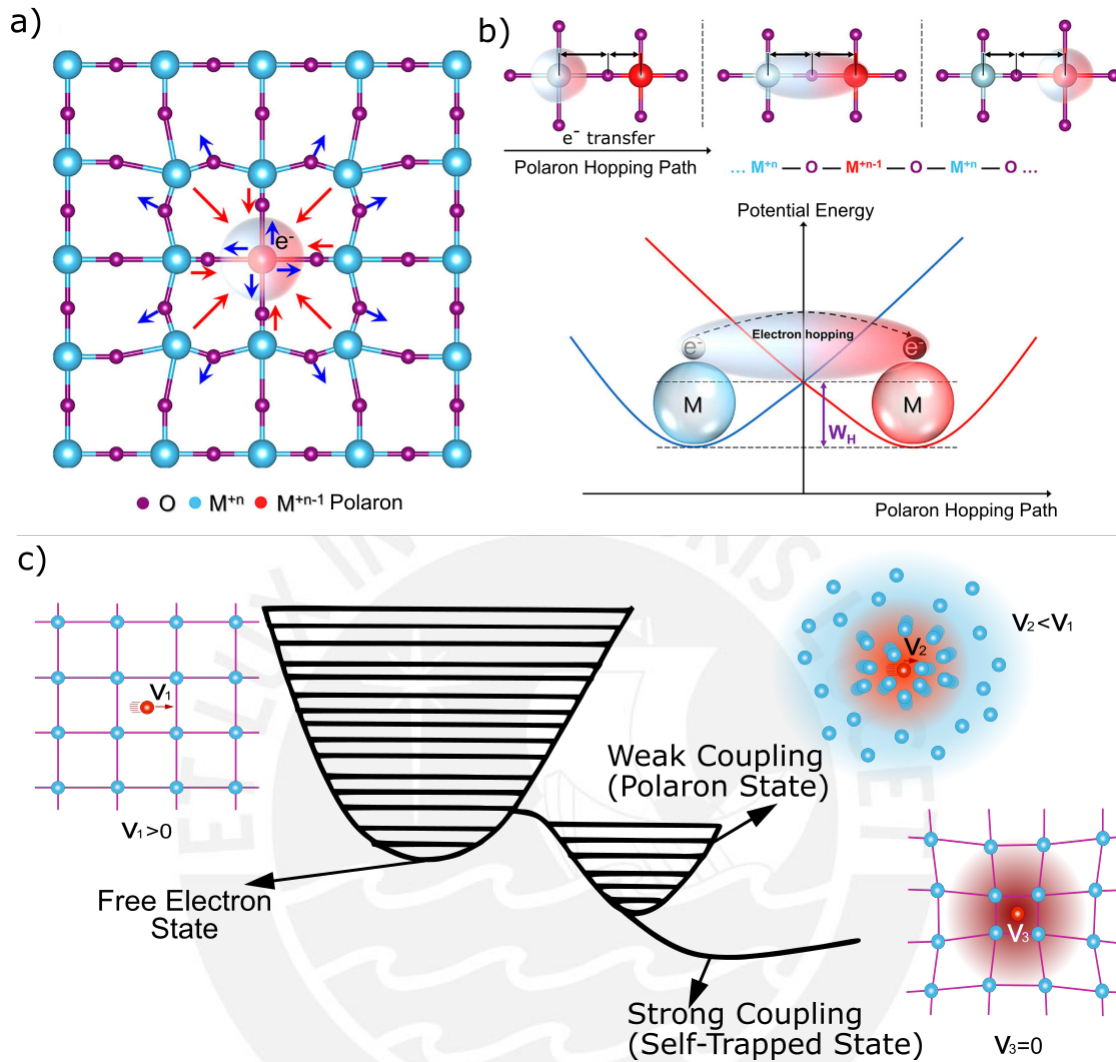
Fig. 1.6 Representation of a polaron state where the electron and the lattice are interacting through the electron-phonon coupling (a). Polaron transport in the lattice through hopping mechanism (b). Different regimes of the electron-phonon coupling. The free state is when electron does not deform the lattice and therefore have plenty of states available. In the weak coupling (polaron state), the electron moves with a cloud of virtual phonons and its mass increases, thus diminishing its velocity and states available. Lastly, in the strong coupling regime the polaron is self trapped by the lattice distortions and the only mechanism of moving is by hopping (c). Figures (a) and (b) were adapted from [106], and figure (c) from [151]

In certain situations, the impact of polaron effects on a material can result in a distinctive absorption shape that resembles a "belly" near the bandgap. This phenomenon is typically approximated using a Gaussian model [138]. One potential application of this characteristic is to introduce doping into the material to create various polaron binding energies and thereby modify the bandgap according to specific design requirements.

The magnitude of this excitation has a crucial impact on the performance of the device. Specifically, if the polaron is localized or extends across multiple unit cells, it directly influences the charge transport mechanism. The polaron radius, which is determined by the band mass of the electron and the LO phonon energy [39], is given by:

$$r_p = \left(\frac{\hbar}{2m_e^* \omega LO} \right)^{1/2}.$$ (1.11)

Large polarons with sizes of $r_p = 4$ nm and 3.1 nm are present in GaAs and ZnSe, respectively [39]. These sizes are larger than the unit cell, and thus can be described in terms of the polarizable continuum medium in the weak regime of the electron-phonon coupling. However, in materials such as AgCl and alkali halides, where the Fröhlich coupling constant α is larger than 6, the size of the polaron is comparable to the unit cell, and carriers can become trapped by their own lattice deformation as seen in figure 1.6c. This figure shows the reduction of the electronic states as a consequence of the different strengths of the electron-phonon coupling. Movement of this self-trapped state is commonly known as hopping transport (see figure 1.6b). Actually, this is the mechanism behind the room-temperature charge transport in organic semiconductors. The radius of these small polarons cannot be calculated using Eq. 1.11, and first principles techniques must include additional terms such as self-energies. In the strong regime of electron-phonon coupling, the attractive interaction between electrons exchanging phonons can lead to the formation of Cooper pairs, which are responsible for superconductive states.

As we have seen, the electron-phonon interaction is involved in various phenomena exhibited by polar materials. These include charge transport, photoemission, absorption, thermoelectricity, and colossal magnetoresistance [40]. These effects have implications for a range of devices, such as redefining the Shockley-Queisser limit of a solar cell based on these materials through photoemission, modifying the current density in photovoltaic devices through charge transport, and affecting the thermoelectric activation mechanisms in organic-based devices. Additionally, the coupling of polarons with excitons can influence hetero-junctions involved in exciton dissociation mechanisms in excitonic solar cells [55, 4].

1.5.2 Exciton-Polarons

Polarons formed by the interaction between electrons and holes can combine through the Coulomb interaction to form exciton-polaron bound states. This interaction involving electrons, holes, and LO phonons has been studied using perturbation theory by Wang [187], Green's function methods by Shindo [149], and variational calculations by Pollamnn, Buttner,

Kane, and others [61, 125, 73]. One of the main effects of this interaction is the increase in the exciton binding energy, which depends on the lattice distortion through the LO phonon energy, the effective dielectric constant, and the effective masses of the electron and hole. This dependence helps us understand the low exciton binding energies observed in polar materials like halide perovskite systems based on methylammonium, formamidinium, or cesium.

As we have seen, in situations where the interaction is strong, excitons can become localized on the atom site where they are created, resulting in a large effective mass due to phonon scattering. These excitons, similar in definition to Frenkel excitons, move through the lattice via a hopping mechanism and can modify the transport properties of the material. They possess large binding energies and exhibit stability at room temperature. Actually, there exists a transition from the Wannier-Mott exciton to the Frenkel type. This critical aspect of the electron-phonon interaction is still not well understood and is a topic of ongoing research.

In this work, we have chosen polar materials such as perovskites for optical measurements to investigate the impact of the electron-phonon coupling. I use spectral measurements reported in literature and data base libraries for our analysis. Chapters 3 and 4 present theories on the mathematical models employed to describe these phenomena.

1.6   Thermal Properties

Thermal properties of semiconductor deals with electron and phonon processes. In this case, both of them experience scattering processes, so their behaviors depend on the availability of carriers and on their scattering rates [29]. For instance, the thermal energy of the system is dissipated by the electron scattering to reach the equilibrium state. During this process, electron collisions occur. They collide with impurities, phonons, defects, boundaries and other electrons scattering events [29].

Phonon processes can be divided in harmonic and anharmonic. The former consider non interacting phonons and give rise to the specific heat as a result of the increase phonon population. A theoretical description of this mechanism has been done by Einstein and Debye [27]. On the contrary, anharmonic effects consider the scattering via phonon-phonon and are responsible for the thermal expansion and thermal conductivity. Thermal expansion causes many effects on the properties of materials since it increases the lattice constant and so the atom separation. Nevertheless, there exist materials in which the expansion coefficient is negative, and so the lattice contracts. In addition, the inclusion of thermal effects is responsible of the crystal phase transition observed in some perovskite materials.

The dependence on temperature of many properties such as the dielectric constant, resistance, electrical and thermal conductivity are important for device applications. For instance, optical properties such as the bandgap and exciton absorption broadening vary with the material's temperature following the internal contributions of the linear thermal expansion and electron-phonon coupling. In fact, one could use the thermal evolution of optical measurements to estimate the expansion coefficient and the strength of the electron-phonon coupling. It is also possible to estimate the Debye's energy and compute thermodynamic potentials.

The specific heat, internal energy, Helmholtz free energy, and entropy are thermal quantities of interest for the purpose of this thesis. In chapter 4, these concepts will be retrieved from the temperature dependent optical measurements for both GaAs and halide perovskites.

The specific heat is the amount of energy necessary to increase the temperature of the system by $1K$. It is temperature dependent and follows the Debye's model where at low temperature behaves proportional to T^3, and for large temperatures as the Dulong Petit limit. This quantity is measured in labortories by using a calorimeter, for instance, the Fast Differential Scanning Calorimetry (FDSC) measures the flow of heat in a sample as function of temperature, allowing physical phase transitions and chemical reactions to be effectively quantified.

The internal energy, U, is usually described as the energy necessary to form a system. It quantifies the energy contained by the internal constituents of the sample. This includes the energy in form of translations, rotations, vibrations (phonons), and forces binding atoms such as chemical bonds. Measurements of internal energy can be done thanks to the thermodynamic relation between this quantity and the specific heat at constant volume.

The Helmholtz free energy, F, gives the effective work you can get from a closed thermodynamic system at constant volume and temperature. Both, internal energy and Helmholtz free energy are illustrated in figure 1.7. There we found as well the Enthalpy, H, and Gibbs free energy, G, which are thermodynamic potentials obtained by adding the mechanical work (necessary to create the system) to the internal energy or the Helmholtz free energy, respectively. Changes in Enthalpy measure the heat absorbed or emitted by a process at constant pressure, while changes in the Gibbs function quantifies the maximum reversible work obtained from the system.

Finally, entropy is a physical property that quantifies the degree of randomness or disorder in a system. Consequently, the thermal energy associated with entropy per unit temperature cannot be utilized to perform useful work [28]. This is because work arises from ordered molecular motion. Conservation of energy and entropy allows us to determine which

$$-TS \longrightarrow$$

$$+PV \downarrow$$

U	$F_{=U-TS}$
Internal Energy	Helmholtz Free Energy
U=Energy needed to create a system	F=Energy needed to create a system minus the energy you can get from the environment
$H_{=U+PV}$	$G_{=U+PV-TS}$
Enthalpy	Gibbs Free Energy
H=Energy needed to create a system plus the work needed to make room for it	G=Total energy needed to create a system and make room for it minus the energy you can get from the environment

Fig. 1.7 Illustrative diagram of the thermodynamic potentials: The internal energy, U, Helmholtz free Energy, F, Enthalpy, H, and Gibbs Free Energy, G. It can be seen that the Helmholtz and Gibbs function can be obtained from the internal energy and enthalpy by diminishing the energy from the environment, TS. Enthalpy and Gibbs free energy can be computed if the work, to make room for a system, PV, is added to the internal and Helmholtz energy, respectively. This figure was reproduced from [107]

processes are feasible. If energy is conserved, but the entropy change is not, then the process is deemed irreversible and cannot be performed. This concept is mathematically expressed in the second law of thermodynamics, which is dependent on temperature. As temperature increases, the disorder of the system increases, resulting in an increase in entropy.

1.7 Thesis Structure

Chapter 2 starts with an investigation related to the evolution of the imaginary component of the dielectric constant ($\tilde{\varepsilon}_2$). $\tilde{\varepsilon}_2$ is analyzed for the fundamental region and high-energy transition region. Here, I describe novel absorption models developed in this work for direct, indirect, and amorphous materials. Notably, the Monolog-Lorentz (ML) and Band-Fluctuations-Lorentz (BFL) models were inspired by the conventional Tauc-Lorentz model

proposed by Jellison et al. [69]. These models accurately shapes the spectra associated with the Urbach, fundamental, and high-transition zones. The advantages of these new models include the continuity of the expressions from tail states to the fundamental absorption, a global description for direct/indirect/amorphous semiconductors from a common ansatz, and the accurate description of direct semiconductors, which is currently missing in literature. These models have been applied to absorption data at room temperature for direct transition semiconductors such as InP, MAPbI$_3$, and GaAs, indirect transition semiconductors such as GaP and c-Si, and amorphous materials such as a-Si. The spectral data was aquire from literature and libraries. The fitting of these new models involve the determination of properties such as the bandgap and Urbach energies from the fundamental oscillator. Then, we add oscillators to shape the high energy regions. Finally, this chapter concludes with a comparison of the analyzed materials with previous literature reports, and the results show that our models agree excellently with other studies. [58]

In Chapter 3, the optical properties of excitonic semiconductors is explored. Accordingly, the Elliott model, for the absorption when the interaction between electrons and holes is taken in to account, is examined. The Elliott theory predicts two absorption contributions: a discrete region below the bandgap and a continuous one above it. The former is composed of exciton energy levels and arises from the bound solutions of the hydrogen atom model. The latter arises from unbound solutions and is amplified due to the Coulomb interaction. Subsequently, I employ the band-fluctuations technique on the Elliott model, which leads to the development of a new analytic expression called the Elliott-Band-Fluctuations (EBF) model. This equation has two parts for the discrete and continuous segments of the imaginary component of the dielectric constant. In addition, we incorporate the effects of the uncertainty principle using a pseudo-Voigt profile, as suggested in Soufiani et al. [154]. The final equation contains both the thermal effects of the EBF model and the uncertainties modeled as the Lorentz function. We apply this model to fit absorption data at various temperatures for GaAs and the tri-halide Perovskites family, namely MAPbBr$_3$, MAPbI$_3$, and MAPbI$_x$Cl$_{3-x}$. The fits are excellent and the retrieved values for the bandgap and binding energy are compared with those obtained from other studies, showing excellent agreement.

Chapter 4 is dedicated to the analysis of the thermal evolution of the parameters obtained in Chapter 3 for both the GaAs and halide perovskite systems, which allows us to derive their respective thermal properties. The thermal evolution of the bandgap is discussed in terms of contributions from electron-phonon coupling and thermal expansion. The former is correlated with the positive pressure-induced evolution of the bandgap, while the latter is always negative. In the case of GaAs, the electron-phonon (e-ph) contribution is explained using the Varshni model [179], whereas for perovskites, Cardona's model [204] with only the thermal

contribution is used to explain the evolution of the bandgap. Regarding the broadening (FWHM) evolution, we employ a model based on the enhancement of the excitonic peak through electron-phonon coupling. This model allows us to obtain the LO phonon energy, which is similar to the Debye energy. Furthermore, a significant portion of this research is devoted to explaining the exciton binding energy in perovskites, given the substantial variability in the experimental reports obtained through absorption, photoluminescence, and magneto-absorption techniques.

We employ Pollmann's model [125], which has been modified by Kane [73], to investigate exciton formation in polar semiconductors, such as perovskites. These materials have a moderate electron-phonon coupling, which can be described using the Fröhlich interaction. In the work of Kane et al. this e-ph term is introduced into the exciton Hamiltonian, resulting in a binding energy for the excitons that is dependent on the effective dielectric constant and the phonon energy. After reproducing this self-consistent result for perovskites, we found that this theory can explain the significant discrepancies observed in the literature. This is because the binding energy obtained from the EBF model is in agreement with the theoretical calculation of Kane's model, which utilizes the LO phonon energy obtained from the bandgap or FWHM thermal evolution. Therefore, it appears that polaronic effects in perovskites and possibly other polar materials are compatible with the band-fluctuations approach. Moreover, by reversing the use of Kane's model, we can predict effective band masses and compare them to the Hydrogen-like model of excitons.

The final section of chapter 4 involves the computation of several thermal properties, including heat capacity, internal energy, Helmholtz function, and entropy. To achieve this, we employ the Debye model for the phonon density of states and the LO phonon frequency. The specific heat results for GaAs and perovskites are then compared with existing reports, demonstrating a high degree of correspondence, whenever they are determined accurately. This supports the notion that fundamental optical measurements can furnish useful insights into the thermal characteristics of solids.

Lastly, chapter 5 summarizes all the important conclusions of this PhD work.

Chapter 2

Global Description of the Absorption: The Band Fluctuations Lorentz Model

Models describing the fundamental absorption and high absorption regions of dielectric non-excitonic materials are scarce, in particular is astonishing that there is no equivalent Tauc-Lorentz model for direct electronic transitions materials. The correct determination of quantities such as the optical bandgap, Urbach energy and oscillator central energies, relies on their physical validity. The knowledge of the optical bandgap and Urbach energy are essential for optoelectronic devices design [58, 166, 174]. In addition, the oscillator's central energy is fundamental for exploring distinct electronic band transitions and material simulations [150].

The absorption edges or fundamental absorption region, where the onset of band-to-band absorption takes place, is typically overlapped with disorder induced localized states, i.e. Urbach tails, whereas the high absorption regime is governed by band-to-band transitions which can be properly described by the classical Lorentz oscillator model and its variants [44]. In the last two decades, these regions have been typically described by the models of Tauc [165], Jellison and Modine [69], Ferlauto [37], and more recently by Ullrich [176, 175], O'Leary [117, 168] and our group [58].

Whereas most of these models have found their way to commercial software and are widely used to model the properties of distinct materials, the most commonly used model is perhaps the Tauc-Lorentz (TL) model. Although Tauc's parabolic absorption spectra is used to describe the absorption edge of indirect and amorphous materials, nowadays it is used for direct semiconductors as well when fitting optical transmittance, reflectance and ellipsometric data, biasing and underestimating the optical bandgap [48]. The TL model does not take into account Urbach tails, attributed to disorder-induced localized states and thermal effects. Thus, when fitting optical data of direct electronic transitions materials, besides the

difference in shape in the fundamental absorption, the exponential Urbach tail is actually fitted with the parabolic shape of Tauc's model. This is the main problem of using the TL model for retrieving the optical bandgap.

Ferlauto et al.[37] developed a model by incorporating an exponential tail to the TL model. This model came to be known as Cody-Lorentz (CL) model. On the other hand, Ullrich et al [176, 175] modelled the absorption coefficient of direct electronic transitions materials through the addition of an exponential behaviour below the bandgap that satisfies the first derivative continuity condition. Also, O'Leary et al [117, 168] modelled the absorption coefficient of amorphous silicon by incorporating an exponential tail to the valence-band density of states, which was further convoluted with the conduction-band density of states to calculate the fundamental absorption. In a previous work [58], our research group modified the absorption edge by introducing band-fluctuations to the joint density of states for both direct and indirect electronic transitions materials. In this way Urbach tails are incorporated in both types materials [58]. These models were then used to analyze experimental data.

In order to arrive at an accurate description of the optical absorption, we propose in this work to apply the procedure of Jellison et al, to obtain the Tauc-Lorentz model, but instead to the Ullrich, O'Leary and bands-fluctuations approaches, thus, unifying the absorption edge and high absorption regions in a single equation for each model. The aforementioned models are widely discussed in section 2.1.

In section 2.2, we proceed and develop each of the aforementioned models in a single electronic Joint Density of States (JDOS), which is proportional to the optical absorption coefficient. In section 2.3, we extend the models to include a Lorentz oscillator component for the high absorption region. We compare the extended models with experimental data for direct electronic transitions materials such as methylammonium lead iodide (MAPI), a metal halide pervoskite whose bandgap can be controlled stoichiometrically. For instance, this is exploited when the bandgap is tunned for tandem solar cells [162, 101]. We compare the models also with experimental data of gallium arsenide (GaAs) and indium phosphide (InP) whose applications are in high-speed, optoelectronic and photovoltaic devices [68, 184], and indirect electronic transitions materials such as gallium phosphide (GaP) which is used typically in Light Emitting Devices (LED) technology [183], crystalline silicon (c-Si), which is widely used in electronic and photovoltaic applications [74, 120], and amorphous hydrogenated silicon (a-Si:H), which is used in thin film solar cells [59, 153].

2.1   Established absorption edge models

Here we summarize current models for the absorption edge. We extend the Tauc-Lorentz approach to these models to account for high energy band-to-band transitions and deliver analytical expressions for each model.

2.1.1   Fundamental Absorption
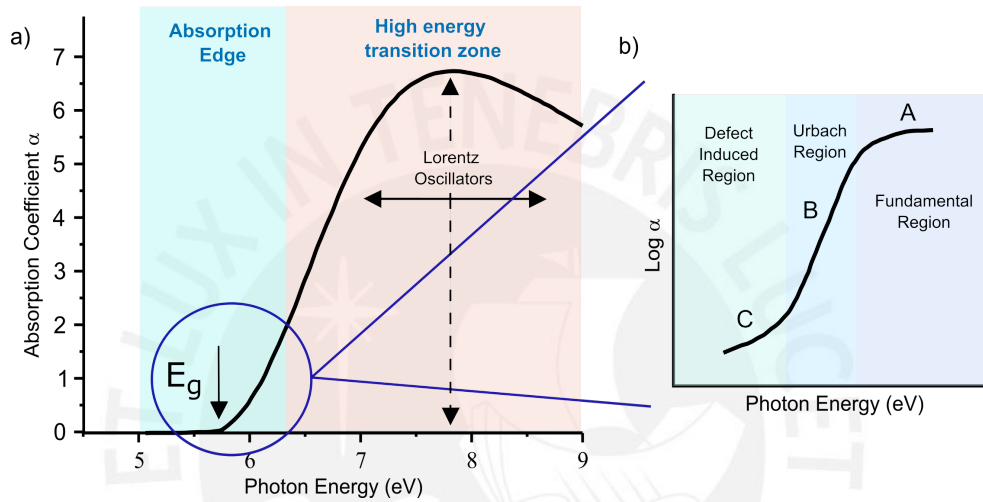
Fig. 2.1 Schematic of the absorption coefficient (α) near the absorption edge and high energy region (a). The different regions of the absorption edge region are illustrated in logarithmic scale in figure (b). Here, region A corresponds to the fundamental absorption, region B to the Urbach tail and region C to the absorption induced by impurities present in the material.
.

The description of the absorption coefficient near the absorption edge is typically described in three regions as depicted in figure 2.1. Region A corresponds to the parabolic band approximation, usually fitted with Tauc's equation, region B corresponds to the universally observed Urbach tail associated with disorder-induced localized states. Region C is associated to defect-induced localized states. The latter zone is typically studied by optical absorption measurements of bulk crystals [192, 193, 9], or thin films by UV-Excited Photoelectron Spectroscopy (UPS) on states near the valence band edge and can be modeled independently [100, 101]. For our purposes this region won't be part of our analysis.

The description of the optical properties of semiconductors was developed in the early 60s. It is based on the existence of long-range order, electron k-vector conservation and Fermi's golden rule. The absorption coefficient is proportional to the electronic transition

rate, which in the most general case can be written as [204]:

$$R_{cv} = R \sum_{k_c, k_v} |M_{cv}|^2 \delta(E_c - E_v - \hbar\omega \pm E_\Omega) \delta_{k_c, k_v + q \pm k_\Omega}.$$

Here R is $2\pi/\hbar(|\vec{E}|e/2\omega m_e)^2$. E_c and E_v are the electron conduction and valence band energy states. $|M_{cv}|$ is the electronic transition momentum matrix element whose behavior is typically taken constant near the absorption edge in both direct and indirect cases, whilst is typically modeled by means of the Lorentz oscillator for higher energies. Note that the general electronic transition is a function of the photon ($\hbar\omega$) and phonon (E_Ω) energies, and the photon (q) and phonon (k_Ω) wave vectors. Thus, we have the energy conservation term $E_c = E_v + \hbar\omega \mp E_\Omega$, and the wave vector conservation $k_c = k_v + q \pm k_\Omega$. For $E_\Omega \ll \hbar\omega$ and $q \ll 1$, the terms q and E_Ω can be neglected. For the case of direct electronic transitions materials, the most probable transitions keeps $k_c = k_v$, whilst in the case of indirect transitions we have $k_c = k_v \pm k_\Omega$. Remarkably, the shift induced by k_Ω can be observed and characterized for cryogenic temperatures. In the framework of the effective mass approximation (parabolic electronic bands approximation), the conduction (D_c) and valence D_v bands electronic density of states are [67], i.e.,

$$D_c(E_c) = \frac{\sqrt{2} m_e^{*3/2}}{\pi^2 \hbar^3} (E_c - E_g)^{1/2} \Theta(E_c - E_g), \tag{2.1}$$

$$D_v(E_v) = \frac{\sqrt{2} m_h^{*3/2}}{\pi^2 \hbar^3} (-E_v)^{1/2} \Theta(-E_v). \tag{2.2}$$

Here m_e and m_h are the electron and hole masses. E_c and E_v are the conduction and valence band energy. E_g is the band gap energy, and Θ is the step-function. For the case of direct semiconductors, the transition rate from the conduction and valence band, R_{cv}^d, can be written in terms of the JDOS D_{cv} with $E_{cv} = E_c - E_v$ as the energy band difference [204], i.e.,

$$R_{cv}^d = R \int dE_{cv} |M_{cv}|^2 D_{cv}(E_{cv}) \delta(E_{cv} - E). \tag{2.3}$$

$D_{cv}(E_{cv})$ displays a square root shape versus E_{cv} and it is proportional to the reduced effective mass $\mu^{*-1} = m_e^{*-1} + m_h^{*-1}$:

$$D_{cv}(E_{cv}) = \frac{\sqrt{2} \mu^{*3/2}}{\pi^2 \hbar^3} (E_{cv} - E_g)^{1/2} \Theta(E_{cv} - E_g). \tag{2.4}$$

Consequently, the electronic transition rate is:

$$R_{cv}^d = R|M_{cv}|^2 \frac{\sqrt{2}\mu^{*3/2}}{\pi^2 \hbar^3}(E - E_g)^{1/2}\Theta(E - E_g). \tag{2.5}$$

On the other hand, in the case of indirect electronic transitions materials, all energetically possible transitions between initial valence (v) and final conduction (c) states must be considered. For this reason, R_{cv}^i is written in terms of the valence D_v and conduction D_c electronic Density Of States (DOS), i.e.,

$$R_{cv}^i = R|M_{cv}|^2 \int dE_{cv} J_{cv}(E_{cv})\delta(E_{cv} - E), \tag{2.6}$$

with

$$J_{cv}(E_{cv}) = \frac{2(m_e^* m_h^*)^{3/2}}{\pi^4 \hbar^6} \frac{\pi}{8}(E_{cv} - E_g)^2 \Theta(E_{cv} - E_g) \tag{2.7}$$

as the indirect JDOS and $E_{cv} = E_c - E_v$. Note that the JDOS of eq. (2.7) is a crude expression where the effect of the phonons has been neglected. However, note that phonon contributions can be added by changing $E_{cv} - E_g$ to $E_{cv} - E_g \pm E_\Omega$. However, as temperature increases, the effect of the phonons is broadened out in the Urbach tail. Nonetheless, eq. (2.7) is empirically used for the description of the band edge. The indirect electronic transition rate is:

$$R_{cv}^i = R|M_{cv}|^2 \left(\frac{(m_e^* m_h)^{3/2}}{4\pi^3 \hbar^6} \right)(E - E_g)^2 \Theta(E - E_g). \tag{2.8}$$

For the case of amorphous materials, Tauc successfully derived a straightforward formula for the fundamental absorption. He relaxed the conservation of the wave vector k, allowing all possible transitions [165, 204]. Coincidentally, the simplification proposed by Tauc has the same quadratic behavior as for indirect electronic transitions materials, i.e.,

$$\tilde{\varepsilon}_2 \approx \frac{(E - E_g)^2}{E^2} \tag{2.9}$$

This analysis was key to understanding the fundamental absorption of a-Si[165].

Equations (2.5) and (2.8) are the starting set of equations for the extensions we propose in this work. They can be coupled to Lorentz oscillator and fulfill the Kramers-Kronig (KK) condition [69], i.e. the function must fall to zero faster than $1/E^2$ as the frequency approaches infinity. However, these models do not consider the Urbach tail overlap on the fundamental absorption and thus bias the bandgap determination.

Urbach found experimentally in 1953 an exponential behavior in the optical absorption edge of AgBr crystals [178]:

$$\tilde{\varepsilon}_2 \approx e^{(E/E_U)}. \tag{2.10}$$

Here E_U is the Urbach energy and represent the inverse of the slope when logarithmic scale is used. The nature of the Urbach rule could be attributed to many factors such as the presence of longitudinal-optical (LO) phonons involved in electronic transitions [157], the exciton-phonon interaction (exciton self-trapping) [173] or by the Franz-Keldysh effect, in which Bloch waves can tunnel in the bandgap region due to an electric field originating from vibrations in the atomic network [128]. Despite their diverse origins, the current consensus is that thermal effects and static disorder are the main reasons behind their appearance [20, 21, 152].

There are various models trying to describe the behavior of tail states, such as the models of Ullrich [175, 176], O'Leary, Malik [117, 115, 116, 96], Orapunt [119], Thevaril [167, 168] and, most recently, by our group [58]. In particular, the model of Dunstan [31], introduced in a simple way band fluctuations effects directly in the absorption coefficient. Ullrich's and O'Leary's models are based on a modified DOS. In both models, the DOS is a piecewise function of tail states and extended states. Ullrich modifies eq. (2.4) as:

$$D_{cv}^U(E_{cv}) = D_0 \begin{cases} (E_{cv} - E_g)^{1/2} & ,E_{cv} \geq E_{cv_T} \\ \frac{1}{\sqrt{2\beta}}e^{\beta(E_{cv} - E_{cv_T})} & ,E_{cv} < E_{cv_T} \end{cases} \tag{2.11}$$

for the case of direct electronic transitions materials. D_0 is an overall constant, β is the inverse of Urbach energy and $E_{cv_T} = E_g + 1/(2\beta)$ denotes the point satisfying the first derivative continuity condition for a smooth transition between the exponential tail and the square root describing the transition between extended states. On the other hand, O'Leary proposes a modified eq. (2.2) for amorphous Si:

$$D_v^O(E_v) = \frac{\sqrt{2}m_h^{*3/2}}{\pi^2\hbar^3} \begin{cases} \frac{1}{\sqrt{2\beta_v}}e^{\beta_v(E_{v_T} - E_v)} & ,E_v > E_{v_T} \\ (-E_v)^{1/2} & ,E_v \leq E_{v_T} \end{cases}, \tag{2.12}$$

where E_{v_T} guarantees the continuity of the DOS. Tails are considered in the valence DOS only, while conduction DOS remains as in eq. (2.1) [117].

We can calculate the respective electronic transition rates, for direct

$$R_{cv}^U = R|M_{cv}|^2 D_{cv}^U(E), \tag{2.13}$$

and indirect (amorphous) materials

$$R^O_{cv} = R|M_{cv}|^2 J^O_{cv}(E), \tag{2.14}$$

where

$$J^O_{cv}(E) = J_0 \frac{1}{\beta^2} j^O_{cv}(\beta(E - E_g)) \tag{2.15}$$

with J_0 being an overall constant, and

$$j^O_{cv}(z) = \begin{cases} \Xi(z) & ,z \geq 1/2 \\ \frac{1}{\sqrt{2}}e^{(z-1/2)}Y(0) & ,z < 1/2 \end{cases}, \tag{2.16}$$

with

$$\Xi(z) = z^2 \Sigma\left(\frac{z - 1/2}{z}\right) + \frac{1}{\sqrt{2}}Y(z - \frac{1}{2})e^{(z-\frac{1}{2})}, \tag{2.17}$$

and

$$\Sigma(z) = \frac{\pi}{8} + \frac{\sqrt{z - z^2}}{4}(2z - 1) + \frac{\sqrt{z - 1}}{4}\frac{\mathrm{Sinh}^{-1}(\sqrt{z - 1})}{\sqrt{1 - z}}, \tag{2.18}$$

$$Y(z) = \sqrt{z}e^{-z} + \frac{\sqrt{\pi}}{2}\mathrm{Erfc}(\sqrt{z}). \tag{2.19}$$

Eqs. (2.13) and (2.14) can describe the whole fundamental region smoothly. Urbach tails can be generated by means of band-fluctuations. This approach has been successfully applied to amorphous Si:H, SiC:H, SiN, crystalline GaAs and nano-crystalline GaMnN [58, 56], nano-crystalline methylammonium lead iodide [57], and formamidinium cesium lead mixed-halide [166]. Band-fluctuations give rise to Urbach tails, thus, the determined optical bandgap, by fitting these models, is bias free. Details on this approach can be found elsewhere [58].

According to the band-fluctuations model, the direct and indirect JDOS are expressed in terms of the Poly-logarithmic functions (Li_n) of order n:

$$D^G_{cv}(E) = -\frac{\sqrt{2}\mu^{*3/2}}{\pi^2\hbar^3}\frac{1}{2}\sqrt{\frac{\pi}{\beta}}\mathrm{Li}_{1/2}\left(-e^{\beta(E - E_g)}\right), \tag{2.20}$$

$$J^G_{cv}(E) = -\frac{2(m^*_e m^*_h)^{3/2}}{\pi^4\hbar^6}\frac{1}{4}\frac{\pi}{\beta^2}\mathrm{Li}_2\left(-e^{\beta(E - E_g)}\right). \tag{2.21}$$

Eqs. (2.20) and (2.21) describe an exponential Urbach tail and the square-root/quadratic behavior for direct/indirect (amorphous) semiconductors in the limiting cases below and above the bandgap, respectively.

2.1.2 High Energy Transition Zone

Above the fundamental absorption, band-to-band electronic transitions are characteristic and can be described by the Lorentz model or driven harmonic oscillator (DHO). The solid is considered classically by the assumptions that electrons are bound to nuclei harmonically and with dissipative effects [48, 1]. The real ($\tilde{\varepsilon}_1$) and imaginary ($\tilde{\varepsilon}_2$) parts of the electrical permittivity are:

$$\tilde{\varepsilon}_1 = 1 + \frac{S(E_c^2 - E^2)^2}{(E_c^2 - E^2)^2 + B^2 E^2}, \tag{2.22}$$

$$\tilde{\varepsilon}_2 = \frac{SBE}{(E_c^2 - E^2)^2 + B^2 E^2}. \tag{2.23}$$

Equation (2.23) is the so called Lorentz term and is parametrized by the strength S, width B and central energy E_c of the oscillator peak. The presence of a single peak is rather uncommon due to the many-body system of a crystalline solid. For this reason, the common agreed extension is to add several oscillators as

$$\tilde{\varepsilon}_2 = \sum_i \frac{S_i B_i E}{(E_{ci}^2 - E^2)^2 + B_i^2 E^2}. \tag{2.24}$$

Tauc-Lorentz Model.

Attempts to find a modified Lorentz model that includes Tauc's law and/or Urbach tail are many. The first such model was proposed by Forouhi and Bloomer [38]. This model lacks time reversal symmetry and the integral in the sum rule diverges [44]. However, it has served as an inspiration of forthcoming models.

Subsequent models overcoming above issues were proposed by Campi and Coriasso (CC) [16], and then by Jellison and Modine (JM) [69]. Despite both models describing the driven harmonic oscillator coupled with Tauc's law, the most popular is the JM model and is usually cited as the Tauc-Lorentz (TL) model. It has been implemented in the majority of optical analysis softwares nowadays.

The idea behind the TL model is to modify the energy independent transition matrix element M_{cv} present in eq. (2.8) to an energy dependent function (the Lorentz oscillator). This is achieved by multiplying the imaginary electrical permittivity of the Lorentz model, eq. (2.23), with the quadratic behavior, eq. (2.8), for indirect semiconductors, i.e. for energies above E_g,

$$\tilde{\varepsilon}_2^{TL}(E) = \tilde{\varepsilon}_2^T(E) \times \tilde{\varepsilon}_2^L(E), \tag{2.25}$$

$$\tilde{\varepsilon}_2^{TL}(E) = \frac{(E - E_g)^2}{E^2} \frac{SBE \times \Theta(E - E_g)}{(E^2 - E_c^2)^2 + B^2 E^2}. \tag{2.26}$$

This model is physically consistent, it is Kramers-Kronig consistent, and it converges into the classical Lorentz model for high energies [43, 44]. Despite the success of the TL model, it presents two main problems: (i) It underestimates the bandgap by not including the Urbach tail. (ii) Its shape is for indirect (and amorphous) electronic transitions materials only. Since the functional behavior arises from the quadratic dependence with photon energy, in practice, the Urbach tails are modeled by the parabolic shape of the Tauc model, biasing the determination of the bandgap.

We aim our attention to the different models that can be obtained by emulating the approach of eq. (2.25), referring to them as modified TL models.

2.1.3   Modified Tauc-Lorentz Models

The first modified TL model was proposed by Ferlauto [37]. It was later known as the Cody-Lorentz (CL) model to honor Cody's research on a-Si. More recently Franta et al. [44] proposed two new models. Their idea was based on replacing the DHO with the Lorentz function. Like the CL model, the latter yielded an analytical $\tilde{\varepsilon}_1$ after Kramers-Kronig transformation. Here, we extend the spectral dependence of Ullrich, O'Leary and BF by incorporating the Lorentz oscillator.

Cody-Lorentz Model.

The absence of the Urbach tail in the TL model was tackled by Ferlauto et al. They incorporated the exponential behavior of Urbach tails to the TL model through a piece-wise function [37], i.e.,

$$\tilde{\varepsilon}_2(E) = \begin{cases} \frac{E_1}{E} e^{(E - E_t / E_U)} & , 0 < E \le E_t \\ G(E) \frac{SBE}{(E^2 - E_c^2)^2 + B^2 E^2} & , E > E_t \end{cases} \tag{2.27}$$

Here E_t is a fitting parameter that defines the transition energy from the exponential behavior to the TL one. E_1 is a parameter in function of E_t that guarantees the continuity of $\tilde{\varepsilon}_2(E)$. $G(E)$ can be either $G_T(E) = (E - E_g)^2 / E^2$ (which correspond to a constant momentum matrix element) or the function proposed by Ferlauto et al. to fit a-Si:H [37]:

$$G_C(E) = \frac{(E - E_g)^2}{(E - E_g)^2 + E_p^2}. \tag{2.28}$$

E_p represents a second-order transition before Lorentz oscillator takes shape. It is important to remark that this equation arises from the consideration of a constant dipole matrix element.

And, even though it may seem the natural extension of the TL model, it carries two main problems, i.e. the discontinuity produced by E_t for the first derivative of $\tilde{\varepsilon}_2$ and the quadratic dependence of $G(E)$ excluding direct semiconductor's absorption behavior.

In the following, we propose alternatives to the Tauc-Lorentz and Cody-Lorentz models based on the Ullrich, O'leary and band-fluctuations approach. These new expressions are presented from sections 2.3.2 to 2.3.5

Ullrich-Lorentz (UL) Model.

The problems of the CL model can be overcome by Ullrich's work for direct electronic transitions materials. Following the aforementioned procedure of Jellison-Modine model, we multiply the Lorentz electrical permittivity, eq. (2.23), to the Ullrich's continuous dielectric function which can be derived from eq. (2.13),

$$\tilde{\varepsilon}_2^U(E) = \frac{8\pi\hbar}{|\vec{E}|^2}R_{cv}^U = \frac{4\pi^2 e^2}{\omega^2 m_e^2}|M_{cv}^2|D_{cv}^U. \tag{2.29}$$

The Ullrich-Lorentz dielectric function will take the form:

$$\tilde{\varepsilon}_2^{UL}(E) = \tilde{\varepsilon}_2^U(E) \times \tilde{\varepsilon}_2^L(E), \tag{2.30}$$

$$\tilde{\varepsilon}_2^{UL}(E) = \frac{4\hbar^2\pi^2 e^2|M_{cv}^2|D_{cv}^U(E)}{E^2 m_e^2}\frac{SBE}{(E^2 - E_c^2)^2 + B^2 E^2}, \tag{2.31}$$

$$\tilde{\varepsilon}_2^{UL}(E) = C\frac{L(E)}{E\sqrt{\beta}}\begin{cases}(\beta(E - E_g))^{1/2} & , E \geq E_g + \frac{1}{2\beta}\\ \frac{1}{\sqrt{2}}e^{\beta(E - E_g)} & , E < E_g + \frac{1}{2\beta}\end{cases}. \tag{2.32}$$

Here $L(E)$ is the Lorentz function,

$$L(E) = \frac{B}{(E^2 - E_c^2)^2 + B^2 E^2}, \tag{2.33}$$

C is a constant equal to $4\pi^2\hbar^2 e^2|M_{cv}^2|D_0 S/m_e^2$. And β is the Urbach slope.

The UL model offers continuity of eq. (2.32) in the first derivative and the square root shape of the absorption coefficient for direct electronic transitions materials as well as the Lorentz behavior for higher energies.

O'Leary-Lorentz (OL) Model.

We now use the same procedure devised by Jellison-Modine for the O'Leary model for indirect/disordered electronic transitions materials, i.e.

$$\tilde{\varepsilon}_2^{OL}(E) = \varepsilon_2^O(E) \times \tilde{\varepsilon}_2^L(E), \tag{2.34}$$

$$\tilde{\varepsilon}_2^{OL}(E) = \frac{\tilde{C}}{E}\frac{L(E)}{\beta^2}\begin{cases} \Xi(\beta(E-E_g)) & ,E \geq E_g + \frac{1}{2\beta} \\ \frac{Y(0)}{\sqrt{2}}e^{\left(\beta(E-E_g)-\frac{1}{2}\right)} & ,E < E_g + \frac{1}{2\beta} \end{cases}, \tag{2.35}$$

with $\tilde{C}$ equal to $4\pi^2\hbar^2 e^2 |M_{cv}^2|J_0 S/m_e^2$. This model is continuous in the first and second derivatives.

Band-Fluctuations-Lorentz (BFL) Model.

The UL and OL models are excellent modifications to the Lorentz model since they carry all the information needed for the fundamental absorption of both direct and indirect (amorphous) materials and fulfill the requirements for a Kramers-Kronig transformation. In addition, the band-fluctuations model offers a good description of the fundamental absorption as it was shown in a previous work [58]. The extension of the BF model following the approach of Jellison-Modine is

$$\tilde{\varepsilon}_2^{BFL}(E) = \tilde{\varepsilon}_2^{BF}(E) \times \tilde{\varepsilon}_2^L(E),$$

$$\tilde{\varepsilon}_{2,d}^{BFL}(E) = -C\frac{1}{2E}\sqrt{\frac{\pi}{\beta}}\text{Li}_{1/2}\left(-e^{\beta(E-E_g)}\right)L(E), \tag{2.36}$$

for direct (*d*) electronic transitions materials, and

$$\tilde{\varepsilon}_{2,i}^{BFL}(E) = -\tilde{C}\frac{\pi}{4\beta^2 E}\text{Li}_2\left(-e^{\beta(E-E_g)}\right)L(E), \tag{2.37}$$

for indirect/amorphous (*i*) electronic transitions materials. The BFL model can describe the absorption coefficient near the band edge of either direct and indirect (amorphous) electronic transitions materials from the same principles. Likewise, the description of Urbach tails in a single equation can be seen in the asymptotic behavior of the polylog function as $\sqrt{E-E_g}$ and $(E-E_g)^2$ for the direct and indirect cases, respectively. Lastly, the softness and continuous transition from the fundamental to the high energy zone is well described by this model.

Monolog-Lorentz Model.

The Polylogarithmic functions of order 2 and $1/2$ that appear in the BF and BFL models are available in most software mathematical analysis environments such as Wolfram Mathematica, MatLab, Python, but not in other more common software for fitting analysis. For this reason, we propose a semi-empirical model based on the band-fluctuations approach which produces an analytic expression. This is done by performing the fluctuations operation on the linear scale (Tauc-scale) of the JDOS for the direct and indirect cases, respectively. For direct electronic transitions materials $\tilde{\varepsilon}_2$ is

$$\tilde{\varepsilon}_{2,d}^M(E) = \frac{C}{E^2}\sqrt{\frac{1}{\beta}}\log^{1/2}\left(1 + e^{\beta(E-E_g)}\right),\tag{2.38}$$

and then multiplied by the the Lorentz term of eq. (2.23) it becomes

$$\tilde{\varepsilon}_{2,d}^{ML}(E) = C\frac{1}{E}\sqrt{\frac{1}{\beta}}\log^{1/2}\left(1 + e^{\beta(E-E_g)}\right)L(E).\tag{2.39}$$

For indirect/amorphous materials, $\tilde{\varepsilon}_2$ is

$$\tilde{\varepsilon}_{2,i}^M(E) = \frac{\tilde{C}}{E^2}\frac{\pi}{8\beta^2}\log^2\left(1 + e^{\beta(E-E_g)}\right),\tag{2.40}$$

and multiplying by the Lorentz it becomes

$$\tilde{\varepsilon}_{2,i}^{ML}(E) = \tilde{C}\frac{\pi}{8\beta^2 E}\log^2\left(1 + e^{\beta(E-E_g)}\right)L(E).\tag{2.41}$$

Despite this model being straightforward based on the observation of the functional behavior generating an Urbach tail rather than physical principles, it can give bandgap, Urbach and oscillators central energies very close, if not the same, as those retrieved by the BFL models. For instance, the asymptotic behavior of eq. (2.38) for direct electronic transitions materials is

$$\tilde{\varepsilon}_{2,d}^M(E) \approx \frac{C}{E^2}\begin{cases} \sqrt{E-E_g} & ,E \gg E_g \\ \sqrt{\frac{1}{\beta}}e^{\frac{\beta}{2}(E-E_g)} & ,E \ll E_g \end{cases}\tag{2.42}$$

and, for indirect, eq. (2.40) behaves asymptotically as

$$\tilde{\varepsilon}_{2,i}^M(E) \approx \frac{\tilde{C}}{E^2}\pi\begin{cases} \frac{1}{8}(E-E_g)^2 & ,E \gg E_g \\ \frac{1}{8\beta^2}e^{2\beta(E-E_g)} & ,E \ll E_g \end{cases}.\tag{2.43}$$

Note how the exponential tail and the square root (parabolic) shape versus the photon energy are recovered for direct (indirect) electronic transitions.

It is important to remark that the dimensionality of our models correspond to the case of bulk (3D). However, if we would like to apply the Tauc-Lorentz procedure to lower dimensional materials, such as quantum wells (2D), quantum wires (1D) and quantum dots (0D), a modification of the JDOS is mandatory. The square root behavior of eqs. (2.1) and (2.2) shall be replaced with the corresponding DOS of lower dimensions. On the other hand, the Lorentz model is independent of the dimensions of the sample, so eq. (2.23) remains unchanged.

2.2   Dimensionless JDOS formalism

There are certain mathematical features in the implementation of the aforementioned models that are remarkable. For example, the capability to perform a single fit of the fundamental region and the band-to-band transition zone with 5 parameters only: the constant C, Urbach slope β, bandgap E_g, oscillator central energy E_c and the oscillator broadening B. Furthermore, it gives the advantage of discriminating tail states from band-to-band electronic transitions, as well as the direct determination of the bandgap from the fit without further bias due to the overlap of the Urbach tail. In order to examine the universality of the shape of these models, we carry on a dimensionless JDOS analysis of the fundamental absorption [117, 168]. The importance of this scheme is the dependency of the models on a single parameter, forming a universal curve which can be used for comparison purposes. What is more, experimental results can be brought to this analysis [168, 117]. The procedure consists in rewriting the aforementioned models in terms of a dimensionless independent variable $z = \beta(E - E_g)$ [168, 117, 58]. The permittivity proportional to the JDOS is then divided by the Lorentz oscillator L(E) component along with the multiplying constants, i.e., for the direct case, we have

$$\mathscr{D}_{cv}(z) = \frac{\tilde{\varepsilon}_2 E \sqrt{\beta}}{L(E)C}, \tag{2.44}$$

while for indirect/amorphous case,

$$\mathscr{J}_{cv}(z) = \frac{\tilde{\varepsilon}_2 E \beta^2}{L(E)\tilde{C}} \tag{2.45}$$

For direct electronic transitions materials we have the Ullrich-Lorentz model

$$\mathscr{D}_{cv}^{UL}(z) = \begin{cases} \sqrt{z} & , z \geq 1/2 \\ \frac{1}{\sqrt{2}} e^{(z-1/2)} & , z < 1/2 \end{cases} \tag{2.46}$$

the BF-Lorentz,

$$\mathscr{D}_{cv}^{BFL}(z) = -\frac{\sqrt{\pi}}{2} \mathrm{Li}_{1/2}\left(-e^z\right), \tag{2.47}$$

and the Monolog-Lorentz as

$$\mathscr{D}_{cv}^{ML}(z) = \log^{1/2}\left(1 + e^z\right). \tag{2.48}$$

Whereas, for indirect electronic transitions materials we have the O'Leary-Lorentz model

$$\mathscr{J}_{cv}^{OL}(z) = \begin{cases} \Xi(z) & , z \geq 1/2 \\ \frac{1}{\sqrt{2}} e^{(z-1/2)} Y(0) & , z < 1/2 \end{cases} \tag{2.49}$$

the BF-Lorentz,

$$\mathscr{J}_{cv}^{BFL}(z) = -\frac{\pi}{4} \mathrm{Li}_2\left(-e^z\right), \tag{2.50}$$

and the Monolog-Lorentz as

$$\mathscr{J}_{cv}^{ML}(z) = \frac{\pi}{8} \log^2\left(1 + e^z\right). \tag{2.51}$$

These models in the dimensionless JDOS framework are depicted and compared in figure 2.2. The models share the same behaviour on the fundamental region as the BFL model. The same happens for the indirect case. On the other hand, the exponential tail exhibit different slopes depending on the model. The latter being a feature of the procedure generating the tails in each model. The ML model for Urbach region present a large (short) Urbach tail for models corresponding to direct (indirect) transitions when compared to the UL (OL) model.

2.3 Comparison with experiments

Here we use the models to analyze the $\tilde{\varepsilon}_2$ of crystalline direct, indirect, and amorphous semiconductors. We use data of MAPI, GaAs and InP materials, to test the direct electronic transitions models. Whereas, we fit absorption coefficient data of crystalline Si and GaP and amorphous Si, to test indirect (amorphous) electronic transitions materials. The spectral data is collected from literature, as well as from materials libraries from the SpectraRay
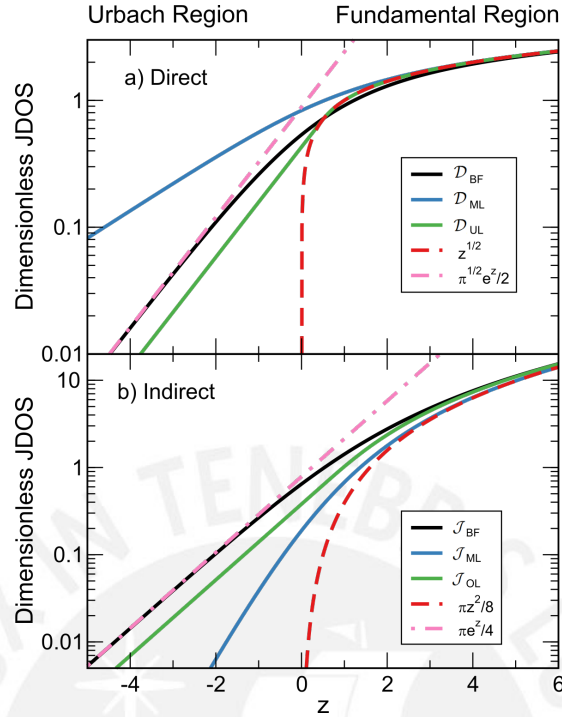
Fig. 2.2 Dimensionless JDOS for the different models. (a) Direct transition materials are represented by the models of Ullrich-Lorentz ($\mathscr{D}_{cv}^{UL}$), BF-Lorentz ($\mathscr{D}_{cv}^{BFL}$), Monolog-Lorentz ($\mathscr{D}_{cv}^{ML}$) and the square root behaviour. (b) Indirect transition materials are described by the models of O'Leary-Lorentz ($\mathscr{J}_{cv}^{OL}$), BF-Lorentz ($\mathscr{J}_{cv}^{BFL}$), Monolog-Lorentz ($\mathscr{J}_{cv}^{ML}$), and Tauc-Lorentz (quadratic behavior). The exponential behavior of the Urbach tail is illustrated in pink dashed lines for direct and indirect cases.

software. In the case of MAPI, the data is obtained by a point-by-point analysis combining Ellipsometry and Spectrophotometry [56], which is unbiased by a dispersion model. In the case of GaP, the spectral data was obtained after a two-phase model on the ellipsometry measurements [3]. For InP, cSi and GaAs, the spectral data from the library is obtained after modeling $\tilde{\varepsilon}_2$ using several TL oscillators. At this point is important to remark, that in the latter case, although $\tilde{\varepsilon}_2$ is already biased by a dispersion model, the spectral curve is good, but the parameters physical meaning are hindered. Lastly, the data of a-Si:H was obtained from modeling the ellipsometry measurements as in the previous cases [67].

The $\tilde{\varepsilon}_2$ spectra of each type of semiconductor are analyzed as follows. First, we perform a fit of the imaginary part of the electrical permittivity by using several oscillators up to a cutoff energy. In this process we have included an amount up to six oscillators in the fitting procedure. We use the BFL model to describe the fundamental absorption and TL for high absorption regions. Second, we perform an analysis exclusively of the fundamental oscillator for testing the pool of models such as UL, OL and ML. These parameters are then collected

and compared for direct and indirect transition materials, respectively. Third, we carry on a dimensionless analysis to compare the fits of different materials in the same dimensionless scale. Fits and dimensionless JDOS analysis are presented in linear and logarithmic scales for visualization purposes only. Nevertheless, all fitting procedure was performed in linear scale. Lastly, we present the Urbach slope analysis, in which we compare the retrieved Urbach energy from Urbach's law, and the ones obtained with the here presented models.

2.3.1   Direct semiconductors

In the case of MAPI, the imaginary part of the electrical permittivity used correspond to Guerra et al [57], whereas the rest were obtained from the SpectraRay software libraries. The spectra are shown in figure 2.3 in normal and logarithmic scale, for viewing purposes only. The fitting procedure used consists of adding oscillators one-by-one while keeping constant values of the previous oscillator. This fixed parameters are then set free for a final fit. In every material, the first oscillator near the band-edge seen in figure 2.3 corresponds to the BFL model, whilst the added oscillators ($2^{nd} - N^{th}$) to the TL model.
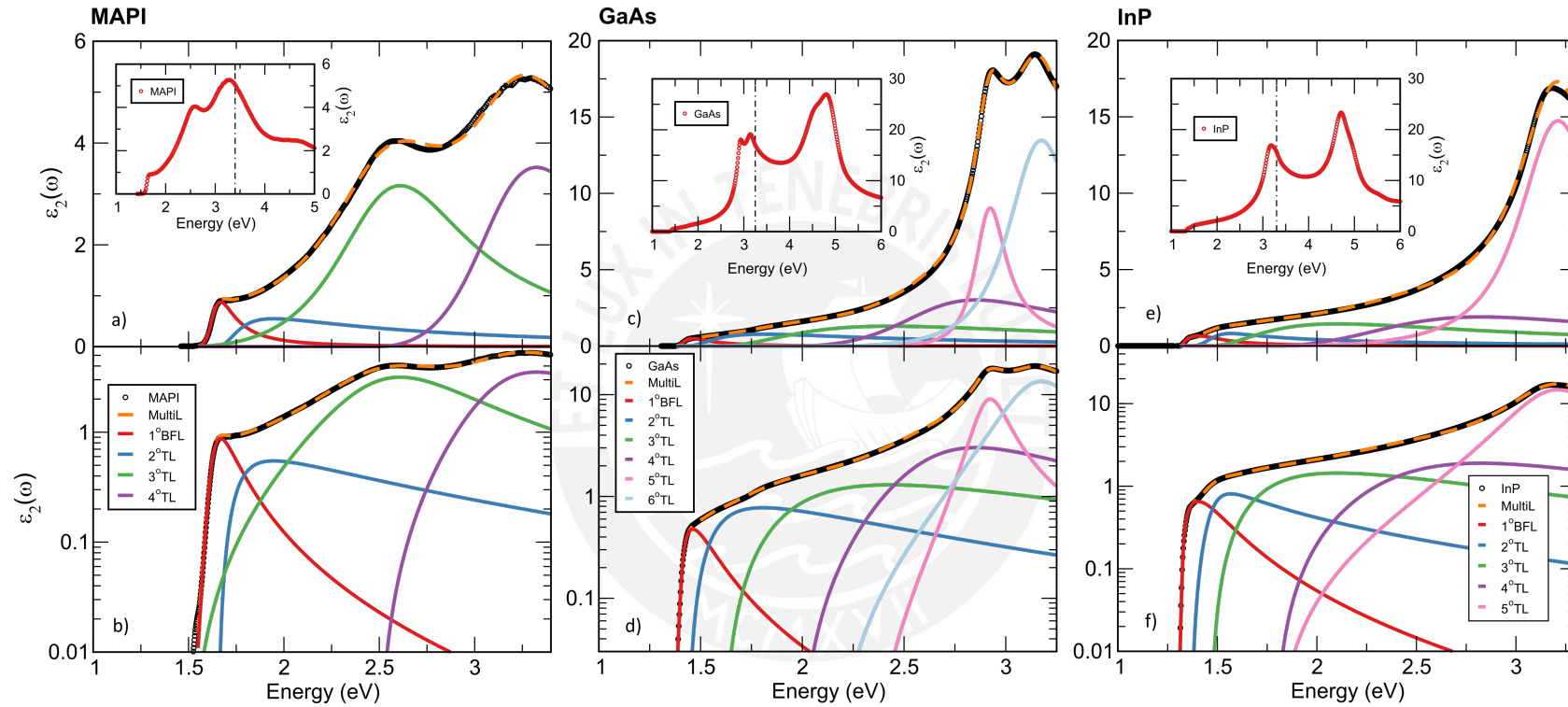
Fig. 2.3 Imaginary part of the electrical permittivity of methylammonium lead iodide (MAPI) (a,b), gallium arsenide (GaAs) (c,d), and indium phosphide (InP) (e,f). The experimental data (o) and fits using multiple Lorentz oscillators (Lorentz oscillators are presented as — ; while the sum is - - -) are illustrated on a linear and a semi-logarithmic scale. The insets in these figures show the full range of values from the VIS to UV. Here, the dashed lines represents the cutoff energy taken for the analysis.
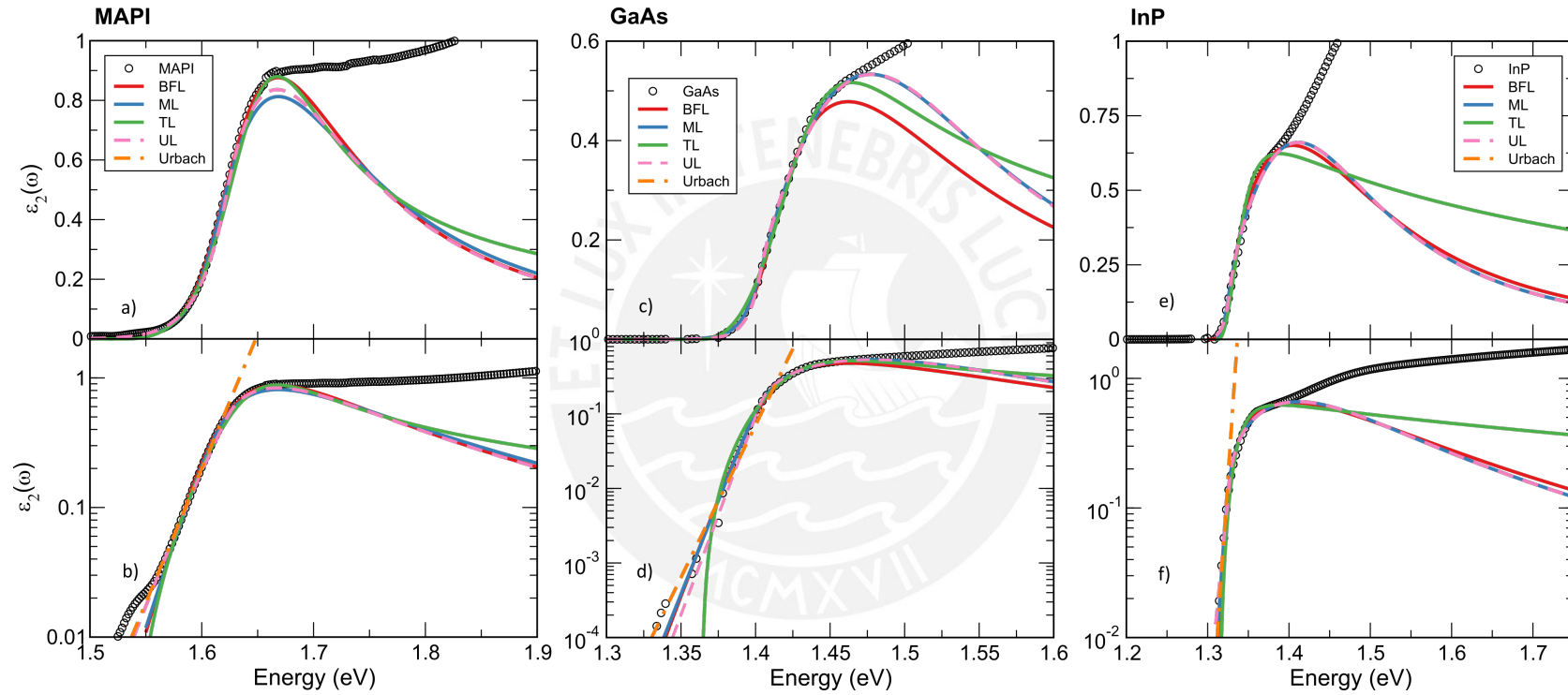
Fig. 2.4 First oscillator of the imaginary part of the electrical permittivity, in normal and logarithmic scale, compared with the different theories, the BFL, ML, TL and UL for direct electronic transitions materials: MAPI (a,b), GaAs (c,d) and InP (e,f).

After this procedure, we replace the first oscillator by the corresponding to the other models for direct electronic transitions materials, i.e. UL and ML. Additionally, we use the TL model for the fundamental absorption for comparison purposes. Fig. 4, depicts the fits of the 2.4. The plots regarding the first oscillator in linear and logarithmic scales for MAPI, GaAs and InP.

The MAPI $\tilde{\varepsilon}_2$ spectrum was fitted by using 1 BFL and 3 TL oscillators as is shown in figure 2.3-a,b. The oscillators parameters are shown in table 2.1. The best fitted bandgap values are similar for BFL, ML and UL, while a shift of 90 meV is observed after the TL model. These values are in agreement with the reported of 1.60 eV [56, 194, 94], and 1.63 eV [150]. We also obtain similar parameters of central energy (E_c) and damping factor (B) for the BFL, UL and ML models. This explains the similar curves for the high absorption region in figures 2.4-a,b only differentiated by the coefficient A. Also, differences in the fitted Urbach energy (E_β) values are expected, nevertheless, the fit with the BFL is the closest to previous reports [83]. For comparison purposes, the central energies of the TL oscillators are also depicted in table 2.1.

The GaAs spectra showed in 2.3-c,d was analysed with 1 BFL and 5 TL oscillators. The best fitted parameters are shown in table 2.2. Note that the bandgap is the same for BFL, ML and UL models, whilst its shifted in the TL model by 40 meV. The bandgap values are close to previous reports of 1.422 eV [7], 1.41 eV [177], 1.44 eV [11] and 1.43 eV [76]. In the case of the 1st oscillator, the ML and UL model share almost all parameters except for the Urbach energy whose value is doubled in the case of the UL model. This is somehow expected as depicted in the exponential slopes of figure 2.2. A similar behaviour is reported for BFL and UL models. Both models predict the same Urbach tail but differ in the high absorption region due to the difference of E_c and A. On the other hand, the Urbach energy found in literature is of 7.5 meV [72], which is in close agreement with the one obtained after fitting the BFL and UL models. For comparison purposes, the TL oscillators central energies are also presented in table 2.2.

The InP imaginary electrical permittivity shown in 2.3-e,f was fitted by using 1 BFL and 4 TL oscillators. The best fitted parameters are written in table 2.3. The bandgap values for the first oscillator are the same for all models, within a difference of 10 meV, even for TL. In this case, the TL curve tries to cover the steep slope observed in figures 2.4-e,f. The fitted bandgap values are close to the previously reported values of 1.27 eV [76], 1.343 [7], and 1.35 eV [63], 1.37 eV [159]. Fits with the ML and UL models exhibit similar best fitted parameters, as in the case of GaAs, except for the Urbach energy. The Urbach energy of 5.11 meV retrieved from the UL model is the closest to the previously reported result of 7.1 meV [7]. Finally, the central energies for the TL oscillators are collected in table 2.3.

Table 2.1 MAPI parameters for the BFL, TL, ML and UL used for the fundamental oscillator (N=1). And the TL parameters for the Nth oscillators.

N	1st				2nd	3rd	4th
	BFL	TL	ML	UL	TL		
E_β (meV)	19.80 (37)	-	10.94 (13)	23.8 (15)	-	-	-
A	2.68 (25)	18.8 (45)	2.31 (14)	2.41 (12)	33 (24)	15.5 (13)	53 (12)
Eg (eV)	1.62 (1)	1.53 (2)	1.62(0)	1.61 (0)	1.65 (4)	1.49 (4)	2.48 (6)
Ec (eV)	1.62 (1)	1.64 (1)	1.63 (0)	1.62 (1)	1.68 (5)	2.55 (1)	3.18 (3)
B	0.17 (1)	0.12 (2)	0.17 (0)	0.20 (0)	0.28 (16)	0.86 (2)	0.81 (7)

Table 2.2 GaAs parameters for the BFL, TL, ML and UL used for the fundamental oscillator (N=1). And the TL parameters for the Nth oscillators.

N	1st				2nd	3rd	4th	5th	6th
	BFL	TL	ML	UL	TL				
E_β (meV)	8.58 (50)	-	4.60 (27)	8.62 (49)	-	-	-	-	-
A	1.10 (15)	19.8 (86)	1.07 (8)	0.90 (5)	35.2 (16)	35.88 (52)	36.08 (53)	39.06 (12)	52.2 (11)
Eg (eV)	1.40 (0)	1.36 (2)	1.40 (0)	1.39 (0)	1.43 (1)	1.60 (1)	1.96 (0)	2.31 (0)	2.12 (1)
Ec (eV)	1.42 (1)	1.42 (1)	1.44 (1)	1.46 (0)	1.43 (1)	1.76 (1)	2.68 (1)	2.91 (0)	3.15 (1)
B	0.21 (1)	0.11 (2)	0.23(1)	0.22 (1)	0.38 (1)	1.30 (7)	0.98 (1)	0.19 (0)	0.42 (0)

Table 2.3 InP parameters for the BFL, TL, ML and UL used for the fundamental oscillator (N=1). And the TL parameters for the Nth oscillators.

N	1st				2nd	3rd	4th	5th
	BFL	TL	ML	UL	TL			
E_β (meV)	4.34 (13)	-	2.31 (7)	5.11 (0)	-	-	-	-
A	1.45 (6)	69.9 (89)	1.38 (5)	1.33 (4)	23.3 (33)	42.7 (54)	29.2 (22)	36.13 (86)
Eg (eV)	1.32 (0)	1.31 (1)	1.32 (0)	1.32 (0)	1.37 (1)	1.46 (1)	1.78 (2)	1.77 (5)
Ec (eV)	1.37 (1)	1.32 (0)	1.37 (0)	1.37 (0)	1.45 (1)	1.53 (4)	2.46 (3)	3.20 (1)
B	0.30 (1)	0.06 (1)	0.28 (1)	0.28 (1)	0.23 (2)	0.90 (7)	1.53 (3)	0.49 (0)

Table 2.4 GaP parameters for the BFL, TL, ML and OL used for the fundamental oscillator (N=1). And the TL parameters for the Nth oscillators.

N	1st				2nd	3rd	4th	5th
	BFL	TL	ML	OL	TL			
E_β (meV)	20.8 (45)	-	45.3 (26)	21.1 (18)	-	-	-	-
A	4.0 (30)	0.65 (2)	3.62 (27)	5.02 (72)	3.99 (72)	45.88 (50)	117.1 (20)	78.1 (37)
$Eg(eV)$	2.19 (4)	2.14 (0)	2.20 (0)	2.19 (1)	2.27 (0)	2.47 (1)	2.68 (0)	2.64 (2)
$Ec(eV)$	2.21 (3)	2.27 (0)	2.24 (0)	2.19 (1)	2.25 (1)	3.6 (41)	2.72 (1)	3.71 (0)
B	0.24 (8)	0.29 (0)	0.23 (1)	0.22 (2)	0.79 (3)	1.9 (26)	0.32 (1)	0.29 (1)

2.3.2   Indirect Semiconductors
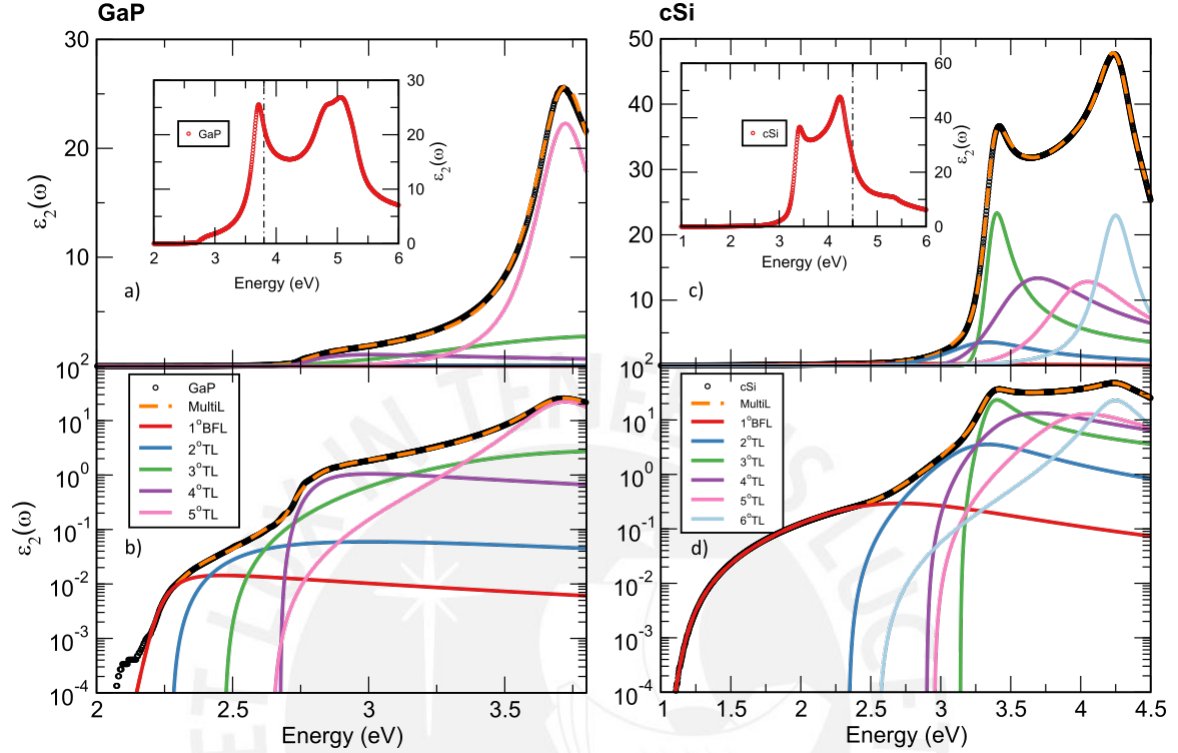
Fig. 2.5 Imaginary part of the electrical permittivity of gallium phosphide (GaP) (a,b) and cristalline silicon (cSi) (c,d). The experimental data (o) and fits using multiple Lorentz oscillators (Lorentz oscillators are presented as — ; while the sum is - - -) are illustrated on a linear and a semi-logarithmic scale. The insets in these figures show the full range of values from the VIS to UV. Here, the dashed lines represents the cutoff energy taken for the analysis.

The imaginary part of their electrical permittivity was extracted from SpectraRay libraries. GaP $\tilde{\varepsilon}_2$ data was extracted from Aspnes et al. [3], and the corresponding for c-Si was selected from the UV-NIR data. These are shown in figure 2.5 in linear and logarithmic scale. The fitting procedure employed was the same as for direct semiconductors. We have used the BFL model for fundamental absorption and N^{th} TL oscillators for higher electronic transition energies. The cutoff energy is depicted in the inset of figures 2.5-a,c, for each case. Fits of the first oscillator using the BFL, OL and ML models are shown in figure 2.6-a,b,c,d for linear and logarithmic scale.
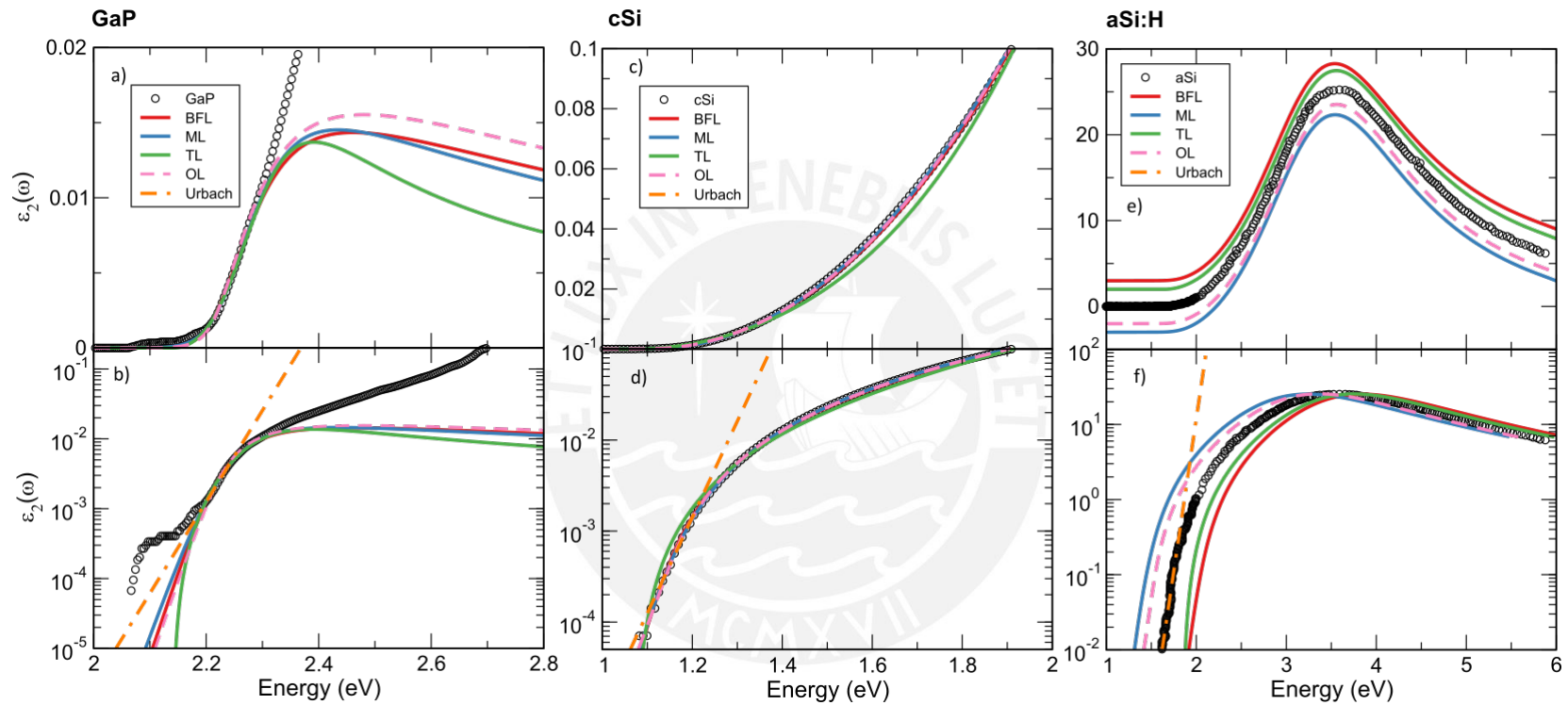
Fig. 2.6 First oscillator of the imaginary part of the electrical permittivity, in normal and logarithmic scale, compared with the different theories, the BFL, ML, TL and UL for direct electronic transitions materials: GaP (a,b), cSi (c,d) and aSi (e,f). Notice that for clarity purposes, the electrical permittivity of the models is shifted in (e) by an amount of ± 3 and ± 2 units. This is repeated for the energy in (f) with amounts of ± 0.3eV and ± 0.2eV.

The GaP $\tilde{\varepsilon}_2$ spectrum was fitted using 1 BFL and 4 TL oscillators as shown in figure 2.5-a,b. The fundamental absorption is only seen in the logarithmic scale due to the small components of the transition matrix element for the phonon assisted transition. Best fitted parameters are written in table 2.4. Bandgap values are close between the BFL, ML and OL models and differ about 50 meV with respect to TL model. The value of the ML model of 2.20 eV is the closest to the 2.26 eV reported, at room temperature, in Lorenz et al. [90], calculated with the Elliott model. The first oscillator exhibits virtually the same best fitted parameters between the ML and OL models, except for the amplitude and Urbach energy, the latter is expected since models differ in the functional form of the Urbach tail. Figure 2.6-a,b depicts the aforementioned fits.

c-Si $\tilde{\varepsilon}_2$ data was fitted with 1 BFL and 5TL oscillators. This is shown in figure 2.5-c,d. The best fitted parameters are written in table 2.5. The small fundamental indirect absorption is only visible in logarithmic scale as in the case of GaP. The retrieved bandgap value of 1.12 eV is shared between the BFL, TL and OL models, while a shift of 50 meV is observed for TL model. This value is in agreement with the well known value of 1.11 eV [76], and 1.124 eV calculated with the free-exciton absorption at room temperature [12]. The Urbach tail calculated with the BFL, ML and OL models gives values in the range of 23.92-43.34 meV, which differs from the literature value of 9.6 meV of [20] and 12 meV of [95]. This apparent difference can be attributed to the sensitivity of the optical measurements used in the studies of Cody and MacFarlane and the differences between the distinct models incorporating Urbach tails.

2.3.3 Amorphous Silicon

The fitting procedure used for Amorphous materials is the same as for indirect electronic transitions materials. Here we analyze a-Si:H. Absorption data was extracted from Jackson et al. [67]. This is shown in figure 2.6-e,f. Note the shape of a single oscillator in ε_2. The best fitted parameters are collected in table 2.6. A similar bandgap energy is obtained for all models. Here, the BFL value is the closest to the reported bandgap of 1.72 eV calculated with the Tauc's dispersion equation in samples of a:Si with 14% of hydrogen [20]. From the functional behavior (see figure 2.6-e,f), the central energy E_c and broadening factor B have similar values for all models. Lastly, the Urbach energy of BFL and OL models are the closest to Cody's value of 45 meV [20].

Table 2.5 c-Si parameters for the BFL, TL, ML and OL used for the fundamental oscillator (N=1). And the TL parameters for the Nth oscillators.

N	1st				2nd	3rd	4th	5th	6th
	BFL	TL	ML	OL	TL				
E_β (meV)	23.92(14)	-	43.34(40)	32.63(23)	-	-	-	-	-
A	3.79(24)	0.98(1)	3.82(4)	3.76(3)	33.91(82)	1008(6)	302.9(61)	145.4(8)	48.5(17)
Eg (eV)	1.115(0)	1.070(0)	1.115(1)	1.12(1)	2.34(1)	3.14(0)	2.90(1)	2.95(4)	2.55(3)
Ec (eV)	2.66(2)	2.45(1)	2.65(1)	2.64(1)	3.24(1)	3.36(0)	3.50(1)	3.96(0)	4.24(0)
B	1.71(2)	1.18(2)	1.76(2)	1.72(1)	0.78(1)	0.21(0)	0.83(1)	0.77(1)	0.34(0)

Table 2.6 a-Si:H parameters for the BFL, TL, ML and OL used for its single oscillator, the fundamental N=1.

N	1st			
	BFL	TL	ML	OL
E_β (meV)	48.5 (99)	-	82.80 (99)	53.20 (41)
A	526.5 (45)	194.5 (12)	516.4 (52)	495.1 (33)
Eg (eV)	1.69 (0)	1.65 (1)	1.68 (0)	1.67 (0)
Ec (eV)	3.40 (1)	3.44 (0)	3.41 (1)	3.43 (1)
B	2.12 (2)	2.11 (1)	2.11 (3)	2.06 (2)

2.3.4   Dimensionless comparison
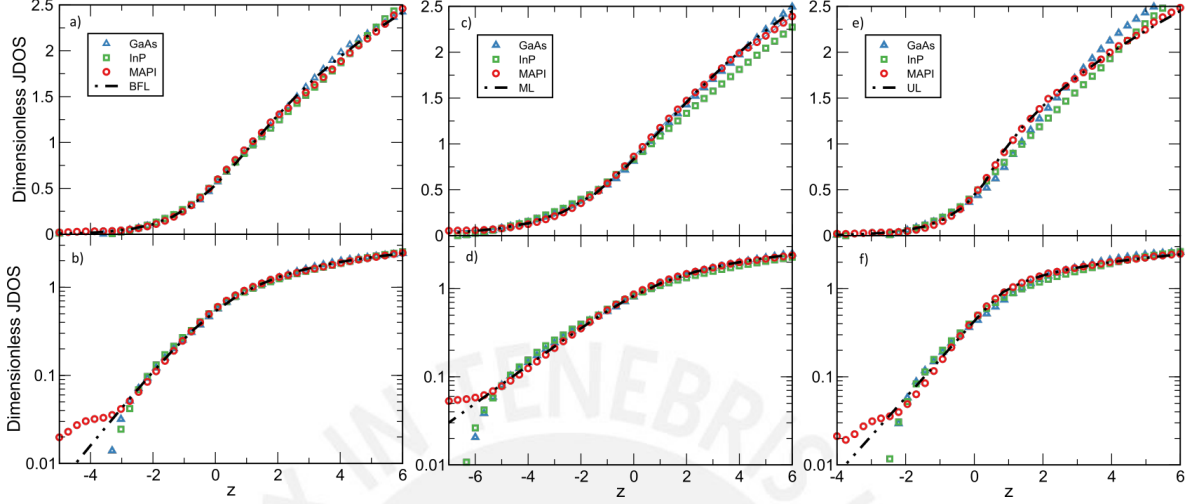
Fig. 2.7 Dimensionless JDOS ($\mathscr{D}_{cv}$) for direct electronic transitions materials (GaAs, InP and MAPI), in normal and logarithmic scale, compared with the dimensionless models such as BF-Lorentz (a,b), Monolog-Lorentz (c,d) and Ullrich-Lorentz (e,f).

We now carry out a dimensionless analysis for direct, indirect (amorphous) transition materials. This is presented in figures 2.7 and 2.8, respectively. The data were brought to a dimensionless scale by using the following procedure. We first subtract the high energy Lorentz oscillators from the data, then we divide this result with an energy dependent function that takes the form of $CL(E)/(E\sqrt{\beta})$ and $\tilde{C}L(E)/(E\beta^2))$ for direct and indirect transition materials, respectively. This left us, for example, with the shape of the polylogarithm and logarithm functions for the BFL and ML models, respectively. The objective of this analysis is to contrast the different models, on the same dimensionless scale, as well as the resulting fits of ε_2 of different materials in a single picture. Figures 2.7 and 2.8 depict the dimensionless JDOS curves along with the spectral data of each direct and indirect (amorphous) material brought into this scale, respectively. Differences observed are attributed to the model goodness. In the particular case of c-GaP, the Urbach tail region data could be close to the spectral sensitivity of the instrument. Nevertheless, sample properties such as thickness impact in the determination of the absorption edge, due to strong absorbance.

2.3.5   Urbach slope

In this subsection we analyze in detail the Urbach slope of the different presented models and compare them with the Urbach tail obtained with the traditional Urbach rule model, for comparison purposes. The comparison between the Urbach energy for direct $E_{\beta_{dir}}$ and
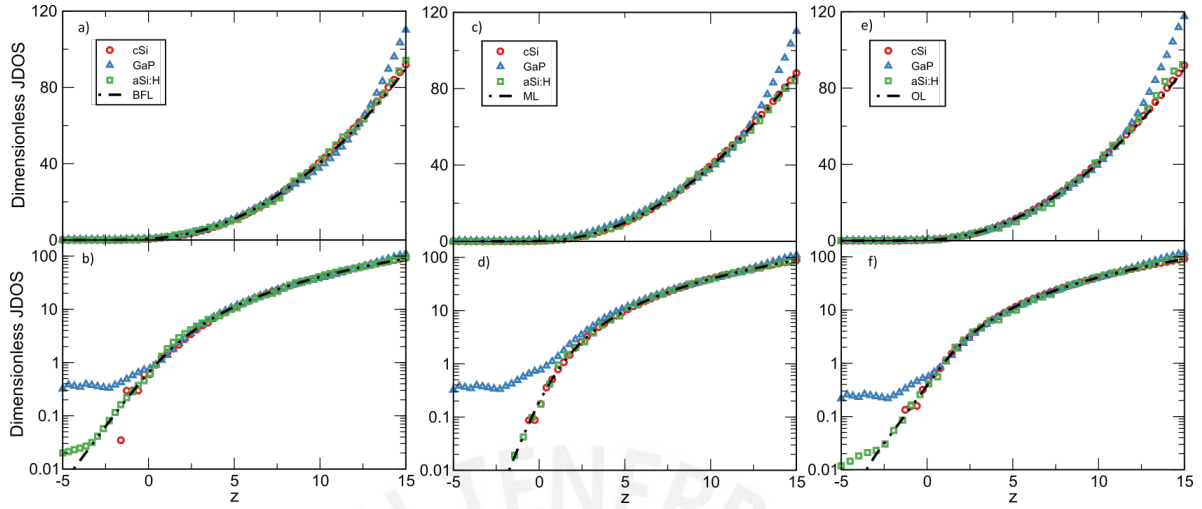
Fig. 2.8 Dimensionless JDOS ($\mathscr{J}_{cv}$) for indirect electronic transitions materials (GaP and c-Si) and amorphous Si:H, in normal and logarithmic scale, compared with the dimensionless models such as BF-Lorentz (a,b), Monolog-Lorentz (c,d) and O'Leary-Lorentz (e,f).

indirect $E_{\beta_{ind}}$ semiconductors with the Urbach energy from the Urbach rule (E_U) is shown in fig. 2.9 a and b, respectively. In both cases we see that Urbach energies depicted with the models are shifted when compared to E_U. This shift is larger for larger Urbach energies for direct and indirect transition materials. The E_U for the direct MAPI, GaAs and InP is 20.7 meV, 10.47 meV and 4.7 meV, respectively. These values are in agreement with other previous results using the Urbach rule. For instance, the literature reports are 14 meV [83] for MAPI, 7.5 meV [72] for GaAs, and 7.1 meV [7] for InP.

From figure 2.9-a, it can be noticed that the BFL and ML models tend to behave linearly, based on only three points, when compared with E_U. This suggest a correct function-ability of the PolyLog in the Urbach region and capacity to compare E_U values with previous reports. On the other hand, the Urbach energies for the UL model are similar to the BFL for InP and GaAs, except for MAPI. Lastly, the disorder energy of ML model is half the value derived from the Urbach rule for all materials.

In the case of indirect/amorphous materials (see figure 2.9-b), the Urbach energies computed with the Urbach rule are 52 meV, 39.7 meV and 32.7 meV for a-Si:H, c-Si and GaP, respectively. Previous reported values are 45 meV and $9.6 - 12$ meV for a-Si:H and c-Si, respectively [20, 95], but these can vary depending on the growing process, defects concentration and deposition temperature [34, 129].

In the case of GaP, the $E_{\beta_{ind}}$ is the same for the BFL and OL models. Its value is the half of the one retrieved by the ML model. This behavior is repeated in the case of a-Si:H
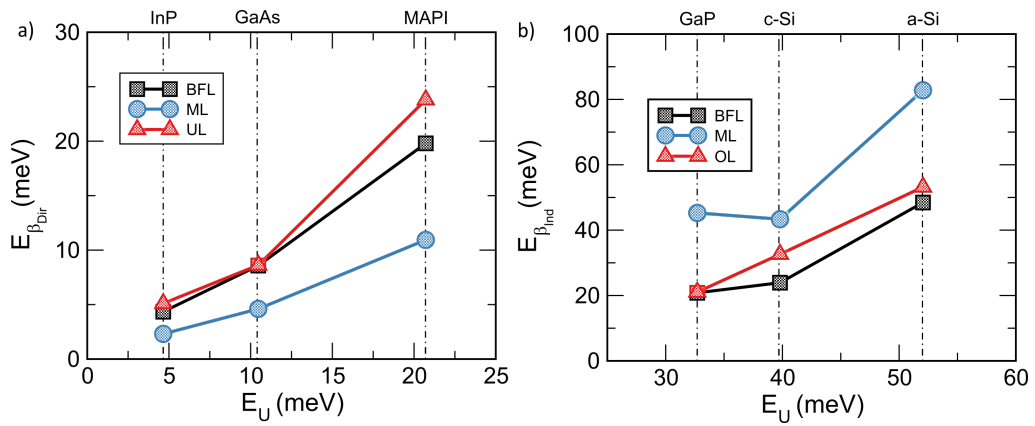
Fig. 2.9 Urbach energies calculated with BFL/ML/UL(OL) models plotted versus the traditional Urbach energy extracted from the Urbach's rule (eq. 2.10). The case of direct electronic transitions materials is shown in (a) and indirect/amorphous materials are shown in (b).

where the BFL and OL models are the closest to the value of E_U, while the ML differs by an amount of 30 meV.

Chapter 3

The Sommerfeld Enhancement Factor: The EBF Model

Our understanding of absorption edge in excitonic semiconductors is essential for PV technology. Important optical parameters such as the binding energy, Urbach energy and bandgap can be extracted from this part of the absorption spectrum. For example, Urbach tail states have an impact on devices based on amorphous and polycristalline semiconductors [56, 57, 166, 180, 2]. In the same way, excitons have a profound impact in the operation mechanism of excitonic solar cells [55], where free charge transport is a result of the thermal dissociation of excitons into free electrons and holes [6]. In the peculiar case of a planar architecture of an excitonic solar cell, such as in the ones used for perovskites, the configuration involves two carrier selective material layers with a wide bandgap which sandwiches the central layer of the excitonic semiconductor [4]. The energy band difference of these layers overcome the exciton binding energy forcing it to disassociate [6]. For this reason, knowledge of the binding energy can be helpful to engineer the excitonic solar cell architecture like the ones based on perovskites.

The binding energy measurement encloses experimental techniques such as absorption, photoluminescence (PL) and magneto-absorption. For instance, when these techniques are applied to tri-halide perovskites, they show a large range of values [49] like in the cases of MAPbBr$_3$ and MAPbI$_3$, where the reported values go from 15 to 76 meV and 5 to 50 meV, respectively [201, 145, 164]. At first sight, this behavior can be attributed to the different experimental conditions. However, there is a fundamental aspect of perovskites that is needed to be taken into account. The polar nature of perovskites defines a broad difference in the static and infinity electrical permittivities [154, 6]. This in combination with the low LO phonon energy results in a weak electron-phonon coupling. This explanation could satisfy the large discrepancy as stated in Soufiani et al. [154]. However, even with this understanding of

the underlying mechanism of the reported discrepancies, we have no tool for extracting the precise exciton binding energy.

$$\alpha(\hbar\omega) \approx \frac{1}{\hbar\omega} \left(\sum_{n=1}^{\infty} \frac{2R^*}{n^3} \mathscr{G}\left(E_{x_n} - \hbar\omega\right) + \int_{E_g}^{\infty} \frac{\mathscr{G}\left(E - \hbar\omega\right)}{1 - e^{-2\pi\sqrt{\frac{R^*}{E-E_g}}}} dE \right) \tag{3.1}$$

$$E_{x_n} = E_g - \frac{R^*}{n^2} \tag{3.2}$$

Usually, the procedure for extracting the binding energy from absorption measurements is based on the Elliott formula presented in eq. (3.1). This expression have two terms arising from the discrete and continuum contributions to the absorption. Moreover, contributions from the thermal disorder and the uncertainty principle broadening can be modeled by the function $\mathscr{G}(z)$, presented in eq. (3.1), producing in particular non-analytic expressions.

The Elliott model is a description of the fundamental absorption when the Coulomb interaction is turned on. Here, the dissipation rate energy from the photon field is completely determined by the conversion rate of photons into excitons [204, 32]. As a result, the transition probability per volume is written in terms of the excitonic wave functions (Wannier waves) [189, 45]. These waves correspond to the well known hydrogen atom solutions for bound, $\hbar\omega \ll E_g$, and unbound, $\hbar\omega \gg E_g$, cases. The former results in discrete exciton binding energies that depend on the e-h reduced mass. Whereas, the latter corresponds to a continuous range of energies above the bandgap [32]. For energies larger than the bandgap, $\hbar\omega \gg E_g$, the continuous part is proportional to $\sqrt{\hbar\omega - E_g}$ and $(\hbar\omega - E_g)^2$ for direct and indirect semiconductors, respectively [32]. Despite the success, eq. (3.1) shows a non-analytic expression depending on the belly distribution $\mathscr{G}(\hbar\omega)$ used to introduce broadening effects [154]. This distribution, e.g., can take the form of a Gaussian to model the effect of thermal deviations, and, a Lorentzian to account for the uncertainty principle.

Here, I propose an alternative to Elliott's equation, based on the formulation of band-fluctuations (BF) model [58]. The treated band-fluctuations arise from disorder-induced local variations of the band edges, thermally-induced potential fluctuations, lattice vibrations and other deviations from the perfect periodicity of the lattice [56, 58]. This process results in an analytic expression (here named EBF model). Contrary to the non-analytic versions of Elliott model when convoluted with the Gaussian, Lorentzian or the hyperbolic secant distributions. The equation, which is described in section two, contains a belly shaped peak for the discrete states, and a continuous function that grows more slowly than $\sqrt{\hbar\omega - E_g}$ for high energies, $\hbar\omega \gg E_g$.

Section 3.1 starts with a brief discussion of the Elliott model. This settle the basis for the new EBF model developed in section 3.2. In section 3.3 and 3.4, the new model is compared

with a similar one developed by Soufiani et al. Lastly, in section 3.5 we apply our EBF model to the absorption of excitonic semiconductors for several temperatures. Here, we have selected GaAs, and the tri-halide perovskites based on methylammonium, MAPbX$_3$ (X=Pb,I,Cl). GaAs was selected for its well known bandgap, E_g, and characteristic exciton binding energy, R^*, for comparison purposes. And, the tri-halide perovskite family was selected due to its applications in excitonic solar cells and light-emitting diodes (LEDs) [99], as well as due to the intriguing variability of the binding energy caused by their polar nature [6, 154]. With this materials, we aim to test the applicability of the EBF model for excitonic, polar and non-polar, materials. Nonetheless, this analysis can be extended to other polar excitonic materials like the organic compounds and n-type semiconductors like ZnO, SnO2, among others, which are the base for Transparent Conductive Oxides (TCOs).

3.1   Brief summary of the Elliott model

The Elliott model describes exciton states as an hydrogen atom. In this picture, the electron is excited from the valence to the conduction band leaving a hole behind. They interact trough the Coulomb potential producing a quasi-particle, known as exciton. This produces new energy levels in the region between the conduction and valence bands. As a consequence, the exciton system absorbs light for energies below the bandgap. These states correspond to the bound solutions. On the other hand, the unbound states are formed when the photon energy is larger than the band edge [204, 32, 104]. The optical transition rate per unit volume and per unit time for converting a photon into an exciton is given by:

$$R_{cv} = \frac{2\pi}{\hbar} \sum_f |\langle f| \mathscr{H}_{xR} |0\rangle|^2 \delta(E_f(K) - E_0 - E). \qquad (3.3)$$

Here the photon energy is $E = \hbar\omega$, the exciton-photon interaction is expressed by $\mathscr{H}_{xR}$, the initial state with no excitons is $|0\rangle$, and, the final state is $\langle f|$. This state represents an exciton with energy E_f and wave vector K:

$$E_f(K) = \frac{\hbar K^2}{2\mu} - \frac{R^*}{n^2} \approx -\frac{R^*}{n^2}, \qquad (3.4)$$

Here μ is the electron-hole reduced mass (exciton mass), R^* is the exciton Rydberg constant in terms of μ, $R^* = \mu e^4 / 2\hbar^2 (4\pi\varepsilon_0)^2$, and n is the exciton energy level. The wave vector K is the sum of the electron k_e and hole k_h. And, in the case of direct transitions, neglecting the photon momentum, the wave vector conservation is reduced to $k_e = -k_h = k$. This produces

a total wave vector of $K = 0$ [32] as seen in the right hand of eq. (3.4). As a consequence, the final energy depends only on the nth state.

For optical transitions, we have the allowed and forbidden transitions depending on the nature of the hydrogen wavefunction. The allowed transitions are the ones we observe in the optical measurements and corresponds to the s-like states. On the other hand, the forbidden transitions, described by p-like states, are usually called dark excitons due to its minuscule amplitude in the optical spectrum. This is a consequence of the amplitude being inversely proportional to the excitonic radius which is of the size of several unit cells [189]. For this reason, our study is focused on the allowed transitions that shape the fundamental absorption. The interaction potential for these transitions, $\langle f | \mathcal{H}_{xR} | 0 \rangle$, can be expressed in terms of the conduction (ψ_k^c) and valence (ψ_k^v) Bloch wave-functions, i.e.,

$$|\langle f | \mathcal{H}_{xR} | 0 \rangle|^2 = NV |\phi_{nlm}(0)|^2 |\langle \psi_k^c | \mathcal{H}_{eR} | \psi_k^v \rangle|^2. \tag{3.5}$$

Eq. (3.5) states that the probability of exciting an exciton optically is proportional to the overlap of the electron and hole wavefunctions. Here N is the number of unit cells. V is the volume of a unit cell. $\phi_{nlm}(r)$ is the analytic solution for two spherical single bands with effective masses m_e and m_h [32]. This implies that the hydrogen atom solutions can describe the new final states, f. As a consequence, the solution is in terms of the coefficients n, l, m which are the principal, orbital and magnetic quantum numbers. And, the opposite momentum of the electron and hole produces solutions independent of the relative position, $\phi_{nlm}(r = 0)$. Lastly, the electric interaction $\mathcal{H}_{eR}$ follows the behavior of a dipole [32], i.e.,

$$|\langle \psi_k^c | \mathcal{H}_{eR} | \psi_k^v \rangle|^2 = \left(\frac{e|\vec{E}|}{2m_e\omega} \right)^2 |\langle \psi_k^c | \hat{\mathbf{e}}.\vec{\mathbf{p}} | \psi_k^v \rangle|^2, \tag{3.6}$$

with e and m_e being the electron charge and effective mass, ω is the photon frequency, $\vec{E}$ is the external electric field amplitude, and $\hat{e}$ is the unit vector of the polarization.

For the term $\phi_{nlm}(0)$ in eq. 3.5, the only non-vanishing expressions are the S-like states ($l, m = 0$). Thus, implying that excitons will have S symmetry when formed. For energies below the bandgap, the bound allowed solutions for the hydrogen atom are:

$$|\phi_{n00}(0)|^2 = 1/(NV\pi(a_0 n)^3). \tag{3.7}$$

Here a_0 is the Bohr radius for an exciton with reduced mass $\mu^{-1} = m_e^{-1} + m_h^{-1}$.

The transition rate for the exciton formation is

$$R_{cv}^d = \mathscr{R}_d |P_{cv}|^2 \sum_{n=1}^{\infty} \frac{1}{n^3} \delta(E - E_{x_n}), \tag{3.8}$$

with

$$R_{cv}^d = \mathscr{R}_d |P_{cv}|^2 \sum_{n=1}^{\infty} \frac{1}{n^3} \delta(\hbar\omega - E_{x_n}), \tag{3.9}$$

and with

$$\mathscr{R}_d = \frac{\mu^3 e^8 |\vec{E}|^2}{m_e^2 \omega^2 \hbar^7 (4\pi\varepsilon_0)^3}. \tag{3.10}$$

The exciton peak location is $E_{x_n} = E_g - \frac{R^*}{n^2}$, and the matrix element is $P_{cv} = \langle \phi_k^c | \hat{\mathbf{e}}.\vec{\mathbf{p}} | \phi_k^v \rangle$. In addition, a factor of two has been included to count the spin degeneracy. The super/sub-script d has been added to refer to the discrete scenario.

For the continuous part, the employed solutions will correspond to the unbound energy states of the hydrogen atom written in terms of the hyper-geometric wavefunctions, $R(r)$ [204, 148]. As in the previous case, we pick the $r = 0$ solution, i.e.,

$$R(0) = \kappa\pi \frac{e^{\pi\kappa}}{(NV)^2 \sinh(\pi\kappa)}, \tag{3.11}$$

where κ is $\sqrt{R^*/(E - E_g)}$. The interaction term can be written as:

$$|\langle f | \mathscr{H}_{xR} | 0 \rangle|^2 = \left(\frac{e|\vec{E}|}{2m_e\omega} \right)^2 \frac{\kappa\pi e^{\pi\kappa}}{NV \sinh(\pi\alpha)} |P_{cv}|^2. \tag{3.12}$$

The energy difference of the final and initial states, $E_f(K) - E_0$, becomes the difference from the valence and conduction band, $E_c - E_v = E_{cv}$. As a consequence, the sum over the continuum of energies transform the discrete summation into an integral, in terms of the Density Of States (DOS) for direct transition semiconductors, D_{cv}, i.e.,

$$\sum_f \delta(E_{cv} - E) \rightarrow \int NV D_{cv}(E_{cv}) \delta(E_{cv} - E) dE_{cv}, \tag{3.13}$$

with

$$D_{cv}(E_{cv}) = \frac{\sqrt{2}\mu^{3/2}}{\pi^2\hbar^3} \sqrt{E_{cv} - E_g}\,\Theta(E_{cv} - E_g). \tag{3.14}$$

Thus, the transition rate for the continuous case (c) is:

$$R_{cv}^c = \frac{2\pi}{\hbar}\left(\frac{e|\vec{E}|}{2m_e\omega}\right)^2 \frac{\kappa\pi e^{\pi\kappa}}{\sinh(\pi\kappa)}|P_{cv}|^2 D_{cv}(E), \tag{3.15}$$

and by substituting eq. (3.14),

$$R_{cv}^c = \mathscr{R}_c|P_{cv}|^2 \frac{\kappa\sqrt{E-E_g}e^{\pi\kappa}}{\sinh(\pi\kappa)}, \tag{3.16}$$

$$= 2\mathscr{R}_c|P_{cv}|^2 R^* \frac{1}{1-e^{-2\pi\kappa}}, \tag{3.17}$$

with,

$$\mathscr{R}_c = \frac{\sqrt{2}\mu^{3/2}}{2\hbar^4}\left(\frac{e|\vec{E}|}{m_e\omega}\right)^2. \tag{3.18}$$

From eqs. (3.9) and (3.17), we can write the expression for the absorption given the relation between the transition rate and imaginary part of the electrical permittivity:

$$\varepsilon_i = \frac{8\pi\hbar R_{cv}}{|\vec{E}|^2}. \tag{3.19}$$

Thus, the absorption coefficient is:

$$\alpha = \frac{\omega\varepsilon_i}{4\pi\varepsilon_0\hat{n}c} = \frac{2\hbar\omega R_{cv}}{\varepsilon_0|\vec{E}|^2\hat{n}c}. \tag{3.20}$$

Here, $\hat{n}$ is the real part of the refractive index, and c is the speed of light. The total absorption coefficient is the sum of the discrete and continuum parts [32, 142]. This is left in terms of the exciton Rydberg constant for fitting purposes.

$$\alpha(E) = \alpha_d(E) + \alpha_c(E), \tag{3.21}$$

$$\alpha(E) = \frac{\mathscr{A}}{E}\left(2R^*\sum_n \frac{1}{n^3}\delta(E-E_{x_n}) + \frac{1}{1-e^{-2\pi\sqrt{\frac{R^*}{E-E_g}}}}\right). \tag{3.22}$$

with

$$\mathscr{A} = \frac{8\hbar(4\pi\varepsilon_0)^3 R^{*2}}{\varepsilon_0 e^4 m_e^2 \hat{n}c}|P_{cv}|^2. \tag{3.23}$$

In addition, eq. (3.23) it is commonly convoluted with a belly shaped function $\mathscr{G}(E-\hbar\omega)$ for adding the thermal and uncertainty principle contributions. For instance, a Gaussian and Lorentizan are used in Soufiani et al. [154], whilst a hyperbolic secant is used in Saba et al.

[133]. The final version of the Elliott equation can be expressed as [145, 201, 132]:

$$\alpha(\hbar\omega) = \frac{\mathscr{A}}{\hbar\omega}\left(2R^*\sum_n \frac{1}{n^3}\mathscr{G}\left(E_{x_n} - \hbar\omega\right) + \int_{E_g}^{\infty} \frac{\mathscr{G}\left(E - \hbar\omega\right)}{1 - e^{-2\pi\sqrt{\frac{R^*}{E - E_g}}}}dE\right). \qquad (3.24)$$

This convolution process is similar to the band-fluctuations model performed for the optical absorption of non-excitonic materials [58]. In the BF model, a convolution can be applied to the density of states for producing the tail states of the Urbach region. Likewise, the BF model can be applied directly to the absorption coefficient producing a similar expression to eq. (3.24) for non-excitonic materials. In the BF model, the fluctuations around the bandgap are attributed to disorder, thermal or lattice deformations. These are modeled in terms of a Gaussian [135, 115, 116] or by using a distribution inspired on the derivative of the Fermi distribution [58]. In this work, we follow the latter due to its success describing the absorption edge of direct, indirect and amorphous non-excitonic semiconductors [58, 56, 57]

3.2 The Elliot-Band-Fluctuations (EBF) model

The idea of potential fluctuations were proposed initially to model a semi-classical density of states for heavily doped semiconductors [73], later adopted by Dunstan in [31]. This formalism was applied to the optical absorption, by using Gaussian distribution, for the description of the exponential Urbach tails [135]. Later, O'leary et al. deduce an expression for the optical absorption in amorphous materials [115, 116]. Whereas, Guerra et al. use an alternative distribution for modeling the absorption edge on direct, indirect and amorphous semiconductors. This was recently extended for generalizing and modeling high absorption energy absorption regions a recently published work, Lizarraga et al [88]. Here, we model the fluctuations accordingly with the distribution given in Guerra et al., i.e., the distribution $\mathscr{G}(z)$ will acquire the form:

$$\mathscr{G}_{BF}(z) = \frac{1}{\sigma}\frac{e^{z/\sigma}}{(1 + e^{z/\sigma})^2}. \qquad (3.25)$$

Here, σ is the belly width. In the predecessor case, the obtained expressions for the absorption coefficient of non-excitonic direct and indirect materials are non-analytic. These models are written in terms of the polylogarithmic functions which are products of Fermi integrals that are computable numerically. The model produces excellent results when contrasted with experiments as shown in the works of Guerra and co-workers [58, 56, 57]. Following this success, we applied eq. (3.25) to the transition rate of excitonic materials.

Since the absorption in the presence of the Coulomb interaction has two contributions, it is important to remark that in the case of the discrete absorption, the broadening affects the exciton energy levels. Correspondingly, in the continuous case, these fluctuations act on the mobility edge further affecting the E_g determination. The discrete transition rate, eq. (3.9), is now:

$$\langle R_{cv}^d \rangle = \mathscr{R}_d |P_{cv}|^2 \sum_{n=1}^{\infty} \int_{E_{x_n}}^{+\infty} \frac{1}{n^3} \delta(E - E_{x_n}) \mathscr{G}_{BF}(E - \hbar\omega) dE. \tag{3.26}$$

Yielding to the following result:

$$\langle R_{cv}^d \rangle = \mathscr{R}_d |P_{cv}|^2 \sum_{n=1}^{\infty} \frac{1}{n^3} \mathscr{G}_{BF}(E_{x_n} - \hbar\omega). \tag{3.27}$$

For the transition rate of the continuum, eq. (3.17), we have:

$$\langle R_{cv}^c \rangle = \mathscr{R}_c |P_{cv}|^2 \int_{E_g}^{+\infty} \frac{\mathscr{G}_{BF}(E - \hbar\omega)}{1 - e^{-2\pi\sqrt{\frac{R^*}{E - E_g}}}} dE, \tag{3.28}$$

The procedure of solving this integration is the following. First, we write the full expression of eq. (3.28):

$$\langle R_{cv}^c \rangle = 2\sqrt{R^*} \mathscr{R}_c |P_{cv}|^2 \int_{E_g}^{+\infty} \frac{1}{1 - e^{-2\pi\sqrt{R^*/(\hbar\omega - E_g)}}} \frac{1}{\sigma} \frac{e^{(E - \hbar\omega)/\sigma}}{(1 + e^{(E - \hbar\omega)/\sigma})^2} dE. \tag{3.29}$$

We first make the substitutions of $x = E - E_g$ and $y = x + E_g - \hbar\omega = E - \hbar\omega$. The integral becomes:

$$\langle R_{cv}^c \rangle = 2\sqrt{R^*} \mathscr{R}_c |P_{cv}|^2 \int_0^{+\infty} \frac{1}{1 - e^{-2\pi\sqrt{R^*/x}}} \frac{1}{\sigma} \frac{e^{y/\sigma}}{(1 + e^{y/\sigma})^2} dx. \tag{3.30}$$

Now, we make the identity $b = 2\pi\sqrt{R^*}$, and apply integration by parts:

$$u = \frac{1}{1 - e^{-b/\sqrt{x}}} \quad \rightarrow \quad du = \frac{bx^{-3/2}e^{-b/\sqrt{x}}}{2(1 - e^{-b/\sqrt{x}})^2} dx,$$

$$dv = \frac{1}{\sigma} \frac{e^{y/\sigma}}{(1 + e^{y/\sigma})^2} \quad \rightarrow \quad v = -\frac{1}{(1 + e^{y/\sigma})}. \tag{3.31}$$

The integral in eq. (3.28) becomes:

$$I = \frac{1}{1 - e^{-b/\sqrt{x}}} \frac{-1}{1 + e^{y/\sigma}} \Big|_0^{+\infty} - \int_0^{+\infty} \frac{-1}{1 + e^{y/\sigma}} \frac{bx^{-3/2}e^{-b/\sqrt{x}}}{2(1 - e^{-b/\sqrt{x}})^2} dx, \tag{3.32}$$

$$I = \frac{1}{1 + e^{(E_g - \hbar\omega)/\sigma}} + \frac{b}{2} \int_0^{+\infty} dx \frac{1}{\sqrt{x^3}} \left(\frac{1}{e^{b/2\sqrt{x}} - e^{-b/2\sqrt{x}}} \right)^2 \left(\frac{1}{1 + e^{(x + E_g - \hbar\omega)/\sigma}} \right). \quad (3.33)$$

This can be solved by using the Sommerfeld expansion, i.e,

$$\int_0^{+\infty} H(x) \frac{1}{1 + e^{(x-\mu)/\sigma}} dx = \int_0^{\mu} H(x) dx + \frac{\pi^2}{6} \sigma^2 H'(x) \Big|_{x=\mu} + O\left(\frac{\sigma}{\mu} \right)^4. \quad (3.34)$$

Here, the variable μ is $\hbar\omega - E_g$. Likewise, the function $H(E)$ (see eq. 3.35) satisfies the two conditions for the expansion, it does not grow faster than polinomially in x when x goes to infinity, and, it vanishes in the limit of x approaching to zero.

$$H(x) = \frac{1}{\sqrt{x^3}} \left(\frac{1}{e^{b/2\sqrt{x}} - e^{-b/2\sqrt{x}}} \right)^2. \quad (3.35)$$

We neglect higher order terms, σ^2 ,in the Sommerfeld expansion, i.e,

$$\int_0^{+\infty} H(x) \frac{1}{1 + e^{(x-\mu)/\sigma}} dx = \int_0^{\mu} H(x) dx = \frac{2}{b \left(e^{b/\sqrt{\hbar\omega - E_g}} - 1 \right)}. \quad (3.36)$$

Lastly, we replace eq. (3.36) on eq. (3.33), and the transition rate for the continuum is:

$$\langle R_{cv}^c \rangle = 2\sqrt{R^*} \mathscr{R}_c |P_{cv}|^2 \left(\frac{1}{1 + e^{(E_g - \hbar\omega)/\sigma}} + \frac{1}{e^{2\pi\sqrt{R^*/(\hbar\omega - E_g)}} - 1} \right). \quad (3.37)$$

With eqs. (3.27) and (3.37), we can write the expression for the absorption coefficient following eq. (3.21). This will be denoted as α_{EBF} and have the form:

$$\alpha_{EBF}(\hbar\omega) = \frac{\mathscr{A}}{\hbar\omega} \left(2R^* \sum_n \frac{1}{n^3} \mathscr{G}_{BF}(E_{x_n} - \hbar\omega) + \frac{1}{1 + e^{(E_g - \hbar\omega)/\sigma}} + \frac{1}{e^{2\pi\sqrt{\frac{R^*}{\hbar\omega - E_g}}} - 1} \right). \quad (3.38)$$

Here $\mathscr{A}$ is the constant previously found on eq. (3.23). The main features of eq. (3.38) are its analytic form and the dependency on just 4 parameters. These are, the constant ($\mathscr{A}$), the bandgap (E_g), the belly width (σ), and the exciton binding energy (R^*).

3.3 Pseudo-Voigt Profile

The computed absorption of the EBF model arises from considering only thermally induced fluctuations. However, when experimental techniques are applied, the uncertainty principle produces a contribution as well. For instance, this is modeled as a Lorentzian in optic related

experiments. In this section we review a pseudo-Voigt procedure for the inclusion of two different broadening effects, which will be helpful for the extension of our model to embrace the uncertainty principle contribution. In 2015, Soufiani et al. propose a pseudo-Voigt profile for the Lorentzian and Gaussian profiles [154]. They arrive at an analytical expressions, after the convolution process, achieved by approximations [155]. Thus, the absorption coefficient looks like:

$$\alpha(\hbar\omega) = \eta\,\alpha_G(\hbar\omega) + (1-\eta)\,\alpha_L(\hbar\omega), \tag{3.39}$$

where the Gaussian broadening is described by,

$$\alpha_G = \frac{A\sqrt{R^*}}{\hbar\omega}\left(2R^*\sum_{n=1}^{N}\frac{e^{-\left(\hbar\omega-E_g+\frac{R^*}{n^2}\right)^2/2\tau_n^2}}{n^3\sqrt{2\pi}\tau_n} + \frac{1+\operatorname{erf}\left(\frac{\hbar\omega-E_g}{\sqrt{2}\tau_c}\right)}{2} + \frac{\tau_c e^{-\left(\hbar\omega-E_g-R^*\right)^2/2\tau_c^2}}{58\sqrt{2\pi}} + \right.$$

$$\left. \frac{\hbar\omega-E_g-R^*}{116R^*}\left(1+\operatorname{erf}\left(\frac{\hbar\omega-E_g-R^*}{\sqrt{2}\tau_c}\right)\right)\right), \tag{3.40}$$

and the Lorentzian broadening is,

$$\alpha_L = \frac{A\sqrt{R^*}}{\hbar\omega}\left(\frac{2R^*}{\pi}\sum_{n=1}^{N}\frac{\Gamma_n/n^3}{(\hbar\omega-E_g+\frac{R^*}{n^2})^2+\Gamma_n^2} + \left[0.5+\arctan\left(\frac{\hbar\omega-E_g}{\Gamma_c}\right)/\pi\right] + \right.$$

$$\arctan\left(\frac{\hbar\omega-E_g-R^*}{\Gamma_c}\right)\frac{(\hbar\omega-E_g-R^*)}{58\pi R^*} - \arctan\left(\frac{\hbar\omega-E_m}{\Gamma_c}\right)\left(\frac{\hbar\omega-E_m}{58\pi R^*}\right) + $$

$$\left. \frac{E_m-E_g-R^*}{116R^*} - \frac{\Gamma_c}{116\pi R^*}\ln\left[\frac{(E-E_g-R^*)^2+\Gamma_c^2}{(\hbar\omega-E_m)^2+\Gamma_c^2}\right]\right). \tag{3.41}$$

Here, η in eq. (3.39) measures the weight of each contribution. τ and Γ in eqs. (3.40) and (3.41), respectively, have units of energy and represent the broadening of the Gaussian and Lorentzian. The subscript n and c has been added to denote the discrete and continuum contributions, respectively, for each profile. For instance, in the case of eq. (3.40), τ_1 defines the broadening of the first discrete peak, while τ_c does it for the continuum part. Higher order broadening discrete peaks follow the Toyozawa relation [154, 170]:

$$\tau_n = \tau_c - \frac{\tau_c - \tau_1}{n^2}. \tag{3.42}$$

Likewise, the broadening Γ follow the same relations of eq. (3.42). In addition, the two broadenings, Γ and τ, are correlated (see eq. (3.43)) by sharing the same Full Width Half Maximum (FWHM) according to the procedure of Soufiani et al. [155]. This allow an improvement of the fitting region and the reduction of one free parameter. A key feature to

perform meaningful fits.

$$2\Gamma_n = 2\sqrt{2\ln(2)}\tau_n. \tag{3.43}$$

3.4 Uncertainty Principle in the EBF model

The pseudo-Voigt profile, performed by Soufiani et al., described in the previous section is applied to improve our EBF model. Here, we describe the absorption to be composed of an EBF profile, accounting for the thermal contribution, and a Lorentzian profile, for the uncertainty principle contribution. This reads as:

$$\alpha(\hbar\omega) = \eta\,\alpha_{EBF}(\hbar\omega) + (1-\eta)\alpha_L(\hbar\omega), \tag{3.44}$$

with

$$\alpha_{EBF} = \frac{A_1\sqrt{R^*}}{\hbar\omega}\left(2R^*\sum_{n=1}^{N}\frac{1}{n^3\sigma_n}\frac{e^{-\left(\hbar\omega-E_g+\frac{R^*}{n^2}\right)/\sigma_n}}{\left(1+e^{-\left(\hbar\omega-E_g+\frac{R^*}{n^2}\right)/\sigma_n}\right)^2}+ \right.$$
$$\left. A_2\left(\frac{1}{1+e^{(E_g-\hbar\omega)/\sigma_c}}+\frac{1}{e^{2\pi\sqrt{\frac{R^*}{\hbar\omega-E_g}}}-1}\right)\right), \tag{3.45}$$

whereas α_L is described by eq. (3.41).

Equation (3.45) is written accounting for different broadenings in the discrete and continuous parts. Note that, discrete peaks follow the relation of eq. (3.42). And, the correlation between the Lorentzian and EBF FWHM is $2\Gamma_n = 4\sigma_n\mathrm{arccosh}(\sqrt{2})$.

It is remarkable to say that during the implementation of eq. (3.45), different coefficients, A_1 and A_2, had been used for the discrete and continuous, respectively. This difference can be understood from the matrix element which can be modeled as Lorentz oscillator for regions above the bandgap [69, 37]. In addition, differences between eqs. (3.45) and (3.38), such as the extra $\sqrt{R^*}$ alongside A_1, are related to our inclination of constructing an expression similar to the ones used by Soufiani et al. [155]. We highlight that eq. (3.45) have six parameters only. Those are, $A1$, $A2$, σ_d, σ_c, E_g and E_b.

Lastly, it is remarkable that during the fitting procedure with eq. (3.44), the best fitted parameters were achieved in the regime of $\eta \approx 0.99$. Thus, indicating that only band-fluctuations effects, either thermal or structural, modeled with the EBF model of eq. (3.45), contribute to shape the absorption for the materials analyzed in this work. Nonetheless, this

behavior may not be generalized for other materials, and the full expression of eq. (3.44) should be used before attempting to neglect Lorentzian broadening.

3.5   Optical Absorption Results

In this section, I describe first the absorption curves and the fitting procedure of the EBF and the pseudo-Voigt for an specific data set at room temperature. Then I proceed to apply the developed EBF to the temperature dependent absorption curves and retrieve best fitted parameters of bandgap, FWHM and first exciton binding energy.

Eq. (3.45) is applied to describe the excitonic absorption of GaAs, and tri-halide perovskites, MAPbBr$_3$, MAPbI$_3$ and MAPbI$_{3-x}$Cl$_x$. This analysis starts by presenting the comparison of the EBF model with the pseudo-Voigt one. Fits of eq. 3.44 and eq. 3.39 are depicted in figures 3.1-a, b, c and d for absorption curves at room temperature of the aforementioned materials. The experimental data were extracted from Sturge [158] for GaAs, Soufiani et al. [154] for MAPbBr$_3$ and MAPbI$_3$, and D'Innocenzo et al. [26] for MAPbI$_{3-x}$Cl$_x$. In the case of GaAs, the data were obtained by measuring the transmittance [158]. For MAPbBr$_3$ and MAPbI$_3$, the data were obtained by measurements of the transmitted light with an spectrophotometer at room temperature, while a method using free space optics and an spectrometer was used for the measurements at several temperatures (the latter controlled by a cryostat) [154]. For MAPbI$_{3-x}$Cl$_x$ the measurements were carried on by a spectrophotometer, and a flow static exchange gas cryostat were used for controlling sample temperature [26]. For all cases, relations between the transmittance and reflectance with the absorption coefficient were employed. Following figures 3.1-a, b, c and d, we see that the EBF is presented in red lines, while Soufiani's model is plotted as black. In addition, the discrete and continuum contributions of the EBF model are presented separately in order to appreciate the shape of each part of the equation.

In these cases, the EBF fits have converged to η equals to 0.99, meaning that fluctuations distribution modeling the thermal contribution is enough for modeling the absorption data of GaAs and tri-halide perovskites. For this value of η, the Soufiani's model shows a good accuracy for the fits despite having small differences for the binding energy, bandgap and FWHM when compared to EBF. We remark that in the original paper of Soufiani [154], values of η vary depending on the sample temperature. They become small when temperature raises, making the Lorentzian factor $1 - \eta$ to grow. Nevertheless, our eq. 3.44 with $\eta = 0.99$ show good results for the bandgap and exciton peaks when compared with other experimental results as it will be shown in the next chapter. Even more, modeling of the temperature
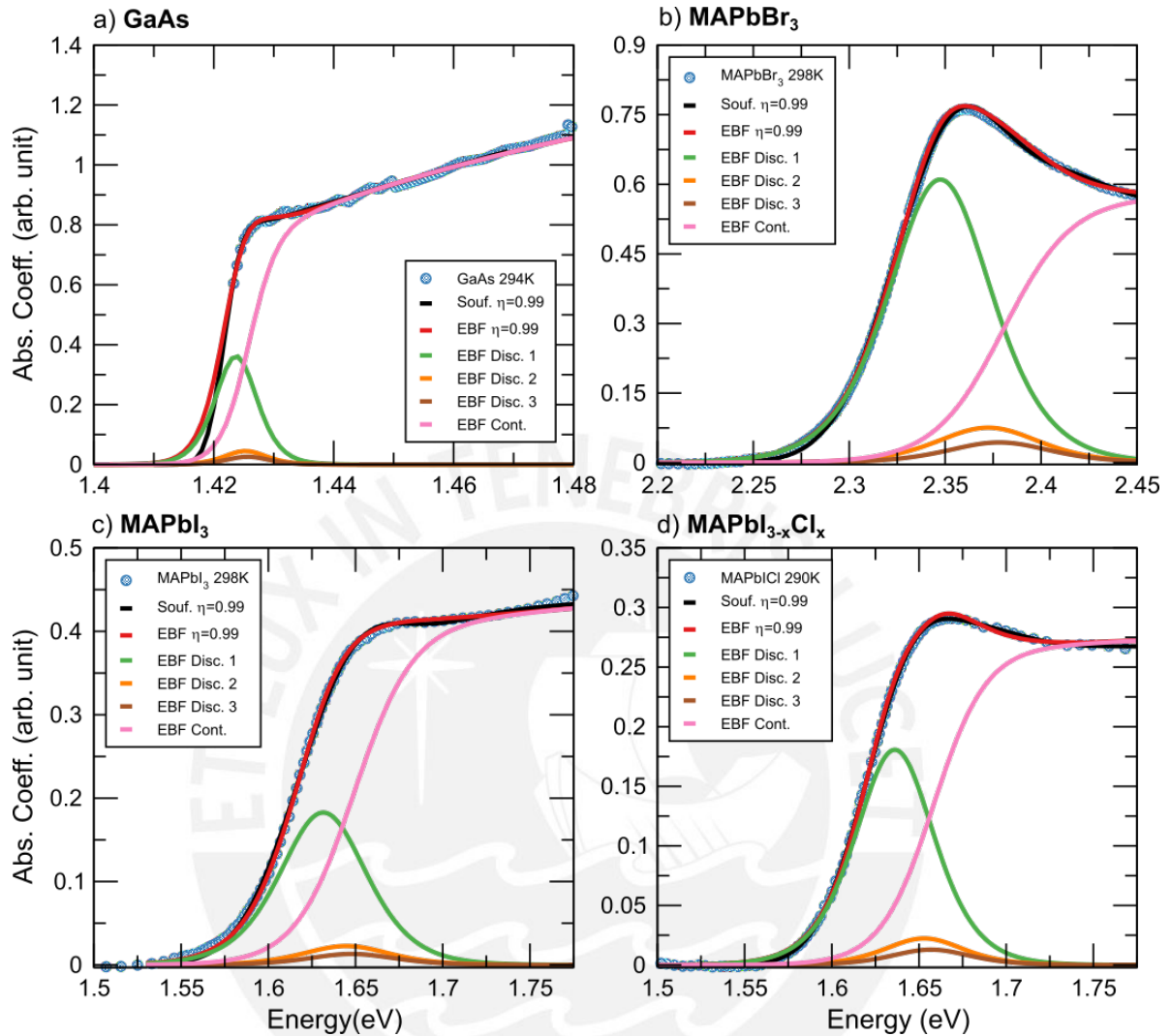
Fig. 3.1 Different contributions to the absorption of the discrete and continuum (pink lines) parts of the equation 3.44 for GaAs and the family of tri-halide perovskites. According to the fits, η has a value of 0.99. Thus, indicating that the only contribution of the curves arises from the thermal contribution of the EBF model. In addition, the fit of Soufiani et. al. model for $\eta = 0.99$ is presented in black lines for comparison purposes. In the legend, Disc. 1 accounts for the first exciton, Disc. 2 for the second exciton, and Disc. 3 to the sum from the third peak to infinity.

dependent EBF parameters, obtained from these fits, give us important physical conclusions on the material properties.

Temperature dependent absorption of direct GaAs fitted with the EBF model is shown in figure 3.2-a, b in linear and semilogarithmic scale with an excellent agreement with the collected data, extracted from [204, 158], for temperatures of 21K, 90K, 186K and 294K. Figures 3.2-a, b shows the full absorption in solid lines, while the description of discrete and

continuous contributions are plotted in dashed lines, for each sample temperature. Table 3.1 summarize the best fitted parameters.

The absorption at different temperatures for the family of tri-halide perovskites, $MAPbBr_3$, $MAPbI_3$ and $MAPbI_{3-x}Cl_x$ is presented as symbols in figures 3.2-c and d, 3.3-a and b, and 3.3-c and d, respectively. The sets of data were extracted from references [154] and [26] for ranges of temperature of 7K to 298K. Here, the fitted absorption is presented in solid line, while separated contributions are depicted in dashed lines. Our fits were performed in linear scale, for this reason, the absorption fits in semi-logarithmic scale show slight deviations as seen in figures 3.2d, 3.3 b and d. Nevertheless, the fits show that the three types of tri-halide pervoskites are shaped accurately by the EBF model. The best fitted parameters are written in tables 3.2, 3.3 and 3.4 for $MAPbBr_3$, $MAPbI_3$ and $MAPbI_{3-x}Cl_x$, respectively.

In the case of perovskites, two main features are observed, the well known phase transition from orthorombic to tetragonal phase marked at 140K with the notorious kink of the bandgap. And, the raise of the bandgap with temperature. This differ with the declining behavior observed in GaAs. Bandgap evolve with the sample temperature differently for both systems due to the thermal expansion and electron-phonon interaction. This will be addressed in detail at the beginning of chapter 4.

The comparison of the values shown in tables 3.1, 3.2, 3.3 and 3.4 with other studies is performed in chapter 4. There, an analysis of the thermal evolution in terms of the electron-phonon interactions is also presented for the bandgap, broadening (quantified by the FWHM) and binding energy.
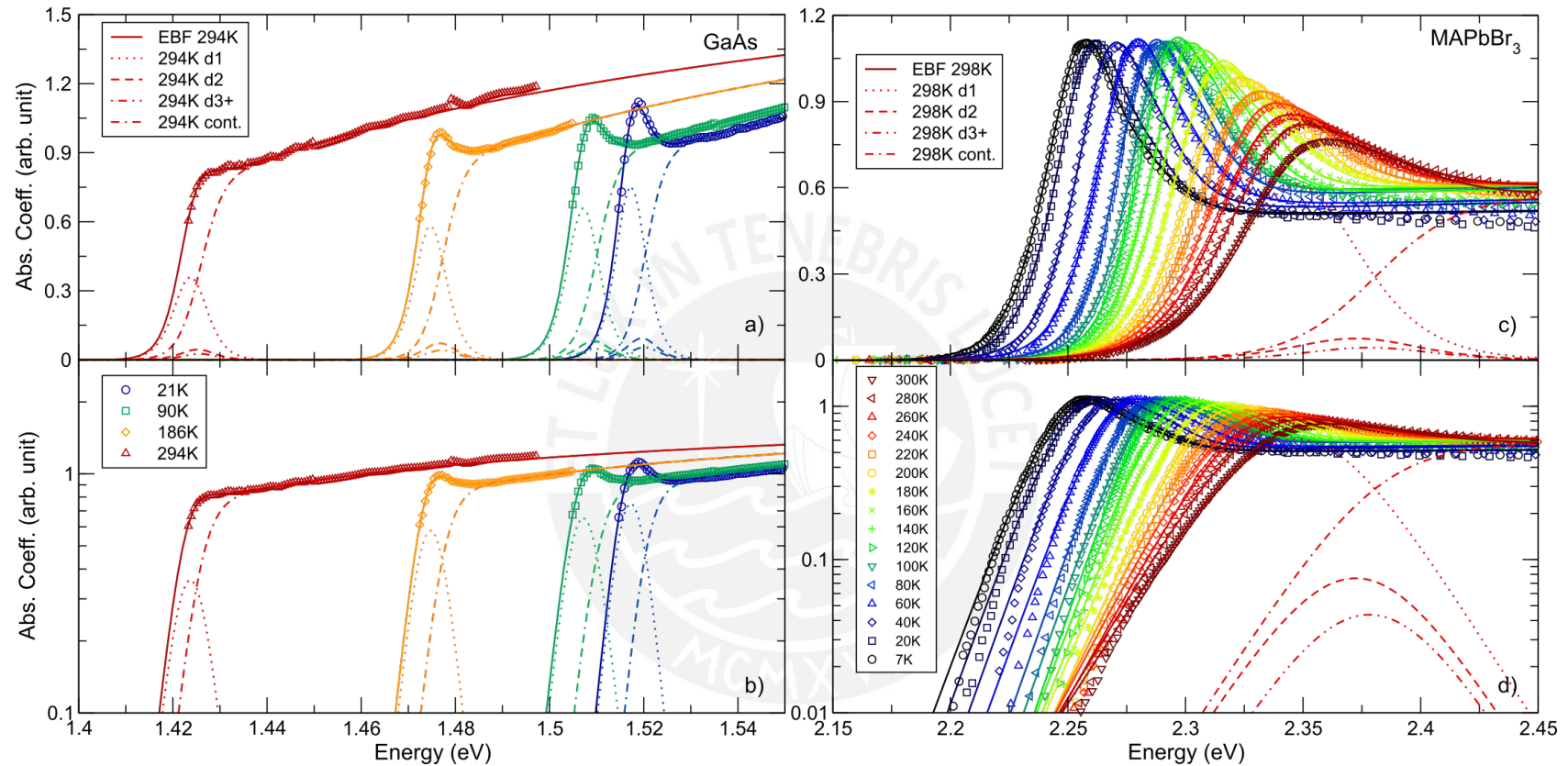
Fig. 3.2 Absorption coefficient of GaAs, extracted from Sturge [158], fitted with the EBF model for several temperatures in linear (a) and semilogarithmic (b) scale. Here the contributions of the discrete peaks and the continuum are plotted in dashed lines in figures (a) and (b). Absorption coefficient of MAPbBr$_3$, extracted from Soufiani [154], fitted with the EBF model for several temperatures in linear (c) and semilogarithmic scale (d). In figure (c), the contributions of the excitonic peaks and the continuum is shown in dashed lines for T=298K.
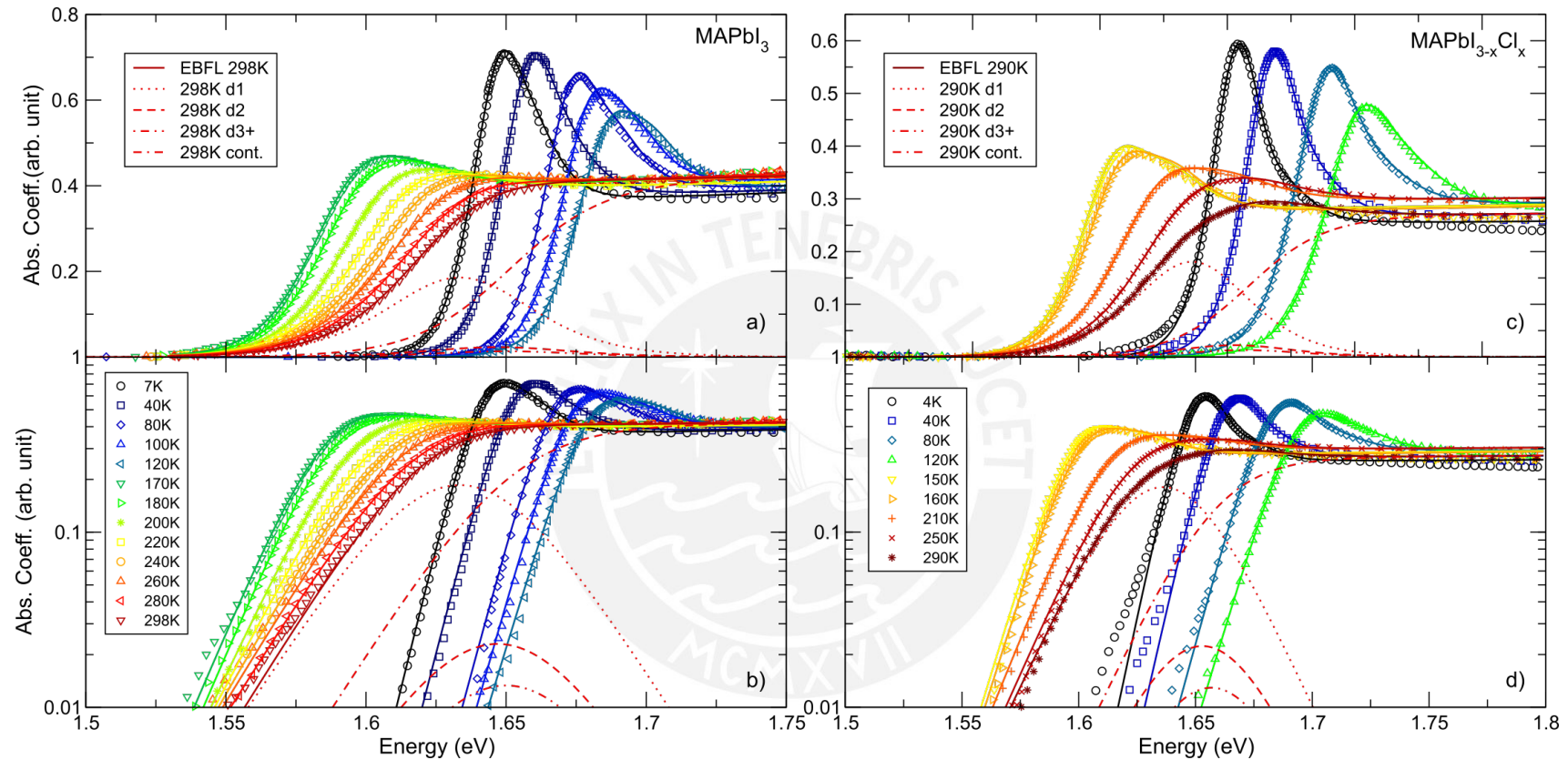
Fig. 3.3 Absorption coefficient of MAPbI$_3$, extracted from Soufiani [154], fitted with the EBF model for several temperatures in linear (a) and semilogarithmic (b) scale. Figure (a) shows the contributions of the discrete peaks and the continuum, in dashed lines, for T=298K. Absorption coefficient of MAPbI$_{3-x}$Cl$_x$, extracted from D'Innocenzo [26], fitted with the EBF model for several temperatures in linear (c) and semilogarithmic scale (d). In figure (c), the contributions of the excitonic peaks and the continuum is shown in dashed lines for T=290K.

Table 3.1 GaAs parameters of the EBF model for temperatures in the range of 21-294K.

T(K)	A1	A2	σ_d (meV)	σ_c (meV)	E_g (meV)	E_b (meV)
21	27.8 (13)	0.91 (3)	2.11 (4)	2.34 (10)	1520 (0)	3.12(13)
90	28.94 (68)	0.88 (2)	2.31 (5)	2.43 (12)	1510 (0)	2.93 (6)
186	29.9 (14)	0.86 (3)	2.25 (6)	2.42 (15)	1477 (21)	2.56 (12)
294	26 (12)	0.98 (46)	2.4 (10)	2.2 (16)	1425 (2)	2.08 (11)

Table 3.2 MAPbBr$_3$ parameters of the EBF model for temperatures in the range of 7-298K

T(K)	A1	A2	σ_d (meV)	σ_c (meV)	E_g (meV)	E_b (meV)
7	9.58 (18)	0.72 (1)	10.45 (4)	7.90 (15)	2285(1)	29.70(50)
20	10.4 (3)	0.68 (1)	10.13 (7)	7.37 (25)	2287 (1)	27.41 (76)
40	12.17 (52)	0.65 (2)	10.01 (9)	6.96 (34)	2292 (1)	24.01 (93)
60	11.58 (31)	0.68 (1)	10.24 (6)	7.27 (22)	2303 (1)	25.64 (64)
80	12.84 (35)	0.69 (1)	9.83 (6)	6.57 (21)	2307 (1)	23.13 (59)
100	12.16 (25)	0.73 (1)	9.84 (6)	6.55 (16)	2314 (1)	24.07 (47)
120	13.51 (44)	0.69 (1)	9.60 (9)	5.91 (28)	2315 (1)	22.20 (68)
140	11.50 (31)	0.74 (1)	10.56 (8)	6.44 (26)	2326 (1)	26.46 (68)
160	11.09 (21)	0.77 (1)	11.00 (6)	6.83 (19)	2332 (1)	27.40 (51)
180	10.99 (21)	0.78 (1)	12.01 (7)	7.69 (21)	2340 (1)	28.28 (53)
200	11.13 (28)	0.81 (1)	12.59 (1)	7.99 (29)	2345 (1)	27.46 (69)
220	10.59 (23)	0.78 (1)	13.82 (11)	9.02 (28)	2353 (1)	28.80 (65)
240	10.34 (30)	0.83 (1)	14.84 (14)	10.13 (34)	2359 (1)	29.17 (88)
260	9.75 (20)	0.86 (1)	15.50 (12)	10.57 (26)	2365 (1)	30.16 (69)
280	8.84 (23)	0.91 (1)	16.86 (13)	12.44 (27)	2374 (1)	33.02 (93)
298	8.53 (11)	0.89 (1)	18.07 (4)	13.60 (12)	2381 (1)	33.28 (47)

Table 3.3 MAPbI$_3$ parameters of the EBF model for temperatures in the range of 7-298K

T(K)	A1	A2	σ_d (meV)	σ_c (meV)	E_g (meV)	E_b (meV)
7	7.39 (21)	0.68 (1)	6.62 (4)	4.93 (13)	1662 (1)	15.17 (38)
40	6.62 (29)	0.75 (2)	6.92 (5)	5.68 (18)	1675 (1)	16.85 (68)
80	6.25 (15)	0.81 (1)	7.23 (6)	4.83 (16)	1692 (1)	17.57 (42)
100	6.68 (17)	0.82 (1)	7.61 (7)	5.08 (17)	1696 (1)	16.32 (44)
120	6.47 (18)	0.83 (1)	8.11 (8)	5.28 (20)	1703 (1)	16.08 (46)
170	4.97 (14)	0.99 (2)	11.49 (8)	9.32 (19)	1613 (1)	17.86 (55)
180	5.37 (12)	0.96 (1)	11.52 (7)	9.27 (20)	1614 (1)	15.96 (37)
200	4.65 (12)	1.03 (2)	12.68 (8)	10.47 (20)	1624 (1)	18.34 (54)
220	4.84 (20)	1.01 (2)	14.04 (8)	12.56 (23)	1631 (1)	17.89 (80)
240	4.53 (37)	1.08 (5)	15.24 (9)	14.62 (24)	1639 (2)	19.3 (17)
260	4.61 (73)	1.08 (9)	16.19 (20)	15.47 (51)	1643 (5)	18.8 (32)
280	5.23 (81)	1.04 (10)	16.76 (12)	16.33 (61)	1644 (4)	15.5 (24)
298	4.24 (74)	1.22 (10)	16.70 (24)	15.45 (49)	1649 (3)	17.7 (15)

Table 3.4 MAPbI$_x$Cl$_{3-x}$ parameters of the EBF model for temperatures in the range of 4-290K

T(K)	A1	A2	σ_d (meV)	σ_c (meV)	E_g (meV)	E_b (meV)
4	3.58 (11)	0.79(1)	6.85 (6)	5.24 (27)	1677 (1)	23.54 (67)
40	4.03 (15)	0.77(2)	7.32 (6)	6.10 (25)	1690 (1)	22.22 (76)
80	3.89 (7)	0.83(1)	8.76 (4)	6.98 (16)	1714 (1)	24.61 (44)
120	4.05 (7)	0.82(1)	9.63 (4)	7.21 (11)	1724 (1)	22.74 (39)
150	3.51 (8)	0.91(1)	9.76 (9)	6.18 (23)	1628 (1)	21.47 (56)
160	3.57 (9)	0.89(1)	10.02 (9)	6.29 (23)	1630 (1)	20.95 (55)
210	3.19 (6)	1.02(1)	12.87 (9)	9.22 (20)	1648 (1)	23.82 (58)
250	3.21 (7)	1.04(1)	14.22 (13)	10.51 (28)	1656 (1)	22.36 (62)
290	2.67 (6)	1.13(1)	15.17 (19)	10.96 (33)	1658 (1)	22.40 (68)

Chapter 4

Thermal Analysis of Optical Parameters

The present chapter starts with an examination of the thermal evolution of the parameters derived from the Elliott-BF model. Specifically, in section 4.1, the thermal evolution of the bandgap can be described in terms of the models of Varshni [179], Passler [121], Viña [182], or the two oscillator one [50, 97]. These models predominantly take into account the electron-phonon contribution. However, for materials like Perovskites [191, 42, 203], the thermal expansion term cannot be neglected when describing the bandgap evolution. A model describing both contributions was first developed by Cardona et al. [17]. In this chapter, we perform an analysis based on the Cardona and Varshni's models for GaAs and tri-halide perovskites. As a result, the LO phonon energy of the solid is calculated. This energy give us information related to the phonon density of states and will be important later in this chapter for calculating thermal properties of the system.

To analyze the FWHM, we employ the model proposed by Toyozawa, Segall, and Mahan [171, 139], which accounts for the coupling of acoustic and optical phonons with electrons. In the here studied semiconductors, the electron-phonon coupling dominates, and as a result, the broadening (FWHM) is proportional predominantly to the LO phonon contribution. As a consequence, the boson occupation number determines the line shape, and the LO phonon energies for tri-halide perovskites are retrieved from this. The thermal evolution of the bandgap and FWHM discussed in sections 4.1 and 4.2 are mandatory for deriving the thermal properties presented in the final part of this chapter.

Section 4.3 describes the thermal evolution of the exciton binding of the GaAs and tri-halide perovskites. The retrieved binding energies are then compared with the literature. Surprisingly, we found a large difference among the different experimental set ups. Nevertheless, this variability can be understood if the polar nature of perovskite systems is considered. Apparently, the variability of the exciton-polaron binding energy is the reason for the large discrepancy in experimental results. For this reason, we explore the picture in which the

exciton interacts with phonons through the electron-phonon interaction in section 4.4. This theory was studied previously by Haken, Toyozawa [171], Pollmann and Buttner [125], and Kane [73]. Here we focus on the Pollman and Kane procedure for finding the ground state binding energy of this exciton dressed by the cloud of LO phonons. We explore this model in section 4.4.1, and the resulting self-consistent equations require initial values for the effective masses of electron and hole, the LO phonon energies, the static and the high frequency dielectric functions [73]. The result of this procedure predicts an exciton binding energy that depends heavily on the phonon branch. What is more, the retrieved binding energy of the LO phonon energy calculated with the thermal evolution of the bandgap and FWHM agrees with the binding energy retrieved using the EBF model. Remarkably, this suggests that the polaron contribution of a solid can be well described by the band-fluctuations model.

If we invert the procedure of the Kane model, i.e., if we fix the LO phonon energy, we can calculate a surface map of the binding energy that only depends on effective band masses of the electron and hole. The results on this procedure shows a good accuracy of the predicted electron and hole band masses for the tri-halide perovskites. Again, the agreement with the here presented results is an indicator of the goodness of the EBF model for predicting structural properties.

Finally, we use the retrieved LO phonon energies obtained from the bandgap and FWHM sections to compute various thermodynamic quantities for the GaAs and perovskite systems. Specifically, we evaluate the Specific Heat, Helmholtz Energy, Internal Energy, and Entropy. To assess the accuracy of our specific heat predictions, we compare these quantities with experimental reports based on calorimetric techniques. Impressively, the optical analysis appears to provide a reliable method for predicting specific heat values in the aforementioned systems. This is consistent with prior work by Ventura et al. [181], which demonstrated the efficacy of optical models for determining thermal properties of solids. Thus, our findings provide further evidence of the utility of optical analysis for investigating thermal properties in materials science.

4.1 Thermal Evolution of the Bandgap

The evolution of the bandgap with temperature obtained after the fitting with the EBF model to GaAs and tri-halide perovskites absorption data are shown in figure 4.1. Here, we see that the results for GaAs are in close agreement with the values of Sturge [158], obtained by fitting the continuum part of the Elliot model at the band edge. In addition, other authors found similar results by measuring the reflectance of high purity and doped GaAs samples [141, 11]. Likewise, The here obtained results for $MAPbBr_3$ and $MAPbI_3$ are comparable

Table 4.1 Bandgap fit by using the model of Cardona with both contributions, eq. (4.6), for GaAs and tri-halide perovskites at different temperatures. Here, the error bars are not shown due to their large values. However, it is remarkable that the LO phonon energy retrieved by this model is in agreement with the one calculated from the FWHM fit shown at table 4.3. The fit of the set of data for Sturge [158] and Soufiani [154] are labeled as the superscripts (st) and (^{s}), respectively.

Material	T (K)	E_0 (meV)	A_{te} (meV/K)	A_{ep} (meV)	$\hbar\omega_{LO}$ (meV)
GaAs	21-294	1617	-0.12	-94.78	35.74
		1583st	-0.11^{st}	-71.19^{st}	32.71^{st}
MAPbBr$_3$	7-140	2283	0.31	-1.85	17.97
		2328^{s}	0.45^{s}	-33.94^{s}	19.03^{s}
	160-298	2279	0.39	-5.81	17.29
		2356^{s}	0.21^{s}	-193.41^{s}	16.85^{s}
MAPbI$_3$	7-120	1679	0.42	-20.4	18.83
		1674^{s}	0.33^{s}	-1.54^{s}	16.44^{s}
	170-298	1711	9.76	-698.95	12.31
		1714^{s}	13.88^{s}	-805.9^{s}	9.95^{s}
MAPbI$_x$Cl$_{3-x}$	4-120	1691	0.47	-16.29	19.56
	150-290	1749	3.27	-408	20.72
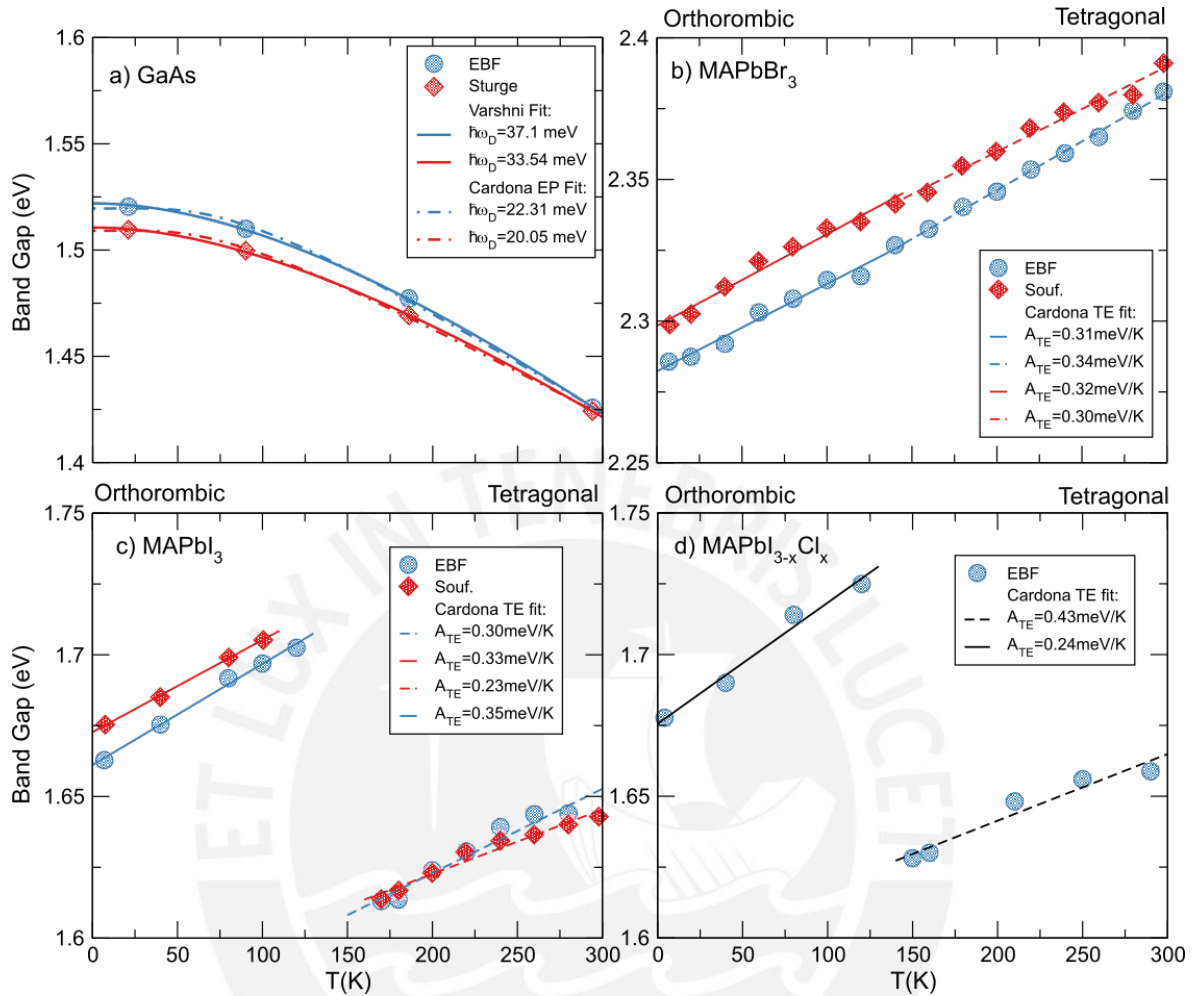
Fig. 4.1 Bandgap energies, retrieved by the EBF model, for GaAs (a), MAPbBr$_3$ (b), MAPbI$_3$ (c) and MAPbI$_{3-x}$Cl$_x$ (d) presented as blue marks. Figure (a) present the data collected from Sturge [158] in red marks for comparison purposes. Here, the continuum and dashed lines show the fits using the Varshni model, eq. (4.7), and Cardona's model, eq. (4.6 with $A_{TE} = 0$), respectively. Likewise, Figures (b) and (c) present the data collected from Soufiani et al. [154], in red marks, for MAPbBr$_3$ and MAPbI$_3$ for comparison purposes. The figures (b), (c) and (d) show a set of continuum and dashed lines which represent the fit of Cardona's model, eq. (4.6) with $A_{EP} = 0$, for the different perovskite phases, the orthorombic and tetragonal, respectively.

with the values found at Soufiani et al [154], obtained by fitting the pseudo Voigt of the Gaussian and the Lorentzian smearing. Additionally, these values are in agreement with other literature reports [49, 54, 132, 102], confirming the good estimation of our results. Lastly, for MAPbI$_{3-x}$Cl$_x$, the results differs by 81 meV, at low temperatures $(2-4K)$, and by an amount of 46 meV, at high temperatures $(190-200K)$, with the report of Galkowski et al. [49], using the magneto absorption technique. Nevertheless, this difference can be attributed

to the sample composition due to the different methods used to synthesize $MAPbI_{3-x}Cl_x$ in D'Innocenzo et al. [26], and Galkowski et al. [49]. In particular, in the report from which the data of this sample was taken, the authors do not specify the stoichiometry.

For the case of GaAs, the bandgap is reduced when temperature is increased, while in the case of tri-halide perovskites, the bandgap increments. The observed difference can be explained by the contributors of the bandgap evolution with the sample temperature. These are the thermal expansion (TE) and the electron-phonon (EP) interaction [42, 191]. For this reason, the evolution of the bandgap can be modeled as [17]:

$$\Delta E_g(T) = [\Delta E_g(T)]_{TE} + [\Delta E_g(T)]_{EP}. \tag{4.1}$$

The first term in the right hand of eq. (4.1) is the effect of the bandgap caused by the contraction/expansion of the lattice as a response of the band-structure when an external hydrostatic pressure is applied [81, 53]. Whilst the second term is composed by the Debye-Waller and Fan terms. The former accounts for the interaction of an electron with two phonons, whilst the latter describes the second order interaction of electron-phonon known as self energy [53, 17, 50].

The thermal expansion contribution depends linearly with temperature [17], i.e.,

$$\Delta E_g(T) \mid_{TE} = -\alpha_v B_0 \frac{dE_g}{dP} T, \tag{4.2}$$

where α_v is the volumetric expansion coefficient, B_0 is the bulk modulus, and dE_g/dP is the pressure behavior of the gap [42, 97]. The coefficients α_v and B_0 are positive for semiconductors such as Si [114], Ge [110], GaAs [111] and halide perovskite families [137, 127, 161, 186, 160, 130, 205, 188]. Thus, implying that the sign of eq. (4.2) depends exclusively on the pressure term, which is positive for semiconductors such as GaAs [147] or Ge [118, 81], and negative in cases like Si [81] and tri-halide perovskites, $MAPbI_3$ [41, 42], $MAPbBr_3$ [77], $MAPbCl_3$ [186].

On the other hand, the renormalized bandgap due to the electron-phonon term is derived in reports of Gopalan, Cardona, Lautenschlager and others [53, 81, 17]. They deduce an expression where all the phonons modes of the jth, wave vector q and energy ω_{jq} contribute to the shift and broadening of the electron state, E_{nk}, with wave vector k at the nth electronic band [42], i.e.,

$$\Delta E_{nk}(T) = \sum_{jq} \frac{\partial E_{nk}}{\partial n_{jq}} \left(n_{jq}(T) + \frac{1}{2} \right). \tag{4.3}$$

Here n_{jq} is the Bose-Einstein distribution, $n_{jq} = (e^{\beta \hbar \omega_{jq}} - 1)^{-1}$ with $\beta = (k_\beta T)^{-1}$, and the coefficients $\partial E_{nk}/\partial n_{jq}$ are the electron-phonon matrix elements. These elements can

be taken as effective electron-phonon coefficients, A_i, at an average frequency ω_i which is deduced from the observation of the phonon DOS [42, 50, 8]. The resulting contribution of the EP interaction, known as Einstein oscillator, for the renormalization of the bandgap is:

$$\Delta E_g(T)\,|_{EP} = \sum_i A_i \left(n(\omega_i, T) + \frac{1}{2} \right).$$ (4.4)

Note that the A_i coefficients are determined by the fitting of the experimental data. However, this sum can collapse into a single term for cases such as GaAs and tri-halide perovskites due to the non presence of separated behaviors in the DOS[42], i.e.,

$$\Delta E_g(T)\,|_{EP} = \frac{A_1}{2} \left(\frac{2}{e^{\hbar\omega/k_\beta T} - 1} + 1 \right).$$ (4.5)

Nevertheless, there are families of semiconductors such as the cuprous halides where two oscillators are required for the acoustic and optical branches [50, 144]. By replacing eqs. (4.2) and (4.5) in eq. (4.1), we can write the full expression for the description of the bandgap proposed by Cardona and co-workers,

$$\Delta E_g(T) = E_{g_0} + A_{TE} T + A_{EP} \left(\frac{2}{e^{\hbar\omega/k_\beta T} - 1} + 1 \right).$$ (4.6)

Here, E_{g_0} is the unrenormalized bandgap, and the coefficients are $A_{TE} = -\alpha_v B_0 \frac{dE_g}{dP}$ and $A_{EP} = A_1/2$. ω is the average optical phonon frequency, ω_{LO}, which is also called Debye frequency, ω_D, due to its theoretical closeness [121].

In previous reports, we have found that the EP contribution in GaAs are around 79% [91], 67% [62], and 56% [10]. The reason why EP is larger than the TE for this material may be due to the small volume deformation potential as it has been shown for Si [17]. However, this behavior is not repeated for the family of tri-halide perovskites in which the EP interaction contributes up to 40% [42, 191, 203].

Eq. (4.6) was used to fit the bandgap evolution with temperature of GaAs, MAPbBr$_3$, MAPbI$_3$ and MAPbI$_{3-x}$Cl$_x$. During the implementation of the fit, our analysis encounter problems regarding the uncertainties of the parameters. For instance, the linear behavior of the perovskites overshadow the electron phonon term producing large error bars for the A_{EP} term. Likewise, for GaAs, the detriment of the exponential opaque the linear behavior of the thermal expansion. Notwithstanding, the best fitted parameters using eq. (4.6) are presented in table 4.1, for comparison purposes only. There, we can see a good estimation of the LO phonon energy comparable to reports found in [89, 19] and [199, 85, 51] for GaAs and the tri-halide perovskites, respectively.

Table 4.2 Parameters of the bandgap evolution versus temperature of GaAs by using the Varshni model, eq. (4.7), and the Cardona's model, eq. (4.6) with $A_{TE} = 0$. In the case of tri-halide perovskites, only the linear thermal expansion contributes to eq. (4.6). Here, the fits of the set of data for Sturge [158] and Soufiani [154] are labeled as the superscripts (st) and (^{s}), respectively.

Material	T (K)	Model			
GaAs	21-294	Varshni et al. [179]			
		E_0 (meV)	a_B (meV/K)	$\hbar\omega_D$ (meV)	
		1522 (1.09)	0.80 (0.14)	37.08 (11.08)	
		1511 (0.73)st	0.68 (0.08)st	33.54 (7.11)st	
GaAs	21-294	Cardona et al. [204]			
		E_{g_0} (meV)	A_{te} (meV/K)	A_{ep} (meV)	$\hbar\omega_{LO}$ (meV)
		1585 (15.33)	0	-65.9 (16.5)	22.31 (3.79)
		1560 (9.19)st	0	-51.02 (10.03)st	20.05 (2.79)st
MAPbBr$_3$	7-140	2282 (1.52)	0.31 (0.02)	0	-
		2298 (1.68)^s	0.32 (0.02)^s	0	-
	160-298	2277 (1.94)	0.34 (0.008)	0	-
		2299 (4.39)^s	0.30 (0.02)^s	0	-
MAPbI$_3$	7-120	1661 (1.33)	0.35 (0.02)	0	-
		1673 (0.54)^s	0.33 (0.008)^s	0	-
	170-298	1564 (5.91)	0.30 (0.03)	0	-
		1577 (4.08)^s	0.23 (0.02)^s	0	-
MAPbI$_x$Cl$_{3-x}$	4-120	1676 (3.29)	0.43 (0.04)	0	-
	150-290	1594 (7.39)	0.24 (0.03)	0	-

Despite the previous procedure, we have used a thermal expansion independent version of the Cardona's model [17], i.e., eq. (4.6) with $A_{TE} = 0$. This is then applied to fit the bandgap evolution of GaAs. Likewise, an independent electron-phonon version of Cardona's model, i.e. eq. (4.6) with $A_{EP} = 0$, is used for the case of tri-halide perovskites. These procedures are based on the behavior of the experimental data who obeys separated trends. In addition, this approach is reinforced by previous studies on these materials [154, 91]. Additionally, we have used the Varshni's model [179], that shapes the bandgap empirically, by taking the form of the e-ph interaction, only for the case of GaAs. Varshni's model reads as:

$$E_g(T) = E_0 + \frac{a_B T^2}{T + \hbar\omega_D/k_\beta}, \tag{4.7}$$

where E_0 is the bandgap at 0K, a_B is the amplitude and ω_D is the Debye frequency. The results of these analyses are collected in table 4.2, and presented in figure 4.1 as continuum and dashed blue lines. In the case of tri-halide perovskites, these lines denote the orthorombic and tetragonal phases, respectively. Whereas in the case of GaAs, they denote the difference between the Varshni and Cardona's model.

In addition, we have fitted the data of the bandgap extracted from Sturge [158], and Soufiani et al. [154]. These lines are colored as red dashed and continuum lines. They show a good agreement with the results obtained by fitting the EBF model. Remarkably, the Debye energy obtained with the Varshni's model presented in table 4.2 for GaAs is in agreement with other experimental values of 28 meV [122], 28.87 meV [89, 19], 36.1 meV [172], and 36.8 meV [131], and with theoretical calculations of phonon DOS found in Lawler et al. [82]. However, when these values are compared with the independent version of the Cardona's model, (eq. (4.6) with $A_{TE} = 0$), we appreciate a difference of about 15 meV that can be attributed to the fitting goodness.

4.2   Thermal Evolution of the FWHM

The full width half maximum represents the broadening of the measurement associated to thermal or uncertainty contributions. This is presented in figure 4.2 for the GaAs and tri-halide perovskites. In our case, the FWHM is only modeled by thermal effects that are shaped by the EBF model. This were calculated by using $4\sigma_n \mathrm{arccosh}(\sqrt{2})$ which is a consequence of the potential fluctuations of eq. (3.25). In the analysis, we found contributions associated with the discrete, σ_d, and continuum, σ_c, parts of the spectra. On the one hand, the discrete case corresponds to the broadening of the excitonic peak due to the aforementioned thermal contribution. Whereas, in the continuum case, this energy corresponds to the Urbach energy associated with the disorder induced localized states.

Figure 4.2a shows a horizontal behavior of the discrete and continuum FWHMs for GaAs. Here, at 294K, the values show large error bars due to non resolved excitonic peak observed in the absorption spectrum at this temperature. For the case of MAPbBr$_3$, figure 4.2b shows a horizontal trend for the orthorombic phase, while an increasing behavior is observed for the tetragonal phase. On the other hand, figures 4.2c and d show a raising trend of the discrete FWHM versus temperature for MAPbI$_3$ and MAPbI$_{3-x}$Cl$_x$, respectively.

The FWHM values for GaAs, at high temperatures ($200-300$K), are in agreement with previous reports [52, 126]. Likewise, for the case of MAPbBr$_3$ and MAPbI$_3$, the FWHMs are comparable to the values reported at [154, 195, 35, 25], for the whole studied temperature range of 0-300K. Lastly, the results of MAPbI$_{3-x}$Cl$_x$, at room temperature, show a difference
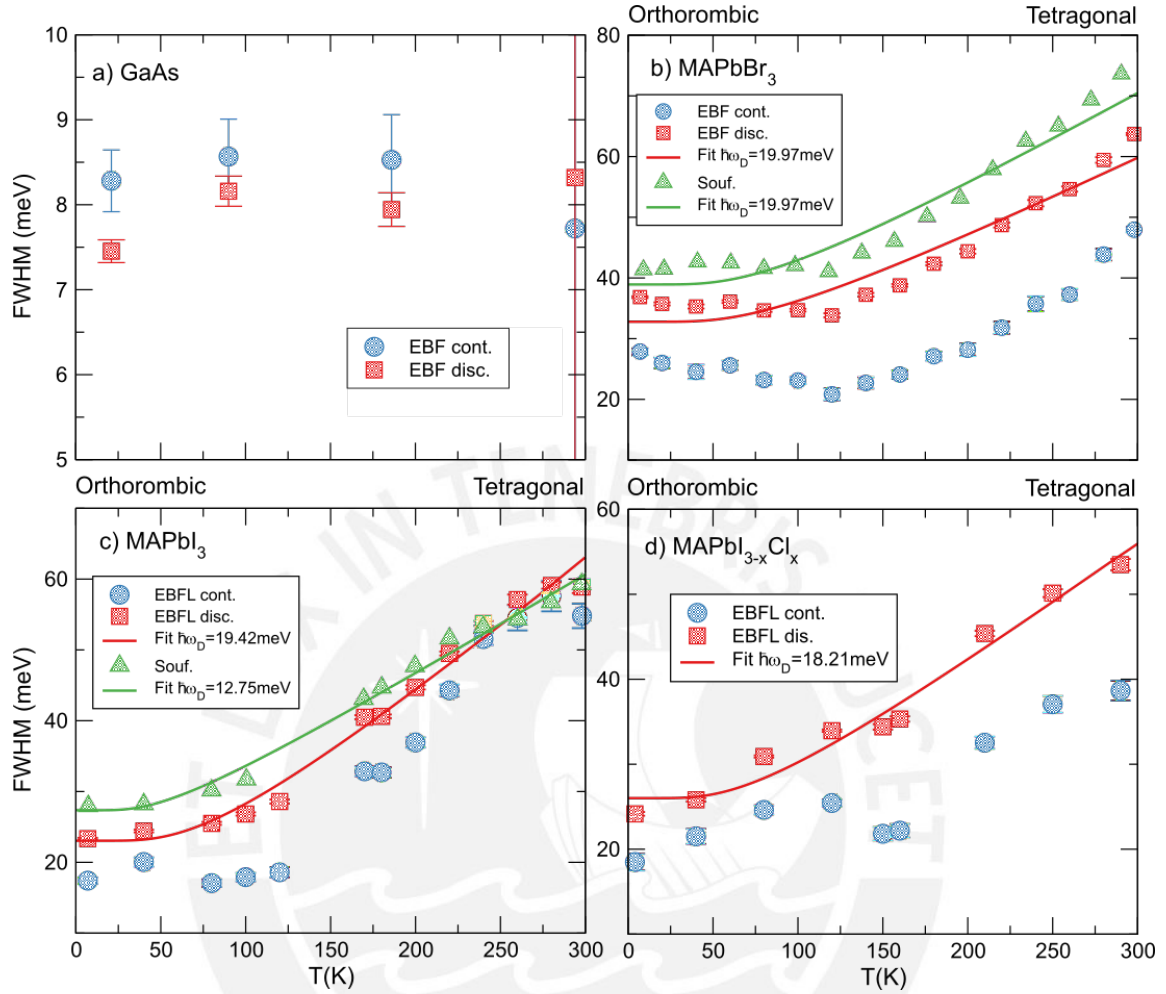
Fig. 4.2 FWHM retrieved by the EBF model for the discrete and continuum contributions marked as blue and red points, respectively, for GaAs (a), MAPbBr$_3$ (b), MAPbI$_3$ (c) and MAPbI$_{3-x}$Cl$_x$ (d). For comparison purposes, we have extracted the data from Soufiani [154] and plotted in green triangles in figures (b) and (c). Eq. (4.8) with $\Gamma_{AC} = 0$ is used to fit the excitonic FWHM of the discrete peak for the tri-halide perovskites in figures (b), (c) and (d). This is presented as red and green lines for the EBF and Soufiani data, respectively.

of 50 meV and 30 meV when compared with the PL reports of Wehrenfennig et al. [190], and, Wu et al. [197], respectively. It is remarkable to state that the values obtained from the FWHM evolution of the EBF model are similar to other studies of the families of tri-halide perovskites based on cesium, Cs, [191, 136] or formamidinium, FA, [195].

The thermal evolution of the discrete excitonic FWHM can be modeled in terms of the interaction of the exciton and phonons which is modeled with the electron-phonon interaction. The theory describing the evolution of the FWHM was developed initially by Toyozawa [171], Segall and Mahan [139]. They divided the contributions in the interactions between

electrons and acoustical phonons, and among electrons with optical phonons. In the former case, the FWHM is calculated from the deformation potential and piezoelectric interactions [131] which gives a linear evolution with temperature. In the latter, the interaction with LO phonons is modeled by the Frölich interaction which produces a FWHM dependent on the Bose-Einstein distribution, i.e., proportional to $(e^{\hbar\omega_{LO}/k_\beta T} - 1)^{-1}$ [131]. As a consequence, the final form of the FWHM can be written as:

$$\Gamma(T) = \Gamma_0 + \Gamma_{AC}T + \Gamma_{LO}\left(\frac{1}{e^{\hbar\omega_{LO}/k_\beta T} - 1}\right). \tag{4.8}$$

Here Γ_0 corresponds to FWHM at 0K, whilst Γ_{AC} and Γ_{LO} are the proportional constants related to acoustical and optical phonon terms. Additionally, $\hbar\omega_{LO}$ is the LO phonon energy.

For our analyzed materials, we are considering eq. (4.8) to be independent of the acoustical contribution, i.e., $\Gamma_{AC} = 0$. This decision is based on previous studies of GaAs [131] and tri-halide perovskites [195, 13]. And, in the case of perovskites this is reinforced by their their polar nature. The retrieved values of this procedure are presented in table 4.3. There, we see that for tri-halide perovskites, the fitted LO phonon energies after the EBF model are 19.97 meV, 19.42 meV and 18.21 meV for MAPbBr$_3$, MAPbI$_3$ and MAPbI$_{3-x}$Cl$_x$, respectively. In the case of MAPbBr$_3$ and MAPbI$_3$, we have applied eq. (4.8) to the FWHM obtained in Soufiani's work, for comparison purposes. The fit, presented in green lines in figures 4.2b and c, show a similar trend when compared to our results. In addition, the obtained LO phonon energy are within the range of $0 - 20$ meV of the phonon DOS calculated with first principles [199, 85, 51].

For the case of GaAs, the flatness of its FWHM make the fit imprecise, causing large uncertainties of the LO phonon energy. This behavior can be attributed to the lack of points of the absorption data (see figures 3.2a,b) around the exciton peak. Nevertheless, more tests on GaAs and other members of the group III-IV semiconductors need to be analyzed in order to confirm this trend.

Lastly, It is remarkable that the computed LO phonon energy, here obtained with the FWHM for tri-halide perovskites, is an stepping stone for the theoretical estimation of the binding energy of excitons in polar semiconductors as we will present in the next sections.

4.3   Thermal Evolution of Exciton Binding Energy

The results of extracting the exciton binding energy versus temperature for the 1s state of the exciton can be seen in figures 4.3 for GaAs and tri-halide perovskites. Here, GaAs shows a decreasing behavior, while tri-halide perovskites show small fluctuations around an average

Table 4.3 Parameters of the FWHM evolution with the temperature of the EBF model by fitting eq. (4.8) for tri-halide perovskites. Note that in all cases the acoustic term Γ_{AC} is set to zero due to the large Frölich interaction of the optical phonons for these semiconductors. Eq. 4.8 is applied to the data of Sturge [158] and Soufiani [154] as well, and the results are labeled with the superscripts (st) and (^{s}), respectively.

Material	Γ_0(meV)	Γ_{LO}(meV)	$\hbar\omega_{LO}$(meV)
MAPbBr$_3$	32.78 (1.60)	31.47 (20.4)	19.97 (9.04)
	38.93 (1.56)^{s}	36.73 (20.02)^{s}	19.97 (7.57)^{s}
MAPbI$_3$	23.05 (1.28)	44.5 (14.19)	19.42 (4.42)
	27.36 (1.04)^{s}	21.25 (7.61)^{s}	12.76 (3.70)^{s}
MAPbI$_{3-x}$Cl$_x$	26.02 (14.20)	30.7 (15.65)	18.21 (6.65)

energy value. In the former, the collected values are in the interval of 2-3.1 eV. These values share an small difference with the values reported at Sturge et al., as is seen in figure 4.3a. However, other studies report values of 4.2 meV [105, 36, 146]. This difference is attributed to the models for extracting the binding energy. For instance, Sestu et al. uses the sum rule on the absorption, Nam et al. retrieves it from PL and reflection measurements, and Fehrenbach et al. locates empirically the excitonic peaks from absorption measurements at low temperature.

In the case of tri-halide perovskites, we have values ranging from 22-33 meV, 15-19 meV and 21-25 meV for MAPbBr$_3$, MAPbI$_3$ and MAPbI$_x$Cl$_{3-x}$, respectively. These values are compared with the results reported in Soufiani et al. [154], plotted as red diamonds in figure 4.3b and c, where we see fluctuations of the binding energy for MAPbBr$_3$, whilst a detrimental behavior is shown for MAPbI$_3$. The here calculated binding energies are compared with the results of [154]. These values, presented as red diamonds, show oscillations of the binding energy for MAPbBr$_3$, while a decreasing behavior for MAPbI$_3$, as can be seen in figures 4.3-b and c, respectively.

The aforementioned binding energies are compared with other values from literature summarized in table 4.4. There, we observe that the here obtained binding energies for MAPbBr$_3$ are in agreement with temperature dependent PL experiments [108, 79] and high field magnetoabsorption [49]. Likewise, for the case of MAPbI$_3$, our results are comparable with values obtained with absorption [33], high field magnetoabsorption [102, 49] and PL [156]. However, for the case of MAPbI$_x$Cl$_{3-x}$, we do not have a coincidence with other reports despite being in the same order of magnitude. This can be attributed to the different sample preparations. However, these results are aligned with the theoretical prediction of the binding energy, whose value should be in the intermediate of iodide and chloride perovskites.

Table 4.4 Binding energies (B.E.) of the first excitonic state of different experimental reports for GaAs and tri-halide perovskites. For the case of halide pervoskites, the values reported are an update along with the data of [71]

Material	B.E.(meV)	Temperature	Method	Ref.
GaAs	4.2	2K	Photoluminescence	[105]
	4.2	1.2K	Absorption	[36]
	3.4-2.5	21-294K	Absorption	[158]
	4.2	1.2	Absorp. (F-sum rule)	[146]
$MAPbBr_3$	40.3	-	Absorption	[201]
	60	170-300/80-140K	Absorp. (F-sum rule)	[145]
	60	-	Absorption/PL	[196]
	53	-	Absorption/PL	[98]
	22-25	100-300K	PL at diff. T	[108]
	36-41	5-280K	Absorp. (F-sum rule)	[132]
	35-42	5-280K	Absorption	[132]
	15.33	4.5-150K	PL at diff. T	[169]
	76	4.2K	Magnetoabsorp.	[164]
	25	2K	High Field Magnetoabsorp.	[49]
	20-40	5K	Photoluminescence	[79]
	34-41	9-298K	Absorption	[154]
	64	-	Absorption	[134]
	71	-	Compuational Methods	[14]
$MAPbI_3$	15 (5)	50-162K (215-300K)	Absorption	[33]
	37	4.2K	Magnetoabsorp.	[64]
	16 (5)	8.5-145K (300K)	High Field Magnetoabs.	[102]
	13	-	Absorption	[201]
	50	4.2K	Magnetoabsorp.	[164]
	45	78-296K	Absorption	[66]
	24-32	5-280K	Absorp. (F-sum rule)	[132]
	22-29	5-280K	Absorption	[132]
	34 (29)	89-140K (170-300K)	Absorption (F-sum rule)	[145]
	25	170K and 300K	Absorption	[133]
	25-12	7-298K	Absorption	[154]
	9	300K	Absorption	[202]
	16 (12)	2K (155-190K)	High Field Magnetoabs.	[49]
	15-6	160-300K	Absorption	[198]
	19	10-300K	PL at diff. T	[156]
	30	-	Absorption	[78]
	2	4.2K	Magnetoabsorp.	[86]
	12.4	10-120K	Photocurrent at diff. T	[124]
	45	-	Computational Methods	[14]
$MAPbI_{3-x}Cl_x$	98	5-300K	PL at diff. T	[206]
	14 (10)	2K (190-200K)	High Field Magnetoabs.	[49]
	55($\pm$20)	160-300K	Absorption	[26]
	62	160-300K	PL at diff. T	[197]
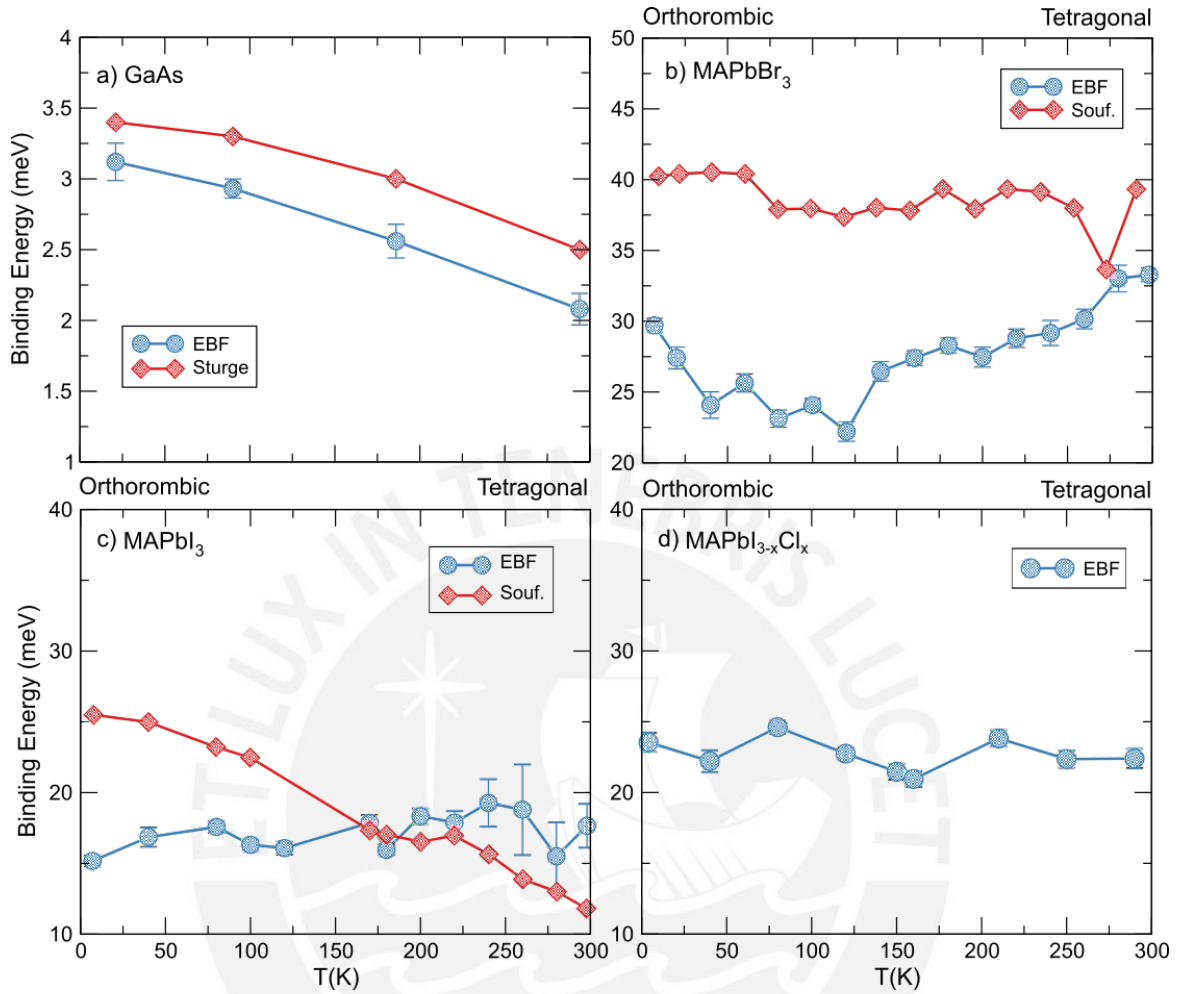
Fig. 4.3 Binding energy of the first excitonic state versus temperature retrieved by fitting the EBF model in optical absorption data of GaAs (a), $MAPbBr_3$ (b), and $MAPbI_3$-$MAPbI_{3-x}Cl_x$ (c). The data of figure (a) is compared with the results extracted from Sturge [158], while in figures (b) and (c) these are compared with Soufiani values [154]. We note that the binding energies in figures (b) and (c), collected with the EBF model, show oscillations with average values of 27.52 meV, 17.17 meV and 22.68 meV, for $MAPbBr_3$, $MAPbI_3$ and $MAPbI_{3-x}Cl_x$, respectively.

In addition, according to the fitting results of bandgap and binding energy, the concentration of the mixed halide perovskite is closer to $MAPbI_3$, i.e., $x \sim 3$.

The binding energies in table 4.4 show a large difference between several reports on the tri-halide perovskites. On the one hand, this might be attributed to differences in deposition conditions and, in particular, to degradation [166]. On the other hand, it could be attributed to the different techniques used to obtain the binding energy, for instance we have absorption, photoluminescence and magnetoabsorption. Each of these experiments

have different procedures to extract the binding energy. For example, in absorption, an Elliott fit is performed, in PL, the Arrhenius formula is employed, whilst in the case of magnetoabsorption, a modified Elliott equation with a magnetic potential is used [64]. These models for excitons are based on the hydrogen atom which does not accurately describe the case of perovskite systems, since the different binding energies detected in experiments at low and high magnetic fields indicate a large presence of electron-phonon interaction [6]. For instance, the formation of polarons could explain the enhancement of the carrier effective mass for low magnetic fields while for high magnetic fields, the carrier-lattice interaction is decoupled [6].

This implies that a further look into the formation of polarons in perovskites shall be done. In the following sections, we describe how the formation of polarons affects directly the absorption of the semiconductor.

4.4 Polarons in Perovskites

The existence of polarons in pervoskites has been found to be a useful explanation for various phenomena, such as the low mobility of carriers [143], slow carrier cooling [47], and their softness [103]. Polarons are formed due to the coupling between electronic states and longitudinal optical (LO) phonons, resulting in an electron dressed by the lattice polarization with an effective mass, which in the weak coupling regime is given by $m^*_{e,h} = m_{e,h}(1 + \alpha/6)$. The Fröhlich coupling constant α is defined by the expression [46, 6]:

$$\alpha = \frac{e^2}{\hbar} \left(\frac{1}{\varepsilon_\infty} - \frac{1}{\varepsilon_s} \right) \sqrt{\frac{m_{e,h}}{2\hbar\omega_{LO}}}. \tag{4.9}$$

Here, ε_∞ and ε_s is the optical and static electrical permittivity, respectively, and $\hbar\omega_{LO}$ is the LO phonon energy.

The combination of a large value of the effective dielectric screening ($1/\varepsilon^* = 1/\varepsilon_\infty - 1/\varepsilon_s$) [15] and a low phonon energy results in a high Fröhlich coupling constant as can be seen in table 4.5 for tri-halide perovskites. The polarons formed in these systems have been shown to interact with light, resulting in the creation of new states known as exciton-polarons. The work of Pollmann et al. [125] and Kane et al. [73] provides a detailed analysis of these states. The exciton Hamiltonian is modified to incorporate the electron-phonon interaction, which results in the binding energy being dependent on both the effective dielectric screening and the LO phonon energy. In the following section, we provide a brief overview of this model, emphasizing important concepts. In order to gain a deeper understanding of the concept of a

Table 4.5 Frölich coupling constant (α) of GaAs and tri-halide perovskites computed with eq. (4.9). The values used for the calculation were extracted from previous reports [154, 30]. In the case of MAPbI$_{3-x}$Cl$_x$, the values denoted as (*) are an average of the parameters for MAPbI$_3$ [154] and MAPbCl$_3$[143]. In addition, we have used the LO phonon energies retrieved by the Varshni equation for GaAs, and the FWHM fit for tri-halide perovskites. Lastly, previous values of α are written in parenthesis for comparison purposes. Note that the effective masses, m_e and m_h, are in terms of the unit mass of electron. ε_∞ and ε_0 are in units of the vacuum permittivity.

Material	α	m_e	m_h	ε_∞	ε_0	$\hbar\omega_{LO}$ (meV)
GaAs	0.072 (0.068^{sd})	0.077^d	0.865^d	10.9^d	12.9^d	37.08
MAPbBr$_3$	1.90 (1.69^{sd})	0.29^s	0.31^s	4.4^s	25.5^s	19.97
MAPbI$_3$	1.41 (1.72^{sd})	0.23^s	0.29^s	5^s	19.6^s	19.42
MAPbI$_{3-x}$Cl$_x$	1.94 (1.95^{sd})	0.32*	0.29*	4.5*	24.7*	18.21

polaron and the electron-phonon Hamiltonian used in the next section, we suggest that the reader consult appendix A.

4.4.1 Exciton-Polaron System: The Pollmann and Kane model

The formation of polarons through the coupling of electronic states to longitudinal optical phonons in a material leads to the creation of exciton-polarons, which can be thought of as a system consisting of two polarons of opposite charge interacting via the Coulomb interaction [60, 80]. The exciton-polaron can be visualized as an exciton dressed by a cloud of optical LO phonons, with the strength of its binding energy depending on the frequency of the phonons. Pollman, Buttner and Kane [125, 73] determined the ground state energy by considering the potential of the electron-hole interaction to be dependent of the quantum states of the polarons. In the present section we summarize their studies.

The Hamiltonian of an exciton interacting with the optical phonon field is:

$$H = H_{\text{exc}} + H_{\text{ph}} + H_{\text{exc-ph}} \tag{4.10}$$

where,

$$H_{\text{exc}} = \frac{P^2}{2M} + \frac{p^2}{2\mu} - \frac{e^2}{\varepsilon_\infty r}, \tag{4.11}$$

$$H_{\text{ph}} = \sum_q \hbar \omega_{LO} \hat{b}_q^\dagger \hat{b}_q, \tag{4.12}$$

$$H_{\text{el-ph}} = \sum_q V_q \left(\hat{b}_q e^{ik \cdot (\frac{m_2^*}{M} r + R)} + \hat{b}_q^\dagger e^{-ik \cdot (\frac{m_2^*}{M} r + R)} \right) \tag{4.13}$$

$$+ V_q \left(\hat{b}_q e^{-ik \cdot (\frac{m_1^*}{M} r - R)} + \hat{b}_q^\dagger e^{ik \cdot (\frac{m_1^*}{M} r - R)} \right), \tag{4.14}$$

and,

$$V_q = -\frac{i}{q} \sqrt{\frac{2\pi e^2 \hbar \omega_{LO}}{\varepsilon_{eff}}} \tag{4.15}$$

Here m_1^* and m_2^* are the electron and hole effective band masses, respectively. The coordinates R, P and M refer to the variables of position, momentum and mass of the center of mass; while r, p and μ represent the same quantities but in relative coordinates. The Pollman procedure is based on applying a canonical transformation to H for obtaining an upper limit of the ground state of the system, i.e.,

$$\hat{H} = U_1^{-1} U_2^{-1} H U_1 U_2 \tag{4.16}$$

The canonical transformation is performed by the operators U_1 and U_2 which correspond to the relative and center of mass coordinates, respectively:

$$U_1 = e^{-i\sum_q q b_q^\dagger b_q \cdot R} \tag{4.17}$$

$$U_2 = e^{\sum_q f_q(r) b_q - f_q a_q^\dagger} \tag{4.18}$$

The meaning of the canonical transformation is that instead of working with the full solution of the exciton-polaron system, $|\psi\rangle$, we separate the contribution of the electron-phonon interaction trough the unitary functions U_1 and U_2 [84, 125]. So, now we can work with the exciton wave function as in the Hydrogen like model, $|\phi(r)\rangle$. By separating variables, the energy of the system is computed as:

$$E = \langle \phi | \hat{H} | \phi \rangle, \tag{4.19}$$

Following the procedure of Pollmann and Kane, the minimization of eq. 4.19 give the upper bound of the ground state energy of the exciton-polaron. This binding energy is obtained in a

set of self consistent equations that depend on the hydrogen wave functions, the static and high frequency dieletric constants, the LO phonon energy and the effective band masses of electron and hole, i.e.:

$$E_{BE} = -|E_\infty|G_1 G_2, \tag{4.20}$$

$$G_n = 1 - \left(1 - \frac{\varepsilon_\infty}{\varepsilon_0}\right) F_n, \tag{4.21}$$

$$F_1 = \frac{2}{\pi} F_d; \; F_2 = \frac{2}{\pi}(2F - F_d), \tag{4.22}$$

$$F_d = F + 2\left(\eta_1 \frac{\partial F}{\partial \eta_1} + \eta_2 \frac{\partial F}{\partial \eta_2}\right), \tag{4.23}$$

$$F = \int_0^\infty \left(E_{k\,min}^A + A_{11}^{-1} + A_{22}^{-1} + E_{k\,min}^B\right) dx, \tag{4.24}$$

$$\beta = \beta_\infty G_1, \; \beta_\infty = \frac{e^2 \mu}{\hbar^2 \varepsilon_\infty}, \tag{4.25}$$

$$\eta_n = 2\frac{\hbar^2 \beta_\infty^2 G_1^2}{m_n \hbar \omega_{LO}}, \; |E_\infty| = \frac{e^4 \mu}{2\hbar^2 \varepsilon_\infty^2} \tag{4.26}$$

with:

$$E_{k\,min}^A = \frac{2A_1 A_2 A_{12} - A_{11} A_2^2 - A_{22} A_1^2}{4\left(A_{11} A_{22} - A_{12}^2\right)} \tag{4.27}$$

$$A_{nn} = 1 + \frac{\hbar^2 k^2}{2m_n \hbar \omega_{LO}} \tag{4.28}$$

$$A_1 = A_2 = 2(1 - R_{00}) \tag{4.29}$$

$$A_{12} = -R_{00} \tag{4.30}$$

$$R_{00} = -\frac{1}{(1+x^2)^2}, \; x = \frac{k}{2\beta} \tag{4.31}$$

and,

$$E^B_{k\ min} = \frac{2B_1B_2B_{12} - B_{11}B_2^2 - B_{22}B_1^2}{4\left(B_{11}B_{22} - B_{12}^2\right)} \tag{4.32}$$

$$B_{nn} = \frac{4}{3}\beta^2\sigma_n^2 x^2\left(1 + \eta_1 + \eta_2 + \eta_n x^2\right) \tag{4.33}$$

$$B_n = -4\beta\left(\sigma_n x^2 R_{00} + \frac{1}{3}\sigma_n^2 x^2 \eta_n + \sigma_1\sigma_2\left(\eta_{\tilde{n}}\delta + x^2 R_{00}\right)\right) \tag{4.34}$$

$$B_{12} = 4\beta^2\sigma_1\sigma_2\left(\delta - R_{00}x^4 + (\eta_1 + \eta_2)\delta\right) \tag{4.35}$$

$$\sigma_n = \frac{A_{12}A_{\tilde{n}} - A_{\tilde{n}\tilde{n}}A_n}{2(A_{11}A_{22} - A_{12}^2)} \tag{4.36}$$

$$\delta = 1 - \frac{1}{x\text{Tan}(x)}, \tilde{n} = \tilde{1} = 2, \tilde{2} = 1. \tag{4.37}$$

Convergence of the calculated binding energy from these equations is relatively quick (taking just ten steps) for the tri-halide perovskites. In the next subsection we present the results of the Kane model applied to the family of tri-halide perovskites.

4.4.2 Exciton-Polaron Contribution Results

We have reproduced the exciton-polaron binding energies found by Soufiani et al. [154] for the LO phonon energies from 0 up to 20 meV with the parameters, m_e, m_h ε_∞, ε_0 extracted from [154, 155] for MAPbBr$_3$ and MAPbI$_3$. This is illustrated in figure 4.3 in blue an yellow colors, respectively. Likewise, by using an average value of MAPbI$_3$ [154] and MAPbCl$_3$ [143], we have obtained the binding energies of the the mixed halide pervoskite, MAPbI$_x$Cl$_{3-x}$. This is presented in red colored symbols shown in figure 4.4. It is remarkable to say that the variability of the parameters of m_e, m_h, ε_0 and ε_∞ found in literature have set upper and lower bounds for the here calculated binding energy. From figure 4.4, we can see that the binding energy of the exciton-polaron can acquire different values depending on the phonon branch they are coupling. This, perhaps, can be an explanation of the large difference in binding energy calculated with different experiments. Moreover, we have performed this procedure on the non-polar case of GaAs for completeness purposes. This is presented in the inset of figure 4.4 by pink asterisks, and was calculated by using values extracted from [30] for a set of phonon energies around the Debye energy.

Our LO phonon energies of the tri-halide perovskites obtained in the FWHM section appear in figure 4.4 as the vertical dashed lines. There, the intersections mark the binding energies of the Kane's model with values of 3.86-25.91 meV, 1.63-16.52 meV and 5.65-27.39 meV for MAPbBr$_3$, MAPbI$_3$ and MAPbI$_x$Cl$_{3-x}$, respectively. Remarkably, these

values from the intersections are in agreement with the binding energies retrieved by the EBF model. Thus, confirming the reliability of the model.

The ability of the EBF model to predict the low values of the exciton binding energy may imply that the concept of lattice deformations behind the band-fluctuations potential of eq. (3.25) is also mapped into the polaronic contribution for polar and ionic materials.
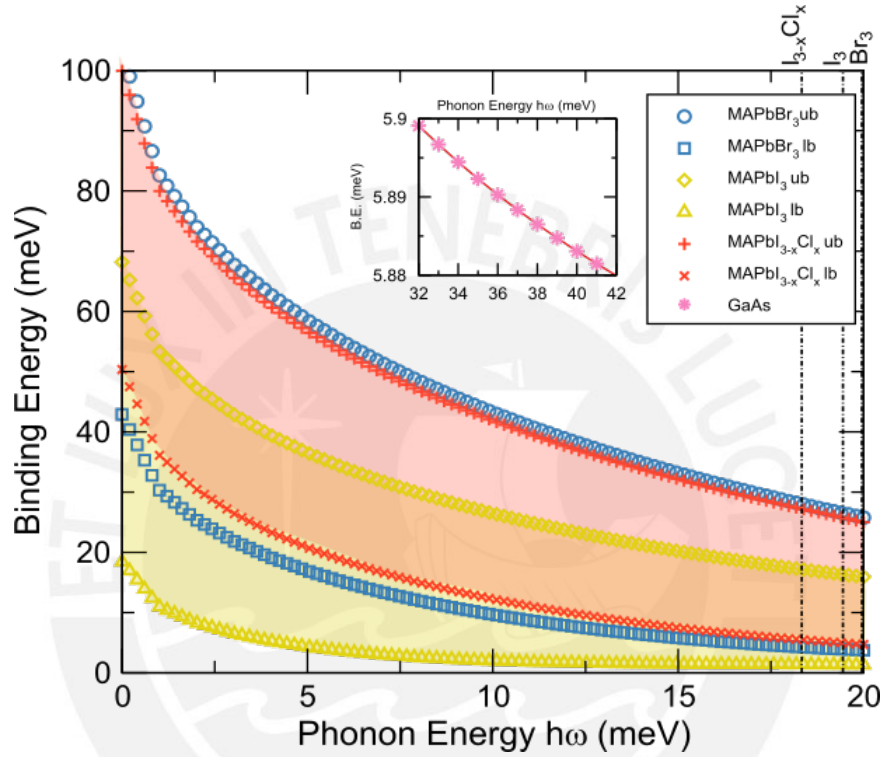
Fig. 4.4 Exciton-polaron binding energy calculated with the Kane's model [73], for different LO phonon wavelengths and starting parameters. These parameters were extracted from [154, 143, 30]. In addition, we have reproduced the work of Soufiani et al. for the upper (ub) and lower (lb) bounds of MAPbBr$_3$ and MAPbI$_3$. The computed values are MAPbBr$_3$-ub ($\varepsilon_\infty = 4.4$, $\varepsilon_s = 25.5$, $m_e = 0.29$, $m_h = 0.31$), and MAPbBr$_3$-lb ($\varepsilon_\infty = 4.8$, $\varepsilon_s = 25.5$, $m_e = m_h = 0.15$) in blue symbols; MAPbI$_3$-ub ($\varepsilon_\infty = 5$, $\varepsilon_s = 19.6$, $m_e = 0.23$, $m_h = 0.29$) and MAPbI$_3$-lb ($\varepsilon_\infty = 6.5$, $\varepsilon_s = 28.8$, $m_e = m_h = 0.12$) in yellow marks; MAPbI$_x$Cl$_{3-x}$-ub ($\varepsilon_\infty = 4.5$, $\varepsilon_s = 24.7$, $m_e = 0.32$, $m_h = 0.29$) and MAPbI$_x$Cl$_{3-x}$-lb ($\varepsilon_\infty = 5.25$, $\varepsilon_s = 29.3$, $m_e = 0.165$, $m_h = 0.29$) in red tokens. In the inset we can see the case of GaAs ($\varepsilon_\infty = 10.9$, $\varepsilon_s = 12.9$, $m_e = 0.077$, $m_h = 0.865$) presented as pink marks. The vertical dashed black lines denotes the LO phonon energy calculated from the FWHM fit.

4.5   Effective Mass

The method of deducing effective masses based on the binding energy can be perceived as an outcome of reversing the equations established by Kane's model. In contrast to Kane's approach where effective masses are fixed in the self-consistent calculation, our method fixes the LO phonon energy instead. This allows us to calculate the binding energy of the exciton-polaron system within a variable mass range. Thus, if we have the binding energy of the system, such as those obtained from the EBF model, we can derive a specific set of values for the effective masses. It should be noted that the LO phonon energy employed is the one obtained previously from the bandgap and FWHM thermal evolution. This is presented in table 4.6.

Figures 4.5, 4.6 and 4.7 depict the surface plot of the binding energy for MAPbBr$_3$, MAPbI$_3$, MAPbI$_{3-x}$Cl$_x$. In these graphs, the horizontal and vertical axes represent the electron and hole band masses, respectively. The colors on each graph correspond to different binding energy values. The LO phonon energies used in the figures 4.5 a, b, 4.6 a, b, 4.7 a and b, were obtained from the thermal evolution of the bandgap using Cardona's model for the orthorombic and tetragonal phases [17]. In the case of figures 4.5 c, 4.6 c and 4.7 c. the value used correspond to the one retrieved in the evolution of the FWHM with Toyozawa's model. Additionally, the binding energy retrieved by the hydrogen model for excitons is presented in figures 4.5 d, 4.6 d and 4.7 d. Here, the ε_∞ is used in the calculation instead of the ε_{eff} of the Kane's model. For all perovskites, the effective masses and electrical permittivities were selected based on the literature reports. These correspond to the studies of Dubey et al. for GaAs, Soufiani et al. [154, 155] and Sendner et al. [143] for the tri-halide perovskites.

For the case of MAPbBr$_3$, the electron and hole band masses used as reference were 0.29 and 0.31, respectively [154]. This reference point is colored in blue and present the differences in the binding energy of figures 4.5 a, b, c and d. As we can notice, the binding energy heavily depends on the LO phonon energy of the system. For lower values of the LO phonon energy, the exciton is dressed by more phonons, causing it to be more tightly bound. In figures 4.5 a, b and c, we have plotted the area covering the values of the binding energy obtained from the EBF model, i.e., 22-33 meV. This region is filled with the medium-size white points, for visualization purposes. In addition, the average binding energy of this region, 27.57 meV, is presented in sky-blue dashed lines, whose location depend of the surface map calculation. Here, we notice that in all cases, the reference blue point is located close to the average binding energy and is inside the binding energy region of the EBF model. This implies that we can predict a ratio for the electron and hole effective masses with only the parameters of the optical properties. Lastly, the binding energy of the Hydrogen-like

MAPbBr₃

Fig. 4.5 Binding energy of MAPbBr$_3$ surface map, calculated with Kane and hydrogen model, in function of the electron (x-axes) and hole (y-axes) effective masses. Figure a, b and c were calculated using the Kane's model with variable mass and fixed LO phonon energies of 17.29 meV (orthorombic), 17.97 meV (tetragonal) and 19.97 meV (FWHM), see table 4.6, respectively. The static electrical permittivity and high frequency electrical permittivity used for figures a, b and c are 25.5 and 4.4, respectively. Figure d shows the calculation using the Hydrogen atom model in which the value of the permittivity is the one for an infinite frequency (4.4). In all figures, blue point represents the effective masses of the literature and the corresponding binding energy calculated with the aforementioned models. Lastly, the binding energy values obtained from the EBF model are plotted as the region filled with white middle-size points. In addition, the average binding energy of these values is presented in sky-blue dashed lines. Note that the effective masses are in terms of the electron mass unit and electrical permittivities are in terms of the vacuum permittivity.

model is calculated for comparison purposes. This is shown in figure 4.5 d, here the value of the binding energy is 105.3 meV is five times the value of the Kane's model.

The reference electron and hole band masses used for $MAPbI_3$ were 0.23 and 0.29, respectively, as reported by Soufiani [154]. This reference point is highlighted in blue and illustrates the differences in binding energy in figures 4.6 a, b, c, and d. It is observed that the binding energy is significantly affected by the LO phonon energy like in the case of $MAPbBr_3$. In figures 4.6 a, b, and c, the binding energy region, 15-19 meV, and the average binding energy, 17.17 meV, obtained from the EBF model, are plotted using the middle-size white points and the sky-blue dashed lines, respectively. In the cases where the LO phonon energy is in the range of $18.83 - 19.42$ meV, the reference blue point fall is close to our average binding energy. Nevertheless, the LO phonon energy of the tetragonal phase (figure 4.6 b) causes a large difference between binding energies of the EBF and the Kane's model. This can be understood from the large variability of the LO phonon energy when the temperature dependent bandgap was fitted by using Cardona's model with thermal expansion and electron-phonon terms. In fact, the LO phonon energy retrieved by the thermal evolution of the FWHM, described in section 4.2, produces the closest value to the effective mass of other reports. For this energy, the proximity of the binding energy (figure 4.6 c) suggests that effective masses of $MAPbI_3$ can be predicted by only using parameters of the optical properties. Finally, for comparison, the binding energy of the Hydrogen model is calculated and presented in figure 4.6 d.

For the case of the $MAPbI_{3-x}Cl_x$, the electron and hole band masses used as a reference were 0.32 and 0.29, respectively. These where computed by averaging the effective masses of $MAPbI_3$ and $MAPbCl_3$ as described in section 4.3. These are highlighted in blue in the figures 4.7 a, b, c, and d, which show the differences in binding energy. Similarly to the aforementioned cases, it is observed that the LO phonon energy has a significant impact on the binding energy. In figures 4.7 a, b, and c, the values obtained in the EBF model are presented in the form of the binding energy region, 21-25 meV, filled with white points, and the average binding energy, 22.68 meV, presented as sky-blue dashed lines. It is noted that, only in the case of the LO phonon energy of 20.72 meV (figure 4.7-b), the theoretical reference blue point fall inside our EBF region. And, in the cases of the LO phonon energies of 19.56 and 18.21 meV of figures 4.7 a and c, respectively, our EBF region is close to the Kane's predicted value. Nonetheless, this small difference can be attributed to the empirical effective band masses used for the exciton-polaron model (see table 4.5). The effective masses may not evolve linearly as we are expecting for the mixed composition of this halide perovskite. According to literature, they can vary following an exponential behavior, or they
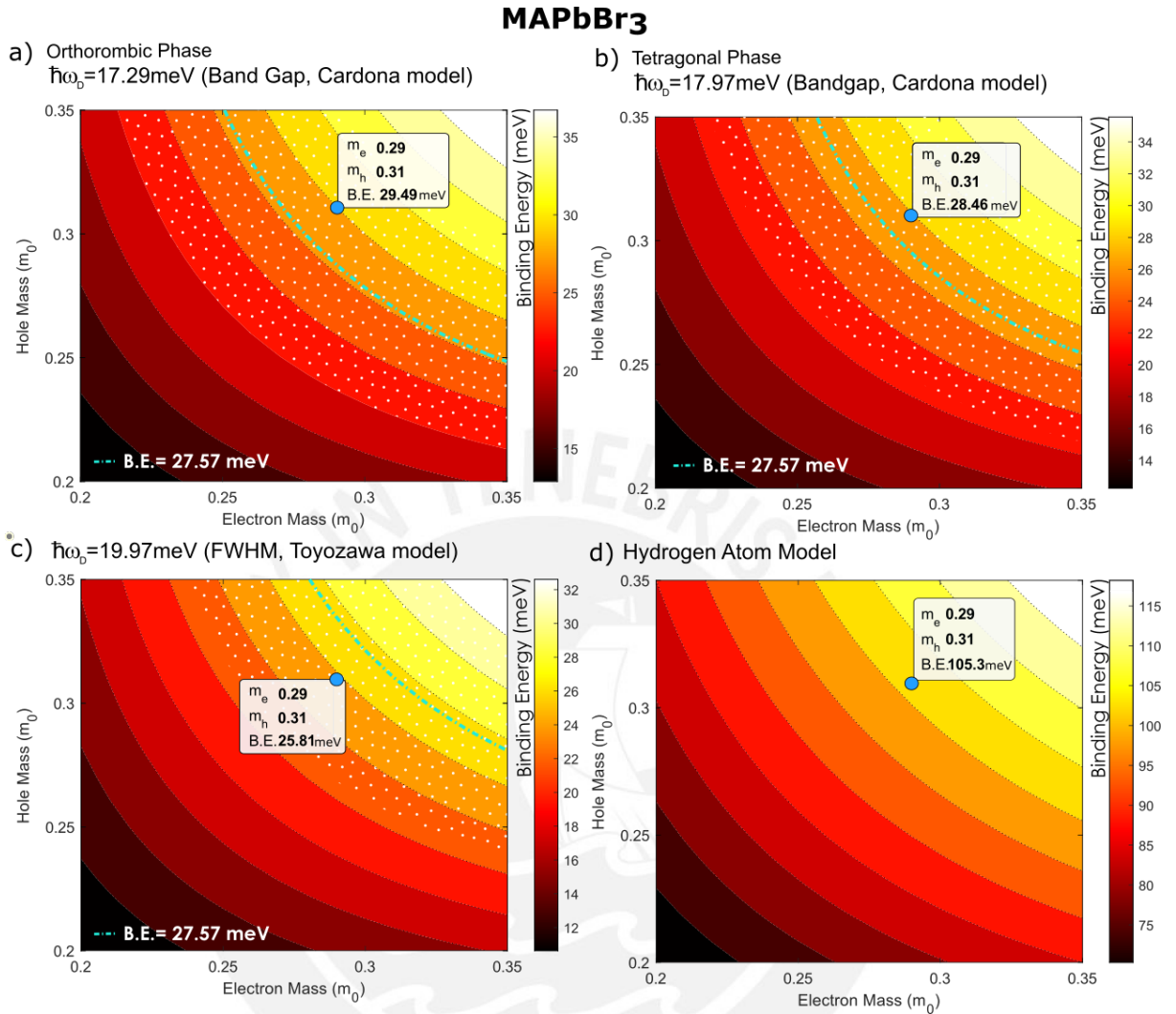
MAPbI$_3$
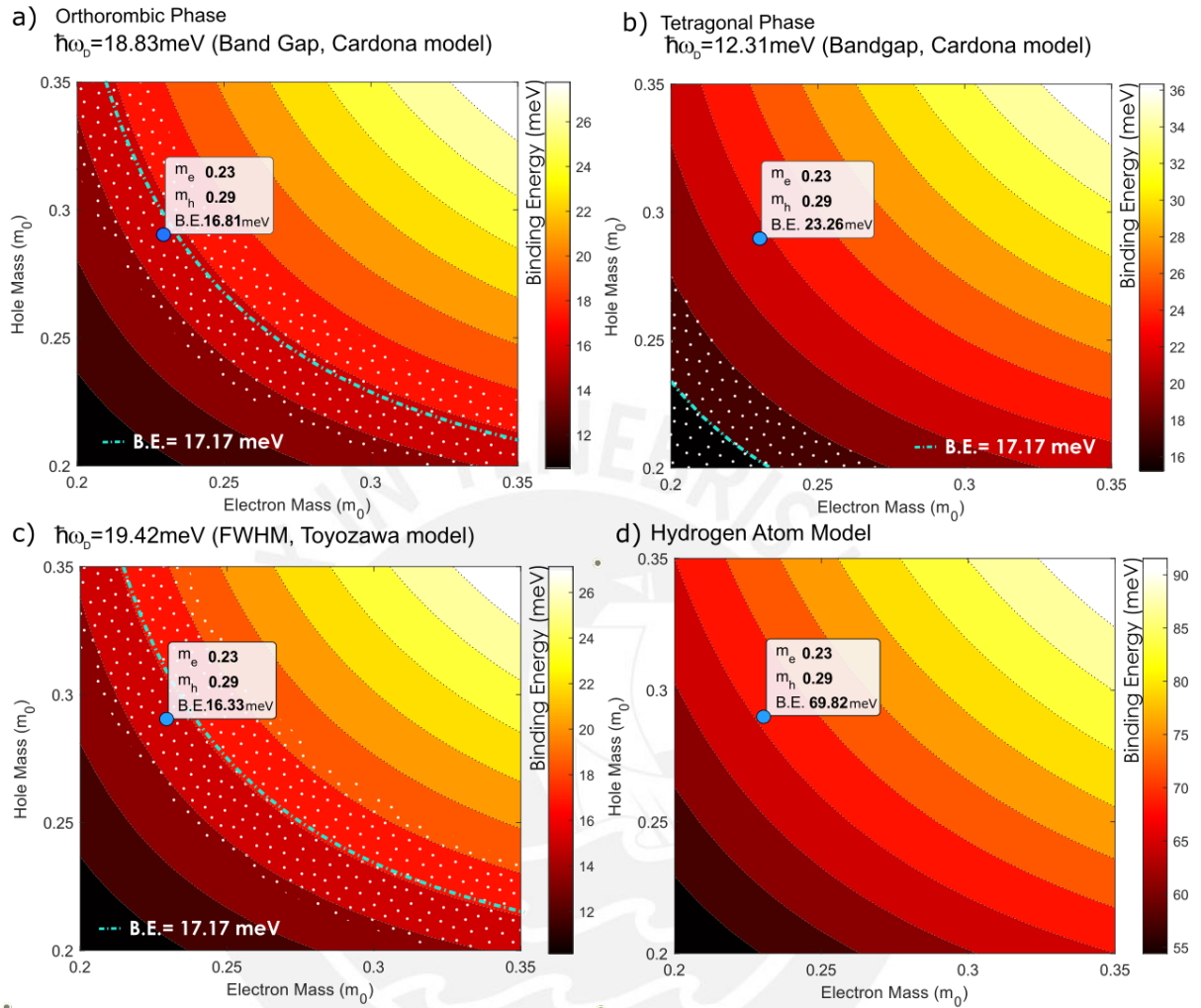
Fig. 4.6 Binding energy of MAPbI$_3$ surface map, calculated with Kane and hydrogen model, in function of the electron (x-axes) and hole (y-axes) effective masses. Figure a, b and c were calculated using the Kane's model with variable mass and fixed LO phonon energies of 18.83 meV (orthorombic), 12.31 meV (tetragonal) and 19.42 meV (FWHM), see table 4.6, respectively. The static electrical permittivity and high frequency electrical permittivity used for figures a, b and c are 19.6 and 5, respectively. Figure d shows the calculation using the Hydrogen atom model in which the value of the permittivity is the one for an infinite frequency (5). In all figures, blue point represents the effective masses of the literature and the corresponding binding energy calculated with the aforementioned models. Lastly, the binding energy values obtained from the EBF model are plotted as the region filled with white middle-size points. In addition, the average binding energy of these values is presented in sky-blue dashed lines. Note that the effective masses are in terms of the electron mass unit and electrical permittivities are in terms of the vacuum permittivity.
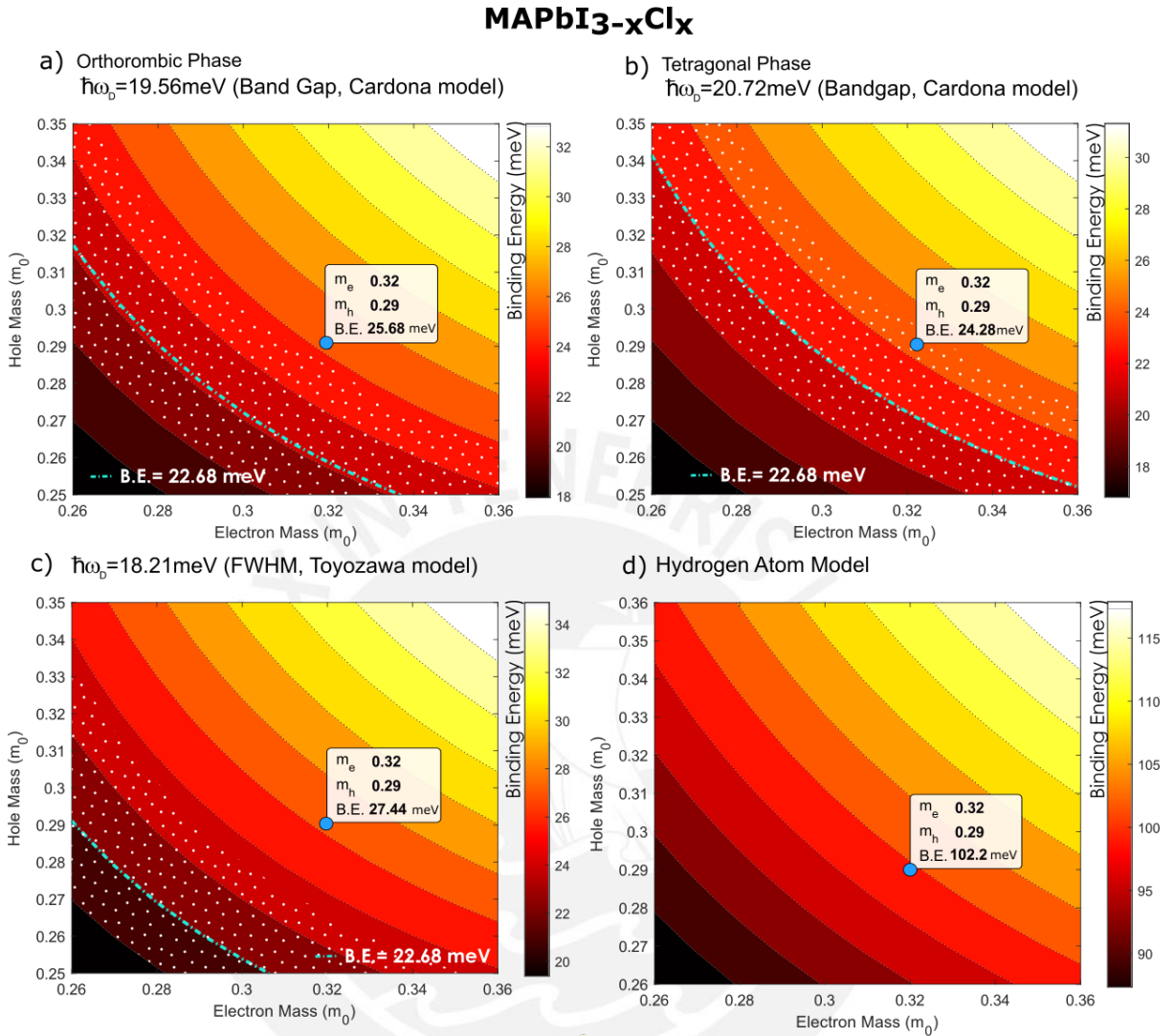
MAPbI$_{3-x}$Cl$_x$

Fig. 4.7 Binding energy of MAPbI$_{3-x}$Cl$_x$ surface map, calculated with Kane and hydrogen model, in function of the electron (x-axes) and hole (y-axes) effective masses. Figure a, b and c were calculated using the Kane's model with variable mass and fixed LO phonon energies of 19.56 meV (orthorombic), 20.72 meV (tetragonal) and 18.21 meV (FWHM), see table 4.6, respectively. The static electrical permittivity and high frequency electrical permittivity used for figures a, b and c are 24.7 and 4.5, respectively. Figure d shows the calculation using the Hydrogen atom model in which the value of the permittivity is the one for an infinite frequency (4.5). In all figures, blue point represents the effective masses of the literature and the corresponding binding energy calculated with the aforementioned models. Lastly, the binding energy values obtained from the EBF model are plotted as the region filled with white middle-size points. In addition, the average binding energy of these values is presented in sky-blue dashed lines. Note that the effective masses are in terms of the electron mass unit and electrical permittivities are in terms of the vacuum permittivity.

can even fluctuate [22, 163]. Lastly, the binding energy of the Hydrogen model is calculated and presented in figure 4.6 d for comparison purposes.

4.6 Thermal Properties

Table 4.6 Collected LO phonon energies from the fits of the thermal evolution of bandgap and FWHM. The former was fitted in section 4.1 with the models of Cardona [17] and Varshni [179]. The latter was fitted with the model of Toyozawa [171]. "Cardona's model TE + EP" reefers to the model developed by Cardona et al. were the thermal expansion and electron phonon terms are considered. "Cardona's model EP only" implies only the electron-phonon coupling of the thermal evolution of the bandgap.

Material	$\hbar\omega_{LO} \approx \hbar\omega_D$ (meV)	Obtention Method
GaAs	35.74	Band Gap (Cardona's model TE+EP)
	22.31	Band Gap (Cardona's model EP only)
	37.08	Band Gap (Varshni's model)
MAPbBr$_3$	17.29 (Ortho. Ph.)	Band Gap (Cardona's model TE+EP)
	17.97 (Tetr. Ph.)	Band Gap (Cardona's model TE+EP)
	19.97	FWHM (Toyozawa model)
MAPbI$_3$	18.83 (Ortho. Ph.)	Band Gap (Cardona's model TE+EP)
	12.31 (Tetr. Ph.)	Band Gap (Cardona's model TE+EP)
	19.42	FWHM (Toyozawa model)
MAPbI$_x$Cl$_{3-x}$	19.56 (Ortho. Ph.)	Band Gap (Cardona's model TE+EP)
	20.72 (Tetr. Ph.)	Band Gap (Cardona's model TE+EP)
	18.21	FWHM (Toyozawa model)

Having described the reliability of the optical parameters in different scenarios such as the thermal evolution of bandgap,and overall broadening quantified by the FWHM, with the binding energy of the exciton-polaron system, and even for structural properties such as the effective band mass, now we test the goodness of these parameters to predict the behavior of the thermodynamic quantities such as the Specific Heat (C_v), Helmholtz Free Energy (F), Internal energy (U) and Entropy (S). The importance of these quantities were discussed

in chapter 1. Here we briefly discuss the equations describing this quantities which are explained in detail in appendix B. These expressions are in terms of the density of states of the phonons. For this reason, we use Debye's theory that models the phonon density of states to account acoustical and optical branches in the same level [65]. This implies a definition of a cutoff phonon energy known as Debye's energy. And, due to its experimental closeness with the LO phonon energy [121], this energy is taken from the thermal evolution fits of the bandgap and FWHM. For our systems of GaAs and tri-halide perovskites, we show the Debye energies in table 4.6. Later in this section, the results of the thermodynamic quantities of GaAs and tri-halide perovskites are presented.

4.6.1   Thermodynamic Quantities

The following expressions are taken from references [185, 5, 93]. An extended summary of them can be found in appendix B. The specific heat of a solid in terms of the phonon density of states is:

$$C_v(T) = k_\beta \int G(\omega) \left(\frac{\hbar\omega}{k_\beta T} \right)^2 \frac{e^{\hbar\omega/(k_\beta T)}}{\left(e^{\hbar\omega/(k_\beta T)} - 1 \right)^2} d\omega \tag{4.38}$$

The Helmholtz free energy follows the relation:

$$F(T) = E_0 + k_\beta T \int_0^{\omega_D} G(\omega) \log\left(1 - e^{-\frac{\hbar\omega}{k_\beta T}} \right) d\omega, \tag{4.39}$$

where,

$$E_0 = \frac{1}{2} \int G(\omega) \hbar\omega d\omega. \tag{4.40}$$

In addition, the internal energy has the following expression:

$$U(T) = E_0 + k_\beta T \int_0^{\omega_D} \left(\frac{\hbar\omega}{k_\beta T} \right) \frac{G(\omega)}{e^{(\hbar\omega/(k_\beta T))} - 1} d\omega. \tag{4.41}$$

Lastly, the entropy is obtained by $S(T) = (U(T) - F(T))/T$, i.e.:

$$S(T) = k_\beta \int_0^{\omega_D} \left(\frac{\hbar\omega}{k_\beta T} \right) \frac{G(\omega)}{e^{(\hbar\omega/(k_\beta T))} - 1} - G(\omega) \log\left(1 - e^{-\frac{\hbar\omega}{k_\beta T}} \right) d\omega. \tag{4.42}$$

We select the density of states from the Debye's theory due to its success for explaining the population of states of the phonons. This is a consequence of the Debye's function shaping

correctly the specific heat at low temperatures [65].

$$G(\omega) = 9n\hbar \frac{(\hbar\omega)^2}{(\hbar\omega_D)^3}\Theta(\omega_D - \omega). \tag{4.43}$$

Here n is the number of atoms in the solid, and $\omega_D = k_\beta T_D/\hbar$. The Debye DOS make equations 4.38, 4.39, 4.41 and 4.42 simpler for numerical computation. For instance, we are left with a specific heat of the form:

$$C_v = 9nk_\beta \left(\frac{T}{\theta_D}\right)^3 \int_0^{\theta_D/T} \frac{x^4 e^x}{(e^x - 1)^2} dx, \tag{4.44}$$

where the variable x represents $\hbar\omega/(k_\beta T)$. Note that in the majority of studies of the thermodynamic quantities, the units are in terms of mol^{-1}. For example, in the case of specific heat, the unit is $J.mol^{-1}K^{-1}$, however, our derived equations are only in terms of $J.K^{-1}$. For solving this problem, the number of particles in the system n needs to be transformed into a quantity that is independent of the molar mass. That means, n becomes the number of atomic species in the stoichiometry (N) times the Avogadro number (N_a). For instance, the number of atomic species in cases such as GaAs have a value of two, while in cases such as In_2O_3 it gets a value of five. Nonetheless, for the halide perovskite cases, e.g. for MAPbBr$_3$, the value of N is taken as six (counting one time CH$_3$, NH$_3$ and Pb, and three times Br) instead of the corresponding value of twelve. The reason behind the selection of this value is to compare it with the available data from previous studies of Onoda et al. [92]. Likewise, the iodide and chloride-iodide mixture perovskites follow the same value for N.

4.6.2 Thermal Properties Estimation Results

The specific heat, Helmholtz energy, internal energy and entropy for GaAs are shown in figures 4.8 a, b, c and d, respectively. These curves were calculated by using equations 4.38, 4.39, 4.41 and 4.42 in the framework of the Debye's theory for describing the distribution of phonons. The LO phonon energies of the colored (blue, green and orange) lines were extracted from the evolution of the bandgap and FWHM which are presented in table 4.6. In the particular case of figure 4.8 a, the black set of data were extracted from the experimental results found at Landolt et al.[19]. In addition, the red set of points corresponds to the best fitted Debye energy, and has a value of 29.63 meV [19]. This value is close to our calculated values of 22.31 and 35.74 retrieved by the thermal evolution of the bandgap and FWHM, respectively. In figure 4.8 a, the former value describes better the initial onset of the curve, while the latter describes it better for high temperatures. Despite not having experimental

data to compare the Helmholtz energy, internal energy and entropy, we can describe general features of the curves. In the case of Helmholtz energy, the lower the phonon energy, the quicker the system loses energy with respect of its environment ($F = U - TS$) since the work TS grows faster than the internal energy. Naturally, at temperatures from 0K up to 300K, the initial onset of the internal energy is larger than TS and so the Helmholtz energy is positive in this region. On the other hand, the internal energy of all systems evolve independently from LO phonon energy at high temperatures. This result is expected since at temperatures above 500K ($kT = 43.08$ meV) all phonon frequencies have been excited. Thus the internal energy no longer depends on the optical branches, but instead on kinetic energy. Lastly, for the case of the entropy, the system with low Debye energy is the one that grows faster. This can be understood from the point that in a system with low energy LO phonons, the phonon branches become active quicker as temperature risese.

For perovskite systems, we depict the specific heat, Helmholtz energy, internal energy, and entropy of MAPbBr$_3$ in figures 4.9 a, b, c, and d, respectively. The LO phonon energies of the green, orange, and purple lines were obtained from the bandgap and FWHM evolution presented in table 4.6. In addition, the black data in figure 4.9a were extracted from experimental results by Onoda et al. [92]. In their study, they fit the specific heat by using a comprenhensive model that includes modeling of internal vibrations, rotations, librations, and the acoustic and optical phonons. As a consequence, they report two and three different values of of the Debye and Einstein temperatures, respectively. Here, we report those Debye temperatures as blue (9.22 meV) and red (16.72 meV) curves. The former presents an upper bound, while the latter is a lower bound in the specific heat. The value of 16.72 meV is the closest to our values of 17.97 meV, 17.29 meV and 35.74 meV. Notably, the specific heat curves retrieved by using the analysis and models presented here appear slightly below the lower bound found by Onoda et al. As for the Helmholtz energy and entropy, figure 4.9b and d indicate that the curves retrieved from the optical analysis share a similar trend as the curve derived from Onoda's highest value. Additionally, figure 4.9c shows that at high temperatures, the internal energy becomes independent of the Debye's energy value.

For MAPbI$_3$, we present the specific heat, Helmholtz energy, internal energy, and entropy in figures 4.10 a, b, c, and d, respectively. The LO phonon energies of the green, orange, and purple lines were determined based on the thermal evolution of the optical parameters provided in table 4.6. Like in the case of MAPbBr$_3$, the analysis of Onoda et al. resulted in two values of the Debye energy. These values are 7.76 meV and 10.51 meV, they give rise to the curves presented as blue and red in figure 4.10. Interestingly, in figure 4.10a, the value of the Debye energy of 10.51 meV seems to fit the experimental data (black lines) up to a temperature of 100K. Our Debye energy value of 12.31 meV, for the tetragonal phase,
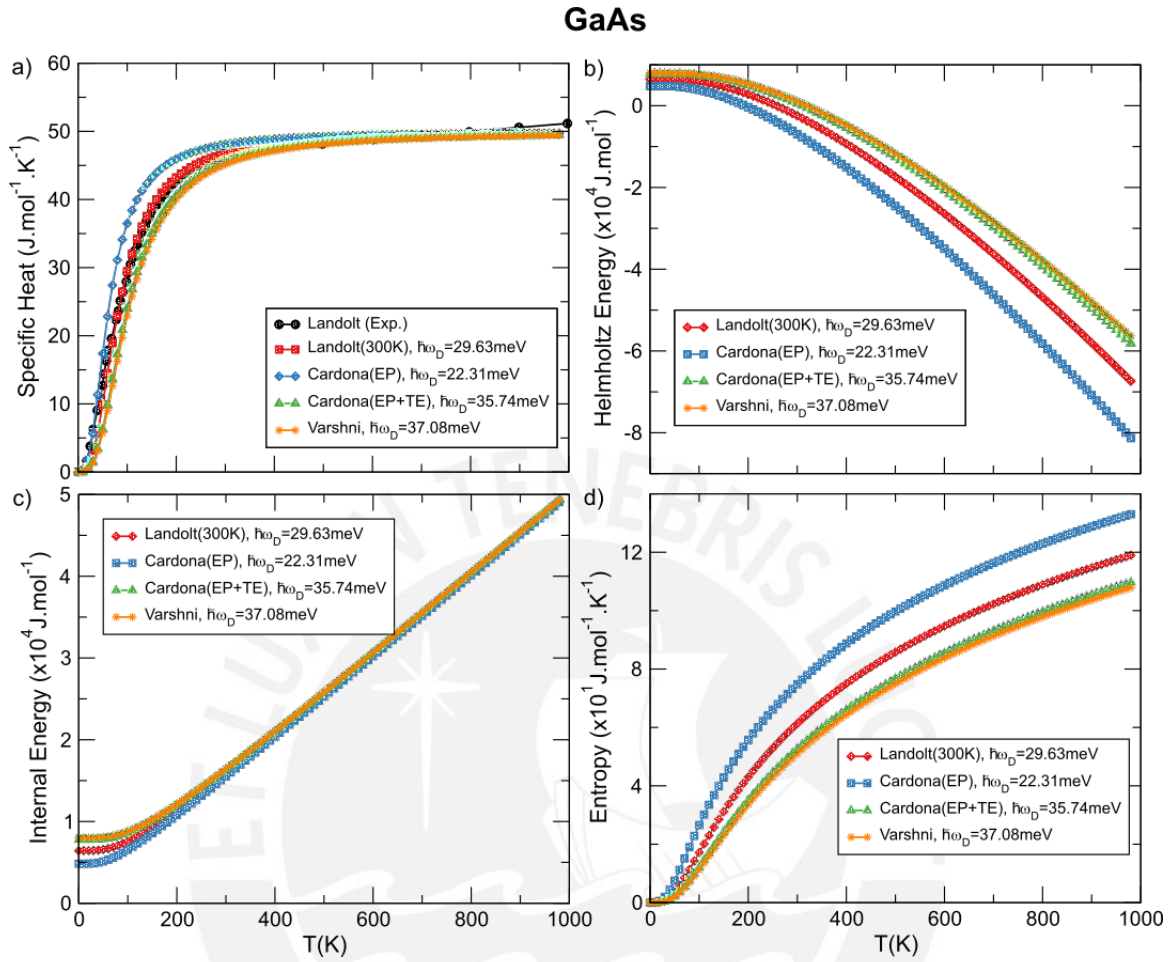
Fig. 4.8 Thermodynamic quantities of GaAs. Specific heat (C_v), Helmholtz Energy (F), Internal Energy (U) and Entropy (S) are shown in figures a, b, c and d, respectively. In these figures, the set of points colored as blue, green and orange correspond to the Debye energy, of 22.31 meV, 35.74 meV and 38.08 meV, respectively (see table 4.6). In addition, the red line shows the curve generated with the value of $\hbar\omega_D = 29.63$ meV reported in [19]. Lastly, in figure a, the experimental measurement of specific heat is presented in black.

produce a curve similar to Onoda's result. The large values, obtained with the optical analysis, of 18.83 meV and 19.42 meV lie below the expected behaviour. Nevertheless, this difference can be explained from our raw consideration of the Debye model for the specific heat. In fact, the shape of the specific heat is composed by several contributions as explained in Onoda et al. [92]. In contrast, our Helmholtz energy, internal energy and entropy curves (figure 4.9b, c and d) for a Debye energy of 12.31 meV follow a similar trend as the curve obtained using Onoda's highest value. One more time, the low value of Debye energy affects the entropy strongly, undergoing a more rapid increase as low energy phonon branches become active at low temperatures.
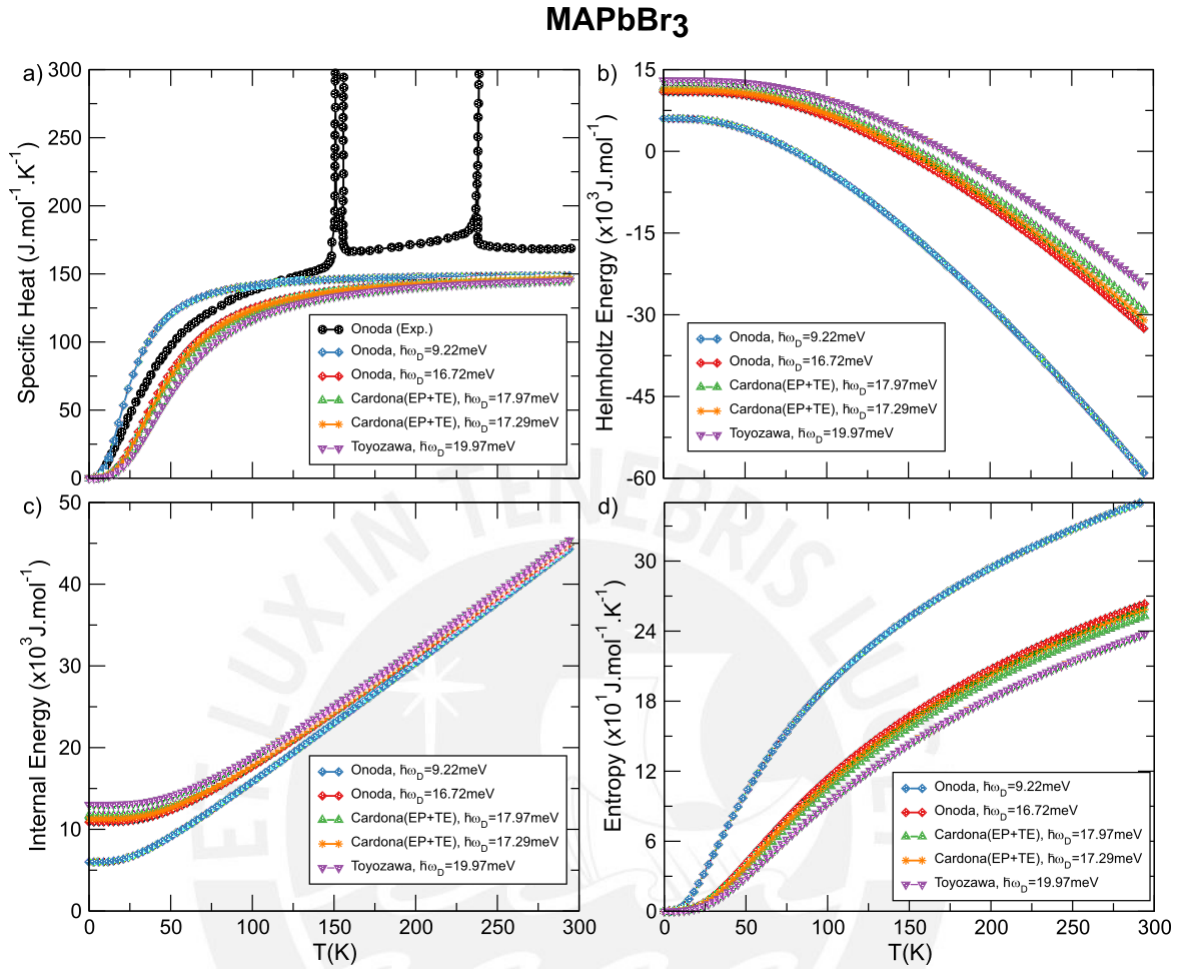
MAPbBr$_3$

Fig. 4.9 Thermodynamic quantities of MAPbBr$_3$. Specific heat (C_v), Helmholtz Energy (F), Internal Energy (U) and Entropy (S) are shown in figures a, b, c and d, respectively. In these figures, the set of points colored as green, orange and purple correspond to the Debye energy, of 17.97 meV, 17.29 meV and 19.97 meV, respectively (see table 4.6). In addition, the blue and red lines show the curves generated with the values obtained by Onoda et al. [92]. Lastly, in figure a, the experimental measurement of specific heat is presented in black. Here, the peaks represent the abrupt increase of energy as product of the phase transition of the perovskite system

Figures 4.11a, b, c, and d depict the specific heat, Helmholtz energy, internal energy, and entropy for MAPbI$_{3-x}$Cl$_x$, respectively. The LO phonon energies of the green, orange, and purple lines were derived from the thermal evolution of the bandgap and FWHM presented in table 4.6. Similar to other tri-halide perovskites, we report the two values of the Debye energy obtained by Onoda et al., i.e., 8.77 meV and 13.56 meV. These values give rise to the blue and red curves observed in figures 4.11a, b, c and d. In figure 4.11a, we report as well the experimental data of the stoichiometrical corners of MAPbI$_{3-x}$Cl$_x$. These corresponds
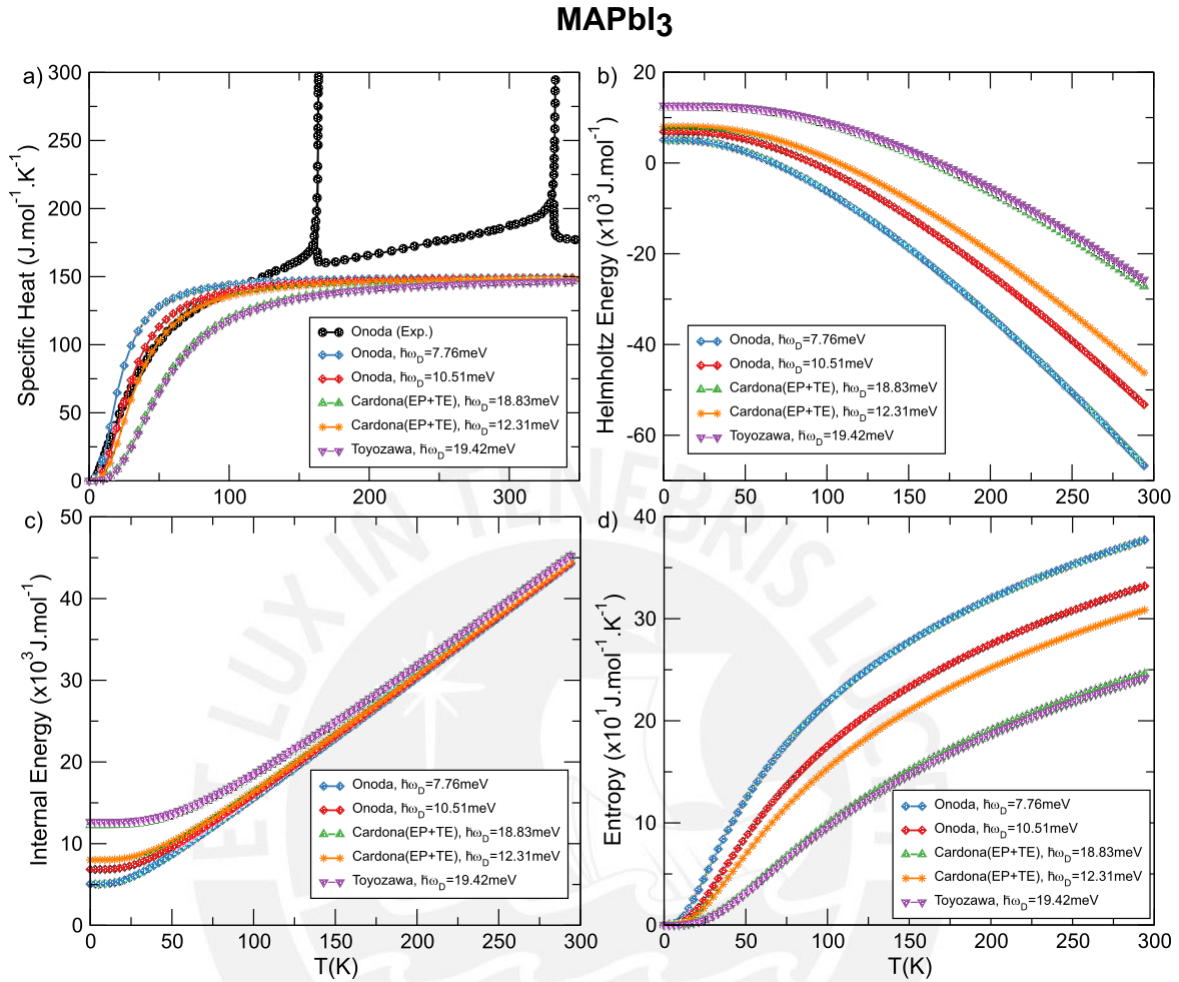
MAPbI$_3$

Fig. 4.10 Thermodynamic quantities of MAPbI$_3$. Specific heat (C_v), Helmholtz Energy (F), Internal Energy (U) and Entropy (S) are shown in figures a, b, c and d, respectively. In these figures, the set of points colored as green, orange and purple correspond to the Debye energy, of 18.83 meV, 12.31 meV and 19.42 meV, respectively (see table 4.6). In addition, the blue and red lines show the curves generated with the values obtained by Onoda et al. [92]. Lastly, in figure a, the experimental measurement of specific heat is presented in black. Here, the peaks represent the abrupt increase of energy as product of the phase transition of the perovskite system

to, the previously shown, MAPbI$_3$ in black colored lines, and MAPbCl$_3$ in pink color. We expect that the specific heat of the mixed material lie within the curves of iodide and chloride based perovskites. From figure 4.11a, we can also infer that the behavior of the Debye energy of 13.56 meV and 18.21 meV are the closest to the MAPbI$_3$ and MAPbCl$_3$ behavior, respectively. In addition, the values retrieved with the Cardona's model of the bandgap seems to shape MAPbCl$_3$ as well. The minor discrepancy can be attributed to our simplistic consideration of the Debye model for the specific heat [92]. Figure 4.11b, c and d show that
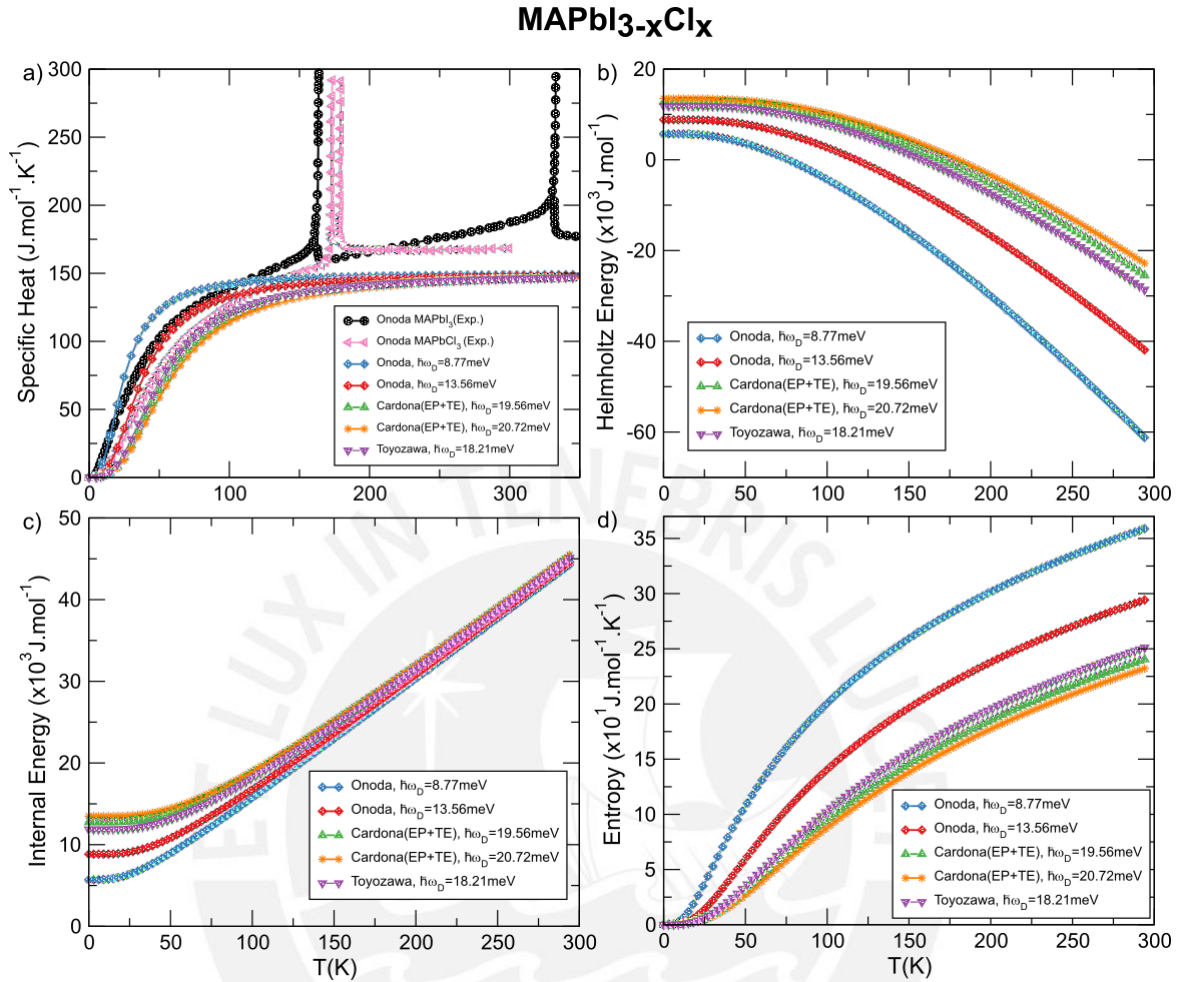
MAPbI$_{3-x}$Cl$_x$

Fig. 4.11 Thermodynamic quantities of MAPbI$_{3-x}$Cl$_x$. Specific heat (C_v), Helmholtz Energy (F), Internal Energy (U) and Entropy (S) are shown in figures a, b, c and d, respectively. In these figures, the set of points colored as green, orange and purple correspond to the Debye energy, of 19.56 meV, 20.72 meV and 18.21 meV, respectively (see table 4.6). In addition, the blue and red lines show the curves generated with the values obtained by Onoda et al. [92]. Lastly, in figure a, the experimental measurements of specific heat for the MAPbI$_3$ and MAPbCl$_3$ are presented in black and pink lines.

the Helmholtz energy, internal energy, and entropy curves obtained from the models follow a similar trend of other tri-halide perovskites.

Chapter 5

Conclusions

In chapter 2, I have presented a review of the models developed for the accurate description of different regions of the absorption coefficient of direct, indirect and amorphous semiconductors. An adequate model for describing the fundamental and high absorption regions of direct semiconductors taking into account the Urbach tail was missing. Tauc-Lorentz and Cody-Lorentz models served as inspiration to develop new self consistent models in the present work. After following the procedure of Jellison-Modine, we arrive to our versions of Ullrich-Lorentz (UL), O'Leary-Lorentz (OL), Band-Fluctuations-Lorentz (BFL) and Monolog-Lorentz (ML) for direct and indirect/amorphous semiconductors. Their advantages are the incorporation of the Urbach tail, the smooth transition from fundamental to high absorption, which is a critical feature to not bias the bandgap determination, and the dependency on 5 fitting parameters only. What is more, the BFL model describes direct, indirect and amorphous semiconductors within a theory that arises from the same principles, while the ML model overcomes the difficulties of the BFL by producing an analytic and simple equation, showing good agreement with the best fitted parameters obtained by the BFL models.

These models were tested for direct (MAPI, GaAs, InP), indirect (c-Si, GaP) and amorphous (a-Si) materials with excellent agreement between experiment and models. The here presented analysis has been done by fitting several oscillators for the whole spectra up to a cutoff energy. We have also analyzed the first oscillator describing the fundamental absorption for each model. These results have also been set in the dimensionless framework for comparison purposes. This extended procedure has been helpful for assessing the capabilities of each model to describe properly the fundamental absorption region along with the high absorption part. The values obtained for each model, presented in figures 2.3, 2.4, 2.5, 2.6, 2.9, and tables 2.1, 2.2, 2.3, 2.4, 2.5 and 2.6 are in good agreement with the results found in

the literature. We believe these models will be helpful for experimentalists studying these and other materials.

In chapter 3, I have constructed a new model based on the Elliott equation. In the Elliott model, the Coulomb interaction between electron and hole is included in the electronic transitions, and, as a consequence, excitons are formed. In this way, the absorption is increased by a set of peaks below the bandgap and a more prominent zone above it due to the Sommerfeld enhanced factor. In the frame of this model, a convolution process is used for the contributions regarding the uncertainty of the measurement and the thermal/disorder effects. Different profiles are used to account this broadenings, such as the Lorentzian, Gaussian or the hyperbolic secant [133, 154].

Motivated by the success of the band-fluctuations model developed in [58] for describing the bandgap and Urbach tails in direct, indirect and amorphous semiconductors through the poly-logarithmic function. We have carried out the convolution process by using the potential that accounts for the fluctuations of the bands. Fluctuations arise from several factors such as perturbations of thermodynamic origin, impurities or dislocations of the perfect lattice. Remarkably, this produces an analytical function which is coupled with the Lorentzian contribution in a pseudo Voigt profile, similar as the one developed in [154].

The new Elliott-Band-Fluctuations (EBF) model serves us to analyze several semiconductors, here GaAs and the family of the tri-halide perovskites, $MAPbBr_3$, $MAPbI_3$, and $MAPbI_xCl_{3-x}$, were chosen. The latter due to the well known properties of GaAs, and the current relevance of the tri-halide perovskites family. The fits show a contribution of 99% arising from the band fluctuations. The obtained values of exciton binding energy, bandgap and broadening quantified by the full width at half maximum (FWHM), are in good agreement with other studies on these materials as presented in figures 3.2, 3.3, and tables 3.1, 3.2, 3.3 and 3.4.

Chapter 4 was dedicated to study the thermal evolution of the optical parameters. Here, we proceed to analyze the bandgap evolution to understand the contributions of the thermal expansion and the e-ph interaction. In some cases the former is negative, as in for GaAs. However, materials such as the tri-halide perovskites show a positive value due to the decrease of the bandgap when pressure increases [147]. For tri-halide perovskites, the dominant contribution for the bandgap arises from thermal expansion expressed as linear behaviour [42, 77]. On the other hand, the negative contribution of the electron phonon interaction, which is proportional to the Bose-Einstein distribution, predominates in the bandgap evolution for GaAs. The independent fits, adapted from the models of Varshni and Cardona, accurately predict the Debye energy and thermal expansion coefficient for GaAs and tri-halide pervoskites, respectively. These are presented in figure 4.1 and tables

4.1 and 4.2. Note that in the case of perovskites, despite the large errors obtained with Cardona's model, the results are comparable with the LO phonon energy retrieved by the thermal evolution of the full width half maximum.
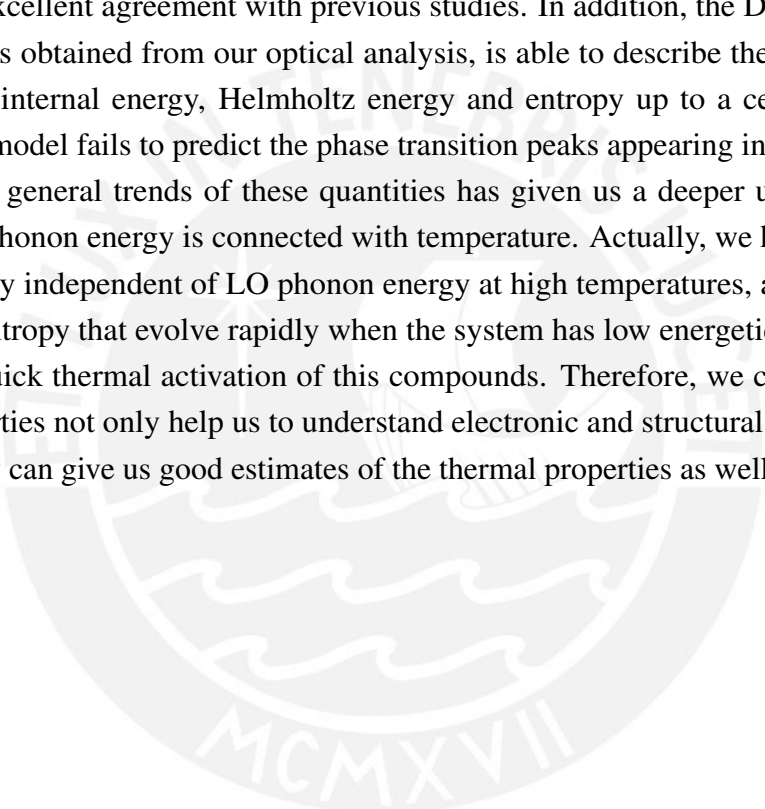
The thermal evolution of the FWHM was fitted by using the broadening evolution proposed by Toyozawa and Segall. Here the electron-phonon interaction is divided in the contributions arising from acoustic and optical phonons. The former produces a linear term, while the latter build a factor proportional to the boson occupation number. Based on previous studies [131, 195], we have considered only the LO phonon contribution for our materials. These produce the determination of the LO phonon energy for the tri-halide perovskites as shown in figure 4.2 and table 4.3. Additionally, the result of the thermal evolution of the exciton binding energy was in agreement with the theoretical result of the constant binding energy as presented in figure 4.3. Despite these good estimations of the binding energy, the variability of the results found in previous studies (table 4.4) make me wonder about the formation of exciton-polaron systems.

For analyzing the exciton-polaron formation in perovskites, we explore the electron-phonon coupling. In summary, the exciton-polaron can be thought as the Coulomb interaction between the electron polaron and the hole polaron. The study of this system has been described in terms of the Pollmann and Kane model [73, 125]. The result of self-consistent equations has helped us to compute the lowest exciton-polaron binding energy with the help of five parameters, the electron and hole effective masses, the static and high frequency electrical permittivity and the LO phonon energy. The result of this model applied to halide-perovskites led us to a possible explanation of the variability in the experimental reports of the exciton binding energy of these materials, as presented in figure 4.4. In summary, the different couplings of the exciton with the LO phonon branches give rise to the large values of binding energies. For the particular case of the LO phonon energy obtained with the bandgap and the FWHM thermal evolution, we have accurately predicted the binding energy with the EBF model. This suggest that the band-fluctuations approach can work in the weak electron-phonon coupling scenario.

The application of the Kane's model is not restricted to the computation of the binding energy from an initial set of parameters. Instead, we can map surfaces of binding energy if we let the effective band masses of electron and hole to vary. Here, we fix the LO phonon energy with the value obtained from the thermal evolution of the bandgap and the FWHM. The retrieved binding energy surfaces obtained for the family of tri-halide perovskites point towards a good agreement between the theoretical binding energy prediction of Kane's model and the free parameter of the EBF model as seen in figures 4.5, 4.6 and 4.7. Implying that the effective masses can be constrained in a particular set of values. This reaffirms the goodness

of the EBF model. The model does not only predict the fitted parameters such as bandgap, FWHM and binding energy, but it gives us LO energies that are correlated with the nature of the exciton-polaron systems.

In the last part of this thesis we have tested our optical models in the computation of the thermodynamic quantities such as the specific heat, internal energy, Helmholtz free energy and entropy. These are presented in figures 4.8, 4.9, 4.10 and 4.11. This was performed by using the LO phonon information of the thermal evolution within the Debye model. We have obtained the behavior of the specific heat for GaAs and the family of tri-halide perovskites showing an excellent agreement with previous studies. In addition, the Debye model with the parameters obtained from our optical analysis, is able to describe the thermodynamic properties of internal energy, Helmholtz energy and entropy up to a certain point. For instance, the model fails to predict the phase transition peaks appearing in the specific heat. However, the general trends of these quantities has given us a deeper understanding on how the LO phonon energy is connected with temperature. Actually, we have observed an internal energy independent of LO phonon energy at high temperatures, and, a Helmholtz energy and entropy that evolve rapidly when the system has low energetic phonons. Thus, implying a quick thermal activation of this compounds. Therefore, we can conclude that optical properties not only help us to understand electronic and structural properties of the solid, but they can give us good estimates of the thermal properties as well.

References

[1] Almog, I. F. (Accessed: 10-01-2022). Available at MIT ocw note sheets.

[2] Asadpour, R. et al. (2015). Bifacial si heterojunction-perovskite organic-inorganic tandem to produce highly efficient ($\eta_T^* \sim 33\%$) solar cell. *Appl. Phys. Lett.*, 106:243902. doi.org/10.1063/1.4922375.

[3] Aspnes, D. E. et al. (1983). Dielectric functions and optical parameters of si, ge, gap, gaas, gasb, inp, inas, and insb from 1.5 to 6.0 ev. *Phys. Rev. B*, 27:985–1009. doi.org/10.1103/PhysRevB.27.985.

[4] Ball, J. and Petrozza, A. (2016). Defects in perovskite-halides and their effects in solar cells. *Nat. Energy*, 1:16149. doi.org/10.1038/nenergy.2016.149.

[5] Bandura, A. V. et al. (2015). Application of zone-folding approach to the first-principles estimation of thermodynamic properties of carbon and zrs2-based nanotubes. *J. of Computational Chemistry*, 37:641–652. doi.org/10.1002/jcc.24243.

[6] Baranowski, M. et al. (2020). Excitons in metal-halide perovskites. *Advanced Energy Materials*, 10:1903659. doi.org/10.1002/aenm.201903659.

[7] Beaudoin, M. et al. (1997). Optical absorption edge of semi-insulating gaas and inp at high temperatures. *Appl. Phys. Lett.*, 70:3540. doi.org/10.1063/1.119226.

[8] Bhosale, J. et al. (2012). Temperature dependence of band gaps in semiconductors: Electron-phonon interaction. *Phys. Rev. B*, 86:195208. doi.org/10.1103/PhysRevB.86.195208.

[9] Bickermann, M. et al. (2010). Uv transparent single-crystalline bulk aln substrates. *Phys. Status Solidi C*, 7:21–24. doi.org/10.1002/pssc.200982601.

[10] Biernacki, S. et al. (1994). Temperature dependence of optical transitions between electronic energy levels in semiconductors. *Phys. Rev. B*, 49:4501. doi.org/10.1103/physrevb.49.4501.

[11] Blakemore, J. S. (1982). Semiconducting and other major properties of gallium arsenide. *J. Appl. Phys.*, 53:R123. doi.org/10.1063/1.331665.

[12] Bludau, W. et al. (1974). Temperature dependence of the band gap of silicon. *J. Appl. Phys.*, 45:1846. doi.org/10.1063/1.1663501.

[13] Bohn, B. J. et al. (2018). Dephasing and quantum beating of excitons in methylammonium lead iodide perovskite nanoplatelets. *ACS photonics*, 5:648–654. doi.org/10.1021/acsphotonics.7b01292.

[14] Bokdam, M. et al. (2016). Role of polar phonons in the photo excited state of metal halide perovskites. *Sci Rep*, 6:28618. doi.org/10.1038/srep28618.

[15] Brivio, F. et al. (2015). Lattice dynamics and vibrational spectra of the orthorhombic, tetragonald, and cubic phases of methylammonium lead iodide. *Phys. Rev. B*, 92:144308. doi.org/10.1103/PhysRevB.92.144308.

[16] Campi, D. et al. (1988). Prediction of optical properties of amorphous tetrahedrally bonded materials. *Journal of Applied Physics*, 64:4128–4134. doi.org/10.1063/1.341323.

[17] Cardona, M. (2005). Electron-phonon interaction in tetrahedral semiconductors. *Solid State Communications*, 133:3–18. doi.org/10.1016/j.ssc.2004.10.028.

[18] Cattelan, M. et al. (2021). Site-specific symmetry sensitivity of angle-resolved photoemission spectroscopy in layered palladium diselenide. *2D Materials*, 8. doi.org/10.1088/2053-1583/AC255A.

[19] Chu, J. et al. (2004). *Semiconductors. Subvolume C. New Data Updates for III-IV, II-VI and I-VII compounds*, volume 44. Springer. Chapter 11.

[20] Cody, G. D. (1992). Urbach edge of crystalline and amorphous silicon: a personal review. *J. of Non-Crystalline Solids*, 141:3–15. doi.org/10.1016/S0022-3093(05)80513-7.

[21] Cody, G. D. et al. (1981). Disorder and the optical-absorption edge of hydrogenated amorphous silicon. *Phys. Rev. Lett.*, 47:1480–1483. doi.org/10.1103/PhysRevLett.47.1480.

[22] Das, S. et al. (2019). Calculation of the band structure, carrier effective mass, and the optical absorption properties of gasbbi alloys. *J. Appl. Phys.*, 125:075705. doi.org/10.1063/1.5065573.

[23] Davydov, A. S. (1973). The theory of contraction of proteins under their excitation. *J. Theoretical Biology*, 38:559–569. doi.org/10.1016/0022-5193(73)90256-7.

[24] Devreese, J. T. (2000). Polarons. doi.org/10.48550/ARXIV.COND-MAT/0004497.

[25] Diab, H. et al. (2016). Narrow linewidth excitonic emission in organic-inorganic lead iodide perovskite single crystals. *The Journal of Phys. Chem. Lett.*, 7:5093–5100. doi.org/10.1021/acs.jpclett.6b02261.

[26] D'Innocenzo, V. et al. (2014). Excitons versus free charges in organo-lead tri-halide perovskites. *Nature Communications*, 5:3586. doi.org/10.1038/ncomms4586.

[27] Dove, M. (2003). *Structure and Dynamics: An Atomic View of Materials*. Oxford Master Series in Condensed Matter Physics 1. OUP Oxford.

[28] Drake, G. W. (Accessed 03.02.2023). Entropy, encyclopedia britannica. Available at https://www.britannica.com/science/entropy-physics. (Accessed 3 February 2023).

[29] Dresselhaus, M. et al. (2018). *Solid State Properties: From Bulk to Nano*. Graduate Texts in Physics. Springer Berlin Heidelberg.

[30] Dubey, S. et al. (2016). Frohlich interaction in compound semiconductors: A comparative study. *Adv. Mat. Res.*, 1141:44–50. doi.org/10.4028/www.scientific.net/amr.1141.44.

[31] Dunstan, D. J. (1983). New evidence for a fluctuating band-gap in amorphous semiconductors. *Journal of Physics C: Solid State Physics*, 16:L567. doi.org/10.1088/0022-3719/16/17/004.

[32] Elliott, R. J. (1957). Intensity of optical absorption by excitons. *Physical Review*, 108:1384–1389. doi.org/10.1103/PhysRev.108.1384.

[33] Even, J. et al. (2014). Analysis of multivalley and multibandgap absorption and enhancement of free carriers related to exciton screening in hybrid perovskites. *Journal of Physical Chemistry C, American Chemical Society*, 118:11566–11572. doi.org/10.1021/jp503337a.

[34] Falsini, N. et al. (2022). Analysis of the urbach tail in cesium lead halide perovskites. *J. Appl. Phys.*, 131:010902. doi.org/10.1063/5.0076712.

[35] Fang, H.-H. et al. (2015). Photophysics of organic–inorganic hybrid lead iodide perovskite single crystals. *Adv. Funct. Mater.*, 25:2378–2385. doi.org/10.1002/adfm.201404421.

[36] Fehrenbach, G. et al. (1985). Excitonic versus plasma screening in highly excited gallium arsenide. *Journal of Luminescence*, 30:154–161. doi.org/10.1016/0022-2313(85)90049-3.

[37] Ferlauto, A. S. et al. (2002). Analytical model for the optical functions of amorphous semiconductors from the near-infrared to ultraviolet: Applications in thin film photovoltaics. *J. Appl. Phys.*, 92:2424–36. doi.org/10.1063/1.1497462.

[38] Forouhi, A. R. et al. (1986). Optical dispersion relations for amorphous semiconductors and amorphous dielectrics. *Physical Review B*, 34:7018–7026. doi.org/10.1103/PhysRevB.34.7018.

[39] Fox, A. (2001). *Optical Properties of Solids*. Oxford master series in condensed matter physics. Oxford University Press.

[40] Franchini, C. et al. (2021). Polarons in materials. *Nature Reviews Materials*, 6:560–586. doi.org/10.1038/s41578-021-00289-w.

[41] Francisco-Lopes, A. et al. (2018). Pressure-induced locking of methylammonium cations versus amorphization in hybrid lead iodide pervoskite. *J. Phys. Chem. C*, 122:2207322082. doi.org/10.1021/acs.jpcc.8b05188.

[42] Francisco-Lopes, A. et al. (2019). Equal footing of thermal expansion and electron-phonon interaction in the temperature dependence of lead halide perovskite band gaps. *J. Phys. Chem. Lett.*, 10:2971–2977. doi.org/10.1021/acs.jpclett.9b00876.

[43] Franta, D. et al. (2013). Application of sum rule to the dispersion model of hydrogenated amorphous silicon. *Thin Solid Films*, 539:233–244. doi.org/10.1016/j.tsf.2013.04.012.

[44] Franta, D. et al. (2017). Dispersion models describing interband electronic transitions combining tauc's law and lorentz model. *Thin Solid Films*, 631:12–22. doi.org/10.1016/j.tsf.2017.03.051.

[45] Frenkel, J. (1931). On the transformation of light into heat in solids. i. *Physical Review.*, 31:17–44. doi.org/10.1103/PhysRev.37.17.

[46] Frohlich, H. (1954). Electrons in lattice fields. *Advances in Physics*, 3:325–361. doi.org/10.1080/00018735400101213.

[47] Frost, J. M. et al. (2017). Slow cooling of hot polarons in halide perovskite solar cells. *ACS Energy Lett.*, 2:2647. doi.org/10.1021/acsenergylett.7b00862.

[48] Fujiwara, H. (2003). *Spectroscopic Ellipsometry Principles and Applications*. Maruzen Co. Ltd, Tokyo, Japan.

[49] Galkowski, K. et al. (2016). Determination of the exciton binding energy and effective masses for methylammonium and formamidinium lead tri-halide perovskite semiconductors. *Energy Environ. Sci.*, 9:962–970. doi.org/10.1039/C5EE03435C.

[50] Gobel, A. et al. (1998). Effects of the isotopic composition on the fundametal gap of cucl. *Phys. Rev. B*, 57:15183–15190. doi.org/10.1103/PhysRevB.57.15183.

[51] Gold-Parker, A. et al. (2018). Acoustic phonon lifetimes limit thermal transport in methylammonium lead iodide. *Proceedings of the National Academy of Sciences*, 115. doi.org/10.1073/pnas.1812227115.

[52] Gopal, A. V. et al. (2000). Photoluminescence study of exciton–optical phonon scattering in bulk gaas and gaas quantum wells. *J. Appl. Phys.*, 87:1858–1862. doi.org/10.1063/1.372104.

[53] Gopalan, S. et al. (1987). Temperature dependence of the shifts and broadening of the critical points in gaas. *Phys. Rev. B*, 35:5577–5584. doi.org/10.1103/PhysRevB.35.5577.

[54] Green, M. A. et al. (2015). Optical properties of photovoltaic organic–inorganic lead halide perovskites. *J. Phys. Chem. Lett.*, 6:4774–4785. doi.org/10.1021/acs.jpclett.5b01865.

[55] Guerra, J. A. et al. (2003). Excitonic solar cells. *J. Phys. Chem. B*, 107:4688–4698. doi.org/10.1021/jp022507x.

[56] Guerra, J. A. et al. (2016). The urbach focus and optical properties of amorphous hydrogenated sic thin films. *J. Phys. D: Appl. Phys.*, 49:195102. doi.org/10.1088/0022-3727/49/19/195102.

[57] Guerra, J. A. et al. (2017). Determination of the complex refractive index and optical bandgap of ch3nh3pbi3 thin films. *J. Appl. Phys.*, 121:173104. doi.org/10.1063/1.4982894.

[58] Guerra, J. A. et al. (2019). Band-fluctuations model for the fundamental absorption of crystalline and amorphous semiconductors: a dimensionless joint density of states analysis. *J. Phys. D: Appl. Phys.*, 52:105303. doi.org/10.1088/1361-6463/aaf963.

[59] Guha, S., Yang, J., and Yan, B. (2016). *Reference Module in Materials Science and Materials Engineering. Chapter: Amorphous and Nanocrystalline Silicon Solar Cells and Modules.* Elsevier. doi.org/10.1016/B978-0-12-803581-8.00835-3.

[60] Haken, H. (1956). Kopplung nichtrelativistischer teilchen mit einem quantisierten feld. *II Nuovo Cimento (1955-1965)*, 3:1230–1253. doi.org/10.1007/BF02785005.

[61] Haken, H. (1986). *Festkörperprobleme 26. Chapter: Excitons and the electronic polarization in semiconductors.* Springer Berlin Heidelberg, Berlin, Heidelberg. doi.org/10.1007/BFb0107791.

[62] Hennel, A. M. (1971). Temperature dependence of the energy gap in gaas. *Physica Status Solidi A*, 8:K111–K113. doi.org/10.1002/pssa.2210080244.

[63] Herzinger, C. M. et al. (1995). Inp optical constants between 0.75 and 5.0 ev determined by variable-angle spectroscopic ellipsometry. *J. Appl. Phys.*, 77:1715.

[64] Hirasawa, M. et al. (1994). Magnetoabsorption of the lowest exciton in perovskite-type compound (ch3nh3)pbi3. *Physica B: Condensed Matter*, 201:427–430. doi.org/10.1016/0921-4526(94)91130-4.

[65] Ibach, H. and Lüth, H. (2009). *Solid-State Physics: An Introduction to Principles of Materials Science.* Springer Berlin, Heidelberg. doi.org/10.1007/978-3-540-93804-0.

[66] Ishihara, T. (1994). Optical properties of pbi-based perovskite structures. *Journal of Luminescence*, 60-61:269–274. doi.org/10.1016/0022-2313(94)90145-7.

[67] Jackson., W. B. et al. (1985). Energy dependence of the optical matrix element in hydrogenated amorphous and crystalline silicon. *Phys. Rev. B*, 31:5187–5198. doi.org/10.1103/PhysRevB.31.5187.

[68] Jagadish, C. and Pearton, S. (2006). *Zinc Oxide Bulk, Thin Films and Nanostructures. Chapter: Foreword.* Elsevier Science Ltd. doi.org/10.1016/B978-008044722-3/50000-2.

[69] Jellison, G. E. et al. (1996). Parameterization of the optical functions of amorphous materials in the interband region. *Applied Physics Letters*, 69:371. doi.org/10.1063/1.118064.

[70] Jena, A. et al. (2019). doi.org/10.48550/ARXIV.1908.02433.

[71] Jiang, Y. et al. (2019). Properties of excitons and photogenerated charge carriers in metal halide perovskites. *Advanced Materials*, 31:1806671. doi.org/10.1002/adma.201806671.

[72] Johnson, S. R. et al. (1995). Temperature dependence of the urbach edge in gaas. *J. Appl. Phys.*, 78:5609. doi.org/10.1063/1.359683.

[73] Kane, E. O. (1978). Pollmann-buttner variational method for excitonic polarons. *Phys. Rev. B*, 18:6849. doi.org/10.1103/PhysRevB.18.6849.

[74] Kearns, J. K. (2019). *Single Crystals of Electronic Materials. Chapter: Silicon single crystals.* Woodhead Publishing Series in Electronic and Optical Materials. Woodhead Publishing. doi.org/10.1016/B978-0-08-102096-8.00002-1.

[75] Kittel, C. (1987). *Quantum Theory of Solids*. Wiley.

[76] Kittel, C. (2005). *Introduction to Solid State Physics*. John Wiley & Sons, Inc, 8th edition edition.

[77] Kong, L. et al. (2016). Simultaneous band-gap narrowing and carrier-lifetime prolongation of organic-inorganic trihalide perovskites. *PNAS*, 113:8910–8915. doi.org/10.1073/pnas.160903011.

[78] Koutselas, I. B. et al. (1996). Electronic properties of three- and low-dimensional semiconducting materials with pb halide and sn halide units. *J. Phys: Condens. Matter*, 8:1217. doi.org/10.1088/0953-8984/8/9/012.

[79] Kunugita, H. et al. (2016). Exciton–exciton scattering in perovskite ch_3nh_3 $pbbr_3$ single crystal. *Jpn. J. Appl. Phys.*, 55:060304. doi.org/10.7567/JJAP.55.060304.

[80] Kuper, C. G. and Whitfield, G. D. (1963). *Y. Toyozawa in 'Polarons and Excitons'*. Edinburgh: Oliver and Boyd, p. 211-232. https://www.worldcat.org/es/title/123784002.

[81] Lautenschlager, P. et al. (1985). Temperature dependence of band gaps in si and ge. *Phys. Rev. B*, 31:2163–2171. doi.org/10.1103/PhysRevB.31.2163.

[82] Lawler, H. M. et al. (2004). Anharmonic effects on infrared spectra of gaas and gap: First-principles calculations. *Phys. Rev. B*, 70:245209. doi.org/10.1103/PhysRevB.70.245209.

[83] Ledinsky, M. et al. (2019). Temperature dependence of the urbach energy in lead iodide perovskites. *J. Phys. Chem. Lett.*, 10:1368–1373. doi.org/10.1021/acs.jpclett.9b00138.

[84] Lee, T. D. et al. (1953). The motion of slow electrons in a polar crystal. *Physical Review*, 90:297. doi.org/10.1103/PhysRev.90.297.

[85] Leguy, A. M. A. et al. (2016). Dynamic disorder, phonon lifetimes, and the assignment of modes to the vibrational spectra of methylammonium lead halide perovskites. *Phys. Chem. Chem. Phys.*, 18:27051–27066. doi.org/10.1039/C6CP03474H.

[86] Lin, Q. Q. et al. (2015). Electro-optics of perovskite solar cells. *Nature Photon.*, 9:106–112. doi.org/10.1038/nphoton.2014.284.

[87] Liu, X. et al. (2020). *Chalcogenide: From 3D to 2D and Beyond. Chapter 8: Layered two-dimensional selenides and tellurides grown by molecular beam epitaxy*. Woodhead Publishing Series in Electronic and Optical Materials. Woodhead Publishing. doi.org/10.1016/B978-0-08-102687-8.00012-9.

[88] Lizárraga, K., Enrique-Morán, L. A., Tejada, A., Piñeiro, M., Llontop, P., Serquen, E., Perez, E., Korte, L., and Guerra, J. A. (2022). New optical models for the accurate description of the electrical permittivity in direct and indirect semiconductors.

[89] LL, Y. et al. (2006). First-principles calculations for transition phase and thermodynamic properties of gaas. *Chinese Physics.*, 15:802. doi.org/10.1088/1009-1963/15/4/022.

[90] Lorenz, M. R. et al. (1968). Band gap of gallium phosphide from 0 to 900°k and light emission from diodes at high temperatures. *Physical Review*, 171:876. doi.org/10.1103/PhysRev.171.876.

[91] Lourenco, S. et al. (2004). Thermal expansion contribution to the temperature dependence of excitonic transitions in gaas and algaas. *Brazilian Journal of Physics*, 34:517–525. doi.org/10.1590/S0103-97332004000300031.

[92] Luo, B. et al. (1383-1395). Calorimetric and ir spectroscopic studies of phase transitions in methylammonium trihalogenoplumbates (ii). *J. of Physics and Chemistry Solids*, 51:1990. doi.org/10.1016/0022-3697(90)90021-7.

[93] Luo, B. et al. (2014). Electronic structure, elastic and thermal properties of semiconductor gax (x = n, p, as, sb) with zinc blende from first-principles calculation. *Int. J. of Modern Physics B*, 28:1450183. doi.org/10.1142/S0217979214501835.

[94] Löper, P. et al. (2015). Complex refractive index spectra of ch3nh3pbi3 perovskite thin films determined by spectroscopic ellipsometry and spectrophotometry. *J. Phys. Chem. Lett.*, 6:66–71. doi.org/10.1021/jz502471h.

[95] MacFarlane, G. G. et al. (1958). Fine structure in the absorption-edge spectrum of si. *Phys. Rev.*, 111:1245. doi.org/10.1103/PhysRev.111.1245.

[96] Malik, S. M. et al. (2002). Optical transitions in hydrogenated amorphous silicon. *Appl. Phys. Lett.*, 80:790. doi.org/10.1063/1.1445476.

[97] Mannino, G. et al. (2020). Temperature-dependent optical band gap in CsPbBr$_3$, MAPBBr$_3$ and FAPbBr$_3$ single crystals. *J. Phys. Chem. Lett.*, 11:2490–2496. doi.org/10.1021/acs.jpclett.0c00295.

[98] Mariano, F. et al. (2020). The enhancement of excitonic emission crossing saha equilibrium in trap passivated *ch$_3$nh$_3$pbbr$_3$* perovskite. *Commun. Physics*, 3. doi.org/10.1038/s42005-020-0309-3.

[99] Marongiu, D. et al. (2019). The role of excitons in 3d and 2d lead halide perovskites. *J. Materials Chemistry C*, 7:12006–12018. doi.org/10.1039/C9TC04292J.

[100] Menzel, D. et al. (2021). Revisiting the determination of the valence band maximum and defect formation in halide perovskites for solar cells: Insights from highly sensitive near–uv photoemission spectroscopy. *ACS Appl. Mater. Interfaces*, 13:43540–43553. doi.org/10.1021/acsami.1c10171.

[101] Menzel, D. et al. (2022). Field effect passivation in perovskite solar cells by a lif interlayer. *Advanced Energy Materials*, 12:2201109. doi.org/10.1002/aenm.202201109.

[102] Miyata, A. et al. (2015). Direct measurement of the exciton binding energy and effective masses for charge carriers in organic–inorganic tri-halide perovskites. *Nature Phys*, 11:582–587. doi.org/10.1038/nphys3357.

[103] Miyata, K. et al. (2017). Large polarons in lead halide perovskites. *Sci. Adv.*, 3:1701217. doi.org/10.1126/sciadv.1701217.

[104] Murayama, Y. (2001). *Mesoscopic Systems: Fundamentals and Applications*. doi.org/10.1002/9783527618026.app4.

[105] Nam, S. B. et al. (1976). Free-exciton energy spectrum in gaas. *Phys. Rev. B*, 13:761. doi.org/10.1103/PhysRevB.13.761.

[106] Natanzon, Y. et al. (2020). Evaluation of polaron transport in solids from first-principles. *Israel Journal of Chemistry*, 60:768–786. doi.org/10.1002/IJCH.201900101.

[107] Nave, R. (Accessed: 2023-01-25). Thermodynamic potentials. Available at http://hyperphysics.phy-astr.gsu.edu/hbase/thermo/thepot.html.

[108] Niesner, D. et al. (2017). Temperature-dependent optical spectra of single-crystal $(ch_3nh_3)pbbr_3$ cleaved in ultrahigh. *Physical Review B*, 95:075207. doi.org/10.1103/PhysRevB.95.075207.

[109] NNSE618 (Accessed: 26.01.2023). Lecture 15 - absorption. Available at https://www.albany.edu/ soktyabr/NNSE618/.

[110] Novikova, S. I. (1960). *Sov. Phys. Solid State*, 2:37–38.

[111] Novikova, S. I. (1961). *Sov. Phys. Solid State*, 3:129.

[112] NSM (Accessed: 2022-12-03). Semiconductors database. Available at http://www.ioffe.ru/SVA/NSM/Semicond/.

[113] of Chemistry, R. S. (Accessed: 10-02-2023). www.rsc.org/periodic-table/element/14/silicon.

[114] Okada, Y. et al. (1984). Precise determination of lattice parameter and thermal expansion coefficient of silicon between 300 and 1500 k. *J. Appl. Phys.*, 56:314–320. doi.org/10.1063/1.333965.

[115] O'Leary, S. K. et al. (1995a). Optical absorption in amorphous semiconductors. *Phys. Rev. B*, 52:7795. doi.org/10.1103/PhysRevB.52.7795.

[116] O'Leary, S. K. et al. (1995b). Semiclassical density-of-states and optical-absorption analysis of amorphous semiconductors. *Phys. Rev. B*, 51:4143. doi.org/10.1103/PhysRevB.51.4143.

[117] O'Leary, S. K. et al. (2002). A simplified joint density of states analysis of hydrogenated amorphous silicon. *J. Appl. Phys.*, 92:4276. doi.org/10.1063/1.1504174.

[118] Olguín, D. et al. (2002). Electron–phonon effects on the direct band gap in semiconductors: Lcao calculations. *Solid State Comm.*, 122:575–589. doi.org/10.1016/S0038-1098(02)00225-9.

[119] Orapunt, F. et al. (2004). The urbach focus and hydrogenated amorphous silicon. *Appl. Phys. Lett.*, 84:523. doi.org/10.1063/1.1641176.

[120] Ozevin, D. (2014). *Sensor Technologies for Civil Infrastructures. Chapter 10: Micro-electro-mechanical-systems (MEMS) for assessing and monitoring civil infrastructures.* Woodhead Publishing Series in Electronic and Optical Materials. Woodhead Publishing. doi.org/10.1533/9780857099136.265.

[121] Pässler, R. (1997). Basic model relations for temperature dependencies of fundamental energy gaps in semiconductors. *Physica Status Solidi (b)*, 200:155–172. doi.org/10.1002/1521-3951(199703)200:1<155::AID-PSSB155>3.0.CO;2-3.

[122] Pässler, R. (2013). Non-debye heat capacity formula refined and applied to gap, gaas, gasb, inp, inas, and insb. *AIP Advances*, 3:082108.

[123] Perrin, M. (Accessed: 2023-01-30). Polariton. Available at https://en.wikipedia.org/wiki/Polariton#/media/File:Phonon_polaritons.svg.

[124] Phuong, L. Q. et al. (2016). Free excitons and exciton–phonon coupling in $ch_3nh_3pbi_3$ single crystals revealed by photocurrent and photoluminescence measurements at low temperatures. *J. Phys. Chem. Lett.*, 7:4905. doi.org/10.1021/acs.jpclett.6b02432.

[125] Pollmann, J. et al. (1975). Upper bounds for the ground-state energy of the exciton-phonon system. *Solid State Comm.*, 17:1171–1174. doi.org/10.1016/0038-1098(75)90279-3.

[126] Qiang, H. et al. (1992). Size dependence of the thermal broadening of the exciton linewidth in gaas/ga0.7al0.3as single quantum wells. *Appl. Phys. Lett.*, 61:1411. doi.org/10.1063/1.107554.

[127] Rakita, Y. et al. (2015). Mechanical properties of $apbx_3$ (a = cs or ch_3nh_3; x = i or br) perovskite single crystals. *MRS Commun*, 5:623–629. doi.org/10.1557/mrc.2015.69.

[128] Redfield, D. (1963). Effect of defect fields on the optical absorption edge. *Phys. Rev.*, 130:916. doi.org/10.1103/PhysRev.130.916.

[129] Rizwan, Z. et al. (2011). Effect of annealing temperature on the optical spectra of cds thin films deposited at low solution concentrations by chemical bath deposition (cbd) technique. *Int. Journal of Molecular Sciences*, 12:1293–1305. doi.org/10.3390/ijms12021293.

[130] Rodova, M. et al. (2003). Phase transition in ternary caesium lead bromide. *J. Thermal Analysis and Calorimetry*, 71:667673. doi.org/10.1023/A:1022836800820.

[131] Rudin, S. et al. (1990). Temperature-dependent exciton linewidths in semiconductors. *Phys. Rev. B*, 42:11218–11231. doi.org/10.1103/PhysRevB.42.11218.

[132] Ruf, F. et al. (2019). Temperature-dependent studies of exciton binding energy and phase-transition suppression in (cs,fa,ma)pb(i,br)$_3$ perovskites. *APL Mater*, 7:031113. doi.org/10.1063/1.5083792.

[133] Saba, M. et al. (2014). Correlated electron–hole plasma in organometal perovskites. *Nat Commun*, 5:5049. doi.org/10.1038/ncomms6049.

[134] Saba, M. et al. (2015). Excited state properties of hybrid perovskites. *Sci. Rep.*, 49:166–173. doi.org/10.1021/acs.accounts.5b00445.

[135] Sajeev, J. et al. (1986). Theory of electron band tails and the urbach optical-absorption edge. *Appl. Phys. Lett.*, 57:1777. doi.org/10.1103/PhysRevLett.57.1777.

[136] Saran, R. et al. (2017). Giant bandgap renormalization and exciton–phonon scattering in perovskite nanocrystals. *Adv. Optical Mater.*, 5:1700231.

[137] Schueller, E. C. et al. (2018). Crystal structure evolution and notable thermal expansion in hybrid perovskites formamidinium tin iodide and formamidinium lead bromide. *Inorg. Chem*, 57:695701. doi.org/10.1021/acs.inorgchem.7b02576.

[138] Scirè, D. et al. (2022). Erratum to: Sub-gap defect density characterization of molybdenum oxide: An annealing study for solar cell applications. *Nano Research*, 15:7752–7753. doi.org/10.1007/s12274-022-4222-9.

[139] Segall, B. et al. (1968). Phonon-assisted recombination of free excitons in compound semiconductors. *Phys. Rev.*, 171:935–948. doi.org/10.1103/PhysRev.171.935.

[140] Seisyan, R. P. (1993). Exciton-polariton resonances in light absorption spectra of semiconductor superlattices and crystals. *Proc. SPIE*. doi.org/10.1117/12.162811.

[141] Sell, D. D. et al. (1644-1647). Observation of polaritons in gaas: A new interpretation of the free-exciton reflectance and luminescence. *Phys. Rev. Lett.*, 27:311–314. doi.org/10.1103/PhysRevLett.27.1644.

[142] Sell, D. D. et al. (1971). New analysis of direct exciton transitions: Application to gap. *Phys. Rev. Lett.*, 26:311–314. doi.org/10.1103/PhysRevLett.26.311.

[143] Sendner, M. et al. (2016). Optical phonons in methylammonium lead halide perovskites and implications for charge transport. *Material Horizons*, 3:613–620. doi.org/10.1039/C6MH00275G.

[144] Serrano, J. et al. (2002). Electron-phonon renormalization of the absorption edge of the cuprous halides. *Phys. Rev. B*, 65:125110. doi.org/10.1103/PhysRevB.65.125110.

[145] Sestu, N. et al. (2015a). Absorption f-sum rule for the exciton binding energy in methylammonium lead halide perovskites. *J. Phys. Chem. Lett.*, 6:4566–4572. doi.org/10.1021/acs.jpclett.5b02099.

[146] Sestu, N. et al. (2015b). Supplementary information. *J. Phys. Chem. Lett.* doi.org/10.1021/acs.jpclett.5b02099.

[147] Shakir, F. et al. (2012). Electronic structure of gallium arsenide under pressure. *Atti Della Fondazione Giorgio Ronchi Anno LXVII N.2, Google*.

[148] Shinada, M. et al. (1966). Interband optical transitions in extremely anisotropic semiconductors. i. bound and unbound exciton absorption. *J. Phys. Soc. Jpn.*, 21:1936–1946. doi.org/10.1143/JPSJ.21.1936.

[149] Shindo, K. (1970). Effective electron-hole interaction in shallow excitons. *J. Phys. Soc. Jpn.*, 29:287–296. doi.org/10.1143/JPSJ.29.287.

[150] Shirayama, M. et al. (2016). Optical transitions in hybrid perovskite solar cells: Ellipsometry, density functional theory, and quantum efficiency analyses for ch3nh3pbi3. *Phys. Rev. Applied*, 5:014012. doi.org/10.1103/PhysRevApplied.5.014012.

[151] Singh, J. (1994). Polarons and excitonic polarons. *Excitation Energy Transfer Processes in Condensed Matter*, pages 69–110. doi.org/10.1007/978-1-4899-0996-1.

[152] Singh, J. and Shimakawa, K. (2003). *Advances in Amorphous Semiconductors*. London: Taylor and Francis. doi.org/10.1201/9780367801083.

[153] Slaoui, A. and Collins, R. T. (2016). *Photovoltaics: Advanced Inorganic Materials*. Elsevier. doi.org/10.1016/B978-0-12-803581-8.02728-4.

[154] Soufiani, A. M. et al. (2015a). Polaronic exciton binding energy in iodide and bromide organic-inorganic lead halide pervoskites. *Appl. Phys. Lett*, 107:231902. doi.org/10.1063/1.4936418.

[155] Soufiani, A. M. et al. (2015b). Supplementary information. *Appl. Phys. Lett*. http://dx.doi.org/10.1063/1.4936418.

[156] S.Sun et al. (2014). The origin of high efficiency in low-temperature solution-processable bilayer organometal halide hybrid solar cells. *Energy Environ. Sci.*, 7:399–407. doi.org/10.1039/C3EE43161D.

[157] Studenyak, I. et al. (2014). Urbach rule in solid state physics. *International Journal of Optics and Applications*, 4:76–83. doi.org/10.5923/j.optics.20140403.02.

[158] Sturge, M. D. (1963). Optical absorption of gallium arsenide between 0.6 and 2.75 ev. *Phys. Rev.*, 129:2835.

[159] Subedi, I. et al. (2017). Optical properties of inp from infrared to vacuum ultraviolet studied by spectroscopic ellipsometry. *Appl. Surf. Sci.*, 421:813–818. doi.org/10.1016/j.apsusc.2017.01.027.

[160] Sun, S. et al. (2015). Mechanical properties of organicinorganic halide perovskites, $ch_3nh_3pbx_3$ (x = i, br and cl), by nanoindentation. *J. Mater. Chem.*, 3:1845018455. doi.org/10.1039/C5TA03331D.

[161] Sun, S. et al. (2017). Factors influencing the mechanical properties of formamidinium lead halides and related hybrid perovskites. *Chem. ChemSusChem*, 10:3740. doi.org/10.1002/cssc.201700991.

[162] Sveinbjörnsson, K. et al. (2022). Monolithic perovskite/silicon tandem solar cell with 28.7% efficiency using industrial silicon bottom cells. *ACS Energy Lett.*, 7:2654–2656. doi.org/10.1021/acsenergylett.2c01358.

[163] Tan, W. et al. (2017). Ordered and disordered phases in mo1xwxs2 monolayer. *Scientific Reports*, 7:15124. doi.org/10.1038/s41598-017-15286-9.

[164] Tanaka, K. et al. (2003). Comparative study on the excitons in lead-halide-based perovskite-type crystals ch3nh3pbbr3 ch3nh3pbi3. *Solid State Communications*, 127:619–623. doi.org/10.1016/S0038-1098(03)00566-0.

[165] Tauc, J. (1968). Optical properties and electronic structure of amorphous ge and si. *Mater. Res. Bull.*, 3:37. doi.org/10.1016/0025-5408(68)90023-8.

[166] Tejada, A. et al. (2018). Optical characterization and bandgap engineering of flat and wrinkle-textured fa0.83cs0.17pb(i1–xbrx)3 perovskite thin films. *J. Appl. Phys.*, 123:175302. doi.org/10.1063/1.5025728.

[167] Thevaril, J. J. et al. (2010). A dimensionless joint density of states formalism for the quantitative characterization of the optical response of hydrogenated amorphous silicon. *J. Appl. Phys.*, 107:083105. doi.org/10.1063/1.3385434.

[168] Thevaril, J. J. et al. (2016). A universal feature in the optical absorption spectrum associated with hydrogenated amorphous silicon: A dimensionless joint density of states analysis. *J. Appl. Phys.*, 120:135706. doi.org/10.1063/1.4963122.

[169] Tilchin, J. et al. (2016). Hydrogen-like wannier–mott excitons in single crystal of methylammonium lead bromide perovskite. *ACS Nano*, 10:6363–6371. doi.org/10.1021/acsnano.6b02734.

[170] Toyozawa, Y. (1958). Theory of line-shapes of the exciton absorption bands. *Progress of Theoretical Physics*, 20:53–81. doi.org/10.1143/PTP.20.53.

[171] Toyozawa, Y. (1964). Interband effect of lattice vibrations in the exciton absorption spectra. *J. Phys. Chem. Solids*, 25:59–71. doi.org/10.1016/0022-3697(64)90162-3.

[172] UCDAVIS (Accessed: 2022-12-30). Woodall research lab. Available at https://woodall.ece.ucdavis.edu/resources/.

[173] Ueta, M. (1986). *Excitonic Processes in Solids*. Springer Berlin Heidelberg, Springer Berlin Heidelberg. doi.org/10.1007/978-3-642-82602-3.

[174] Ugur, E. et al. (2022). The long-wavelength edge of photographic sensitivity and of the electronic absorption of solids. *J. Phys. Chem. Lett.*, 13:7702–7711. doi.org/10.1021/acs.jpclett.2c01812.

[175] Ullrich, B. et al. (1991). Bistable optical thin cds film devices: All-optical and optoelectronic features. *Jpn. J. Appl. Phys.*, 30:L1285. doi.org/10.1143/JJAP.30.L1285.

[176] Ullrich, B. et al. (2003). Analysis of single- and two-photon-excited green emission spectra of thin-film cadmium sulfide. *J. Appl. Phys.*, 93:1914. doi.org/10.1063/1.1537459.

[177] Ullrich, B. et al. (2007). Photoluminescence analysis of p-doped gaas using the roosbroeck–shockley relation. *Semicond. Sci. Technol.*, 22:1174. doi.org/10.1088/0268-1242/22/10/016.

[178] Urbach, F. (1953). The long-wavelength edge of photographic sensitivity and of the electronic absorption of solids. *Phys. Rev.*, 92:1324. doi.org/10.1103/PhysRev.92.1324.

[179] Varshni, Y. (1967). Temperature dependence of the energy gap in semiconductors. *Physica*, 34:149–154. doi.org/10.1016/0031-8914(67)90062-6.

[180] Vasudevan, R. et al. (2016). A thin-film silicon/silicon hetero-junction hybrid solar cell for photoelectrochemical water-reduction applications. *Solar Energy Materials Solar Cells*, 150:82–87. doi.org/10.1016/j.solmat.2016.02.006.

[181] Ventura, E. E. (2022). *La relación intrínseca entre la descripción del ancho de banda y las propiedades térmicas en semiconductores : el caso del a-Si:H E In2O3*. PhD thesis, Pontificia Universidad Catolica del Peru (PUCP). http://hdl.handle.net/20.500.12404/22735.

[182] Viña, L. et al. (1984). Temperature dependence of the dielectric function of germanium. *Phys. Rev. B*, 30:1979. doi.org/10.1103/PhysRevB.30.1979.

[183] Václavík, J. et al. (2013). *EPJ Web of Conferences*, 48:00028. doi.org/10.1051/epjconf/20134800028.

[184] WaferWorld. (Accessed: 23.08.2022). What is indium phosphide? Available at https://www.waferworld.com/post/what-is-indium-phosphide-2 (Accessed: 23.08.2022).

[185] Wallace, D. (1998). *Thermodynamics of Crystals*. Dover books on physics. Dover Publications.

[186] Wang, L. et al. (2016). Pressure-induced structural and optical properties of organometal halide perovskite-based formamidinium lead bromide. *J. Phys. Chem. Lett.*, 7:25562562. doi.org/10.1021/acs.jpclett.6b00999.

[187] Wang, S. et al. (1974). Wannier exciton in a polarizable field. *Physical Review B*, 10:3330. doi.org/10.1103/PhysRevB.10.3330.

[188] Wang, Y. et al. (2015). Pressure-induced phase transformation, reversible amorphization, and anomalous visible light response in organolead bromide perovskite. *J. Am. Chem. Soc.*, 137:1114411149. doi.org/10.1021/jacs.5b06346.

[189] Wannier, G. H. (1937). The structure of electronic excitation levels in insulating crystals. *Phys. Rev.*, 52:191. doi.org/10.1103/PhysRev.52.191.

[190] Wehrenfennig, C. et al. (2014). Homogeneous emission line broadening in the organo lead halide perovskite $ch_3nh_3pbi_{3x}cl_x$. *Phys. Chem. Lett.*, 5:1300–1306.

[191] Wei, K. et al. (2016). Temperature-dependent excitonic photoluminescence excited by two-photon absorption in perovskite CsPbBr$_3$ quantum dots. *Optics Letters*, 41:3821–3824. doi.org/10.1364/OL.41.003821.

[192] Weingärtner, R. et al. (2001). Absorption mapping of doping level distribution in n-type and p-type 4h-sic and 6h-sic. *Materials Science and Engineering: B*, 80:357–361. doi.org/10.1016/S0921-5107(00)00599-7.

[193] Weingärtner, R. et al. (2002). Determination of charge carrier concentration in n- and p-doped sic based on optical absorption measurements. *Applied Physics Letters*, 80:70. doi.org/10.1063/1.1430262.

[194] Wolf, S. D. et al. (2014). Organometallic halide perovskites: Sharp optical absorption edge and its relation to photovoltaic performance. *J. Phys. Chem. Lett.*, 5:1035–1039. doi.org/10.1021/jz500279b.

[195] Wright, A. D. et al. (2016). Electron–phonon coupling in hybrid lead halide perovskites. *Nat. Comm.*, 7:11755. doi.org/10.1038/ncomms11755.

[196] Wu, B. et al. (2016). Discerning the surface and bulk recombination kinetics of organic–inorganic halide perovskite single crystals. *Adv. Energy Mater*, 6:1600551. doi.org/10.1002/aenm.201600551.

[197] Wu, K. W. et al. (2014). Temperature-dependent excitonic photoluminescence of hybrid organometal halide perovskite films. *Phys. Chem. Chem. Phys.*, 16:22476–22481. doi.org/10.1039/C4CP03573A.

[198] Yamada, Y. et al. (2015). Photoelectronic responses in solution-processed perovskite *ch3nh3pbi3* solar cells studied by photoluminescence and photoabsorption spectroscopy. *IEEE J. Photovoltaics*, 5:401. doi.org/10.1109/JPHOTOV.2014.2364115.

[199] Yang, J. et al. (2017). Acoustic-optical phonon up-conversion and hot-phonon bottleneck in lead-halide perovskites. *Nature Communications*, 8:14120. doi.org/10.1038/ncomms14120.

[200] Yang, T. et al. (2023). One-stone-for-two-birds strategy to attain beyond 25% perovskite solar cells. *Nat. Commun.*, 14:839. doi.org/10.1038/s41467-023-36229-1.

[201] Yang, Y. et al. (2015). Comparison of recombination dynamics in *ch3h3pbbr3* and *ch3nh3pbi3* perovskite films: Influence of exciton binding energy. *J. Phys. Chem Lett.*, 23:4688–4692. doi.org/10.1021/acs.jpclett.5b02290.

[202] Yang, Y. et al. (2016). Observation of a hot-phonon bottleneck in lead-iodide perovskites. *Nature Photonics*, 10:53–59. doi.org/10.1103/PhysRev.129.2835.3.

[203] Yu, C. et al. (2011). Temperature dependence of the band gap of perovskite semiconductor compound $CsSnI_3$. *J. Appl. Phys.*, 110:063526. doi.org/10.1063/1.3638699.

[204] Yu, P. and Cardona, M. (2005). *Fundamentals of Semiconductors: Physics and Materials Properties 3rd edn*. Berlin: Springer. doi.org/10.1007/b137661.

[205] Zhang, L. et al. (2017). Pressure-induced structural and optical properties of inorganic halide perovskite *cspbbr3*. *J. Phys. Chem. Lett.*, 8:37523758. doi.org/10.1021/acs.jpclett.7b01577.

[206] Zhang, W. et al. (2013). Enhancement of perovskite-based solar cells employing core–shell metal nanoparticles. *Nano Lett.*, 13:4505–4510. doi.org/10.1021/nl4024287.

[207] Zollner, S. (Accessed: 26.01.2023a). Optical properties of solids: Lecture 10. Available at pdf on Google search "Optical Properties Lecture 10 Zollner.pdf".

[208] Zollner, S. (Accessed: 26.01.2023b). Optical properties of solids: Lecture 8. Available at pdf on Google search "Optical Properties Lecture 8 Zollner.pdf".

Appendix A

Electron-Phonon Interaction

Here we make a brief summary for describing the e-ph interaction, in the weak regime, called as Fröhlich interaction. The coupling between the LO phonons and the electrons is described according to this interaction. And, as we will see, it will correspond to an attractive force mediating two electrons. In this case, the interaction is long range, that is why we are neglecting the TO phonons due to its smaller electric field. The derivation followed here was extracted from the books of [76], [24] and [29].

We start with the Hamiltonian of an electron interacting with the ions in a lattice, is:

$$H = \frac{p^2}{2m_e^*} + \sum_i \frac{p_i^2}{2m_i^*} + \frac{1}{2}\sum_{ij} V_{\text{ion}}(R_i - R_j) + \sum_i V_{\text{el-ion}}(r - R_i) \tag{A.1}$$

where,

$$H_{\text{el}} = \frac{p^2}{2m_e^*} \tag{A.2}$$

$$H_{\text{ion}} = \sum_i \frac{p_i^2}{2m_i^*} + \frac{1}{2}\sum_{ij} V_{\text{ion}}(R_i - R_j) \tag{A.3}$$

$$H_{\text{el-ion}} = \sum_i V_{\text{el-ion}}(r - R_i) \tag{A.4}$$

Here, the m_e^* and m_i^* denotes the effective mass of the curvature of the bands for electron and ions, respectively. The potential energy term of the ions V_{ion} encloses the electric interaction, H_{ion}^0, of them and their harmonic oscillations, H_{ion}^{ph}. These last term can be written in terms of the boson creation, $\hat{b}_q^\dagger$, and annihilation, $\hat{b}_q$, operators of the longitudinal optical field:

$$H_{\text{ion}}^{ph} = \hbar\omega_{LO}\sum_q \hat{b}_q^\dagger \hat{b}_q. \tag{A.5}$$

On the other hand, the electron-ion interaction can be decomposed in a the Coulomb interaction plus the electron-phonon Hamiltonian, i.e.,

$$\sum_i V_{\text{el-ion}}(r - R_i) = \sum_i V_{\text{el-ion}}(r - (R_i^0 + u_i)) \tag{A.6}$$

$$= \sum_i V_{\text{el-ion}}(r - R_i^0) - \sum_i u_i \cdot \nabla V_{\text{el-ion}}(r - R_i^0) \tag{A.7}$$

$$= H_{\text{el-ion}}^0 + H_{\text{el-ph}} \tag{A.8}$$

These equations show that the interaction of electron and phonons are included in the electron-lattice Hamiltonian. By depicting only the electron and boson terms, we end up with the energy of a system where an electron and the surroundings LO phonons interact:

$$\tilde{H} = \frac{p^2}{2m_e^*} + \sum_q \hbar\omega_{LO}\hat{b}_q\hat{b}_q^\dagger - \sum_i u_i \cdot \nabla V_{\text{el-ion}}(r - R_i^0). \tag{A.9}$$

Now, we start to build the electron-phonon interaction by modeling the last term of equation A.9. We start by writing the displacement of the ions, u_i, in the Fourier representation, i.e.,

$$u_i = \frac{1}{\sqrt{NM}} \sum_q Q_q e^{iq \cdot R_i^0} \hat{e} \tag{A.10}$$

Here the $\hat{e}$ is the unit vector of the polarization. When we quantize the displacement, all quantities become operators, and so we can write $\hat{Q}_q$ in terms of the boson operators:

$$\hat{Q}_q = \left(\frac{\hbar}{2\omega_{LO}}\right)^{\frac{1}{2}} (\hat{b}_q + \hat{b}_q^\dagger) \tag{A.11}$$

So, the displacement field is:

$$u_i = \sum_q \left(\frac{\hbar}{2\omega_{LO}Nm_i^*}\right)^{\frac{1}{2}} (\hat{b}_q + \hat{b}_q^\dagger) e^{iq \cdot R_i^0} \tag{A.12}$$

On the other hand, the term $V_{\text{el-ion}}(r - R_i^0)$ can be expanded in fourier series as:

$$V_{\text{el-ion}}(r - R_i^0) = \frac{e}{4\pi\varepsilon_0} \frac{1}{|r - R_i^0|} = \frac{e}{4\pi\varepsilon_0} \sum_q \frac{4\pi}{q^2} e^{iq \cdot (r - R_i^0)} \tag{A.13}$$

The gradient of this term is easily computed:

$$\nabla V_{\text{el-ion}}(r - R_i^0) = \frac{e}{4\pi\varepsilon_0} \sum_q \frac{4\pi i}{q} e^{iq \cdot (r - R_i^0)} \tag{A.14}$$

So, the electron-phonon interaction will have the form:

$$H_{\text{el-ph}} = -\sum_i u_i \cdot \nabla V_{\text{el-ph}}(r - R_i^0) \tag{A.15}$$

$$= -iF \sum_q \left(\frac{\hbar}{2\omega_{LO}Nm_i^*} \right)^{\frac{1}{2}} \frac{e}{4\pi\varepsilon_0} \frac{4\pi}{q} \left(\hat{b}_q e^{iq \cdot r} + \hat{b}_q^\dagger e^{-iq \cdot r} \right) \tag{A.16}$$

In which the sum over i has been dropped due to the cancellation of the term corresponding to R_i^0 and the effective mass of the ions, m_i^*, is taken as constant. If we look deeply in the last term of eq. (A.16), we can interpret this term as a potential acting on the electron located at r due to the induced phonon polarization. In eq. (A.16) a constant F has been added in order to account for the coupling of electron and phonons. This term can be evaluated from the interaction energy, $e^2/\varepsilon r$, between two electrons in a medium of dielectric constant ε as product of the polarization. For this system, the unperturbed Hamiltonian is the electric interaction between electrons. And the first order perturbation is the couple between electrons and the phonon field which corresponds to our eq. (A.16), i.e., for this system:

$$H^{'}(r_1, r_2) = H_{\text{el-ion}}(r_1) + H_{\text{el-ion}}(r_2) \tag{A.17}$$

However, this term does not give us information about the couple of the two electrons when they exchange a phonon. For this reason, we perform the second order perturbation theory, where the Hamiltonian is:

$$H^{''}(r_1, r_2) = -2 \sum_q \frac{\langle 0| H_{\text{el-ion}}(r_1) |q\rangle \langle q| H_{\text{el-ion}} |0\rangle}{\hbar\omega_{LO}} \tag{A.18}$$

Here, only the terms of mixed product for r_1 and r_2 are considered, since the products of r_1 and r_2 alone correspond to self-energy terms. For this reason a factor of two is included to account for the interchange of r_1 and r_2. In addition, the state $|0\rangle$ is the lowest state for the

phonon field, while the state $|q\rangle$ denote the excited one. The solution of H'' is then:

$$H''(r_1, r_2) = -\frac{\hbar}{\omega_{LO} N m_i^*} \frac{e^2}{(4\pi\varepsilon_0)^2} \frac{16\pi^2 F^2}{\hbar\omega_{LO}} \sum_q \frac{1}{q^2} e^{iq\cdot(r_2-r_1)}, \tag{A.19}$$

$$= -\frac{1}{\omega_{LO}^2 N m_i^*} \frac{e^2}{(4\pi\varepsilon_0)^2} 4\pi F^2 \frac{1}{|r_2-r_1|} \tag{A.20}$$

Here, it is easy to see the attractive nature of this Hamiltonian which is Coulomb like between electrons at r_1 and r_2. This means that when electrons exchange one phonon they feel an attraction. That is why in superconductivity, for the BSC theory, this exchange of phonons is so strong that it will create a quasiparticle known as Cooper pairs. Lastly, the Hamiltonian, H'', corresponds to the difference between the system in mediums of dielectric constant equal to the static one, ε_s (where both the electronic and ionic polarizability contributes), and the high frequency one, ε_∞ (where only electronic is considered), i.e.,

$$H''(r_1, r_2) = \frac{e^2}{4\pi\varepsilon_0}\left(\frac{1}{\xi_s} - \frac{1}{\xi_\infty}\right) \tag{A.21}$$

Here ξ_s and ξ_∞ are the coefficients corresponding to the dielectric constants $\varepsilon_s = 4\pi\varepsilon_0\xi_s$ and $\varepsilon_\infty = 4\pi\varepsilon_0\xi_\infty$, respectively. After equating eq. (A.20) and eq. (A.21), we get the value of F:

$$F = 4\pi\varepsilon_0\omega_{LO}\sqrt{\frac{Nm_i^*}{4\pi\varepsilon_{eff}}}. \tag{A.22}$$

Here, $1/\varepsilon_{eff} = 1/\varepsilon_s - 1/\varepsilon_\infty$. We can finally compute the electron phonon energy, after replacing F on eq. (A.16):

$$H_{\text{el-ph}} = -i\sqrt{\frac{2\pi e^2\hbar\omega_{LO}}{\varepsilon_{eff}}} \sum_q \frac{1}{q}(\hat{b}_q e^{i1\cdot r} + \hat{b}_q^\dagger e^{-iq\cdot r}) \tag{A.23}$$

This electron-phonon interaction will lead us to the Fröhlich coupling constant which can be defined when one perform the number of optical phonons that clothe an electron (phonon population cloud) [76]. The Fröhlich coefficient is:

$$\alpha = \frac{e^2}{\hbar}\left(\frac{m_e^*}{2\hbar\omega_{LO}}\right)^{\frac{1}{2}}\left(\frac{1}{\varepsilon_\infty} - \frac{1}{\varepsilon_s}\right). \tag{A.24}$$

Lets remember that in the Fröhlich theory the considerations taken into account were the large size of the polaron, the non relativistic formulation, the parabolic dispersion of the

band electron and that only LO phonons interact with the electron [24]. This large polaron or "Fröhlich" polaron is characterized by low values of α. In this regime, once the polaron is formed, the binding energy and effective mass of the new quasi-particle can be computed as:

$$E_{pol} = -\alpha\hbar\omega_{LO} \tag{A.25}$$

$$m^*_{pol} = \frac{m^*_e}{1 - \alpha/6} \tag{A.26}$$

Other works developed by Feynmann and Tomonaga give corrections for these terms for $\alpha < 6$.

Appendix B

Deduction of Thermodynamic Quantities

Here we explain the demonstration of the thermal quantities shown in chapter 4.6. We follow the derivation found in the literature of [185, 76]. The study of the vibrational properties of the crystal written in terms of the phonon creation and annihilation operators help us to understand the system when undergoes a thermal evolution. Actually, the partition function of the system, Z, can be computed for the system at equilibrium, i.e.,

$$Z = \Pi_q^{N_q} \Pi_{i=1}^{N_i} e^{-\hbar\omega_i(q)/(2k_\beta T)} \left(\frac{1}{1 - e^{-\hbar\omega_i(q)/(k_\beta T)}} \right). \tag{B.1}$$

Here, q and $\omega_i(q)$ represent the phonon wavevector and frequency, respectively. In addition, the term N_i accounts for the phonon branches in the phonon DOS, and the N_q is the number of wavevector points in a certain direction in the Brillouin zone. With eq. B.1, the Helmholtz free energy can be computed from the statistics [185, 5]:

$$F = -k_\beta T \mathrm{Log}(Z), \tag{B.2}$$

resulting in,

$$F = \sum_q^{N_q} \sum_i^{N_i} \left(\frac{\hbar\omega_i(q)}{2} + k_\beta T \mathrm{Log} \left(1 - e^{-\frac{\hbar\omega_i(q)}{k_\beta T}} \right) \right) \tag{B.3}$$

The first term of eq. B.3 corresponds to the free energy at zero kelvin, while the second is the term arising from the harmonic approximation used to find the phonon energy states. If one wants to include anharmonic terms, a perturbative analysis should be carried as shown in [185].

Now, the thermodynamic quantities such as Internal energy (U), Entropy (S), and Specific Heat at constant volume (C_v) are straightforward derived from the Helmholtz free energy

[185]. For instance, the entropy is:

$$S = -\frac{\partial F}{\partial T}\big|_{V,N},$$

(B.4)

thus,

$$S = k_\beta \sum_q^{N_q} \sum_i^{N_i} \left(\frac{\hbar\omega_i(q)}{k_\beta T} \frac{1}{e^{\hbar\omega_i(q)/(k_\beta T)} - 1} - \text{Log}\left(1 - e^{-\frac{\hbar\omega_i(q)}{k_\beta T}} \right) \right).$$

(B.5)

The internal energy is calculated from:

$$U = F + TS,$$

(B.6)

resulting in,

$$U = \sum_q^{N_q} \sum_i^{N_i} \left(\frac{\hbar\omega_i(q)}{2} + \frac{\hbar\omega_i(q)}{e^{\hbar\omega_i(q)/(k_\beta T)} - 1} \right)$$

(B.7)

Lastly, the specific heat at specific volume is derived from [185, 5]:

$$C_v = \frac{1}{V}\frac{\partial U}{\partial T},$$

(B.8)

$$C_v = \sum_q^{N_q} \sum_i^{N_i} \left(k_\beta \left(\frac{\hbar\omega_i(q)}{k_\beta T} \right)^2 \frac{e^{\hbar\omega_i(q)/(k_\beta T)}}{\left(e^{\hbar\omega_i(q)/(k_\beta T)} - 1 \right)^2} \right)$$

(B.9)

The aforementioned equations can be written in terms of the continuum variable q, i.e., we shall make the change:

$$\sum_q^{N_q} \sum_i^{N_i} \rightarrow \sum_i^{N_i} \int \frac{d^3 q}{(2\pi)^3}$$

(B.10)

Actually, we can transform this integral and sum over the phonon branches in terms of a phonon density of states, i.e., we can pass from the integral over q to a one dependent on ω

$$I = \sum_{i=1}^{N_i} \int \frac{d^3 q}{(2\pi)^3} F(\omega(q)) \rightarrow \int F(\omega) G(\omega) d\omega$$

(B.11)

Here $F(\omega)$ represents the thermodynamic quantities. And, the density of states, $G(\omega)$, is defined as:

$$G(\omega) = \sum_{i=1}^{N_i} \int \frac{d^3}{(2\pi)^3} \delta(\omega - \omega_i(q))$$

(B.12)

This phonon DOS has been modeled by Einstein and Debye. In the Einstein model, all phonon branches are considered to have the same energy. While, Debye modeled it using the the mono-atomic chain of atoms. The Debye's theory is the preferred for studying thermal properties because it provide us with a cutoff energy that closely predicts the behavior of the specific heat. And, despite its simplicity, it give us reliable results for the population of states of the phonons. The Debye DOS is [76]:

$$G(\omega) = 9n\hbar \frac{(\hbar\omega)^2}{(\hbar\omega_D)^3}\Theta(\omega_D - \omega). \tag{B.13}$$

Here n is the number of atoms in the solid, and $\omega_D = k_\beta T_D / \hbar$. As a consequence, we can compute the thermodynamic quantities in terms of the density of states [185, 93], i.e.: The Helmholtz free energy is,

$$F(T) = E_0 + k_\beta T \int_0^{\omega_D} G(\omega) \text{Log}\left(1 - e^{-\frac{\hbar\omega}{k_\beta T}}\right) d\omega, \tag{B.14}$$

with,

$$E_0 = \frac{1}{2}\int G(\omega)\hbar\omega d\omega, \tag{B.15}$$

the entropy of the systems becomes,

$$S(T) = k_\beta \int_0^{\omega_D} \left(\frac{\hbar\omega}{k_\beta T}\right) \frac{G(\omega)}{e^{(\hbar\omega/(k_\beta T))} - 1} - G(\omega) \text{Log}\left(1 - e^{-\frac{\hbar\omega}{k_\beta T}}\right) d\omega, \tag{B.16}$$

the internal energy is,

$$U(T) = E_0 + k_\beta T \int_0^{\omega_D} \left(\frac{\hbar\omega}{k_\beta T}\right) \frac{G(\omega)}{e^{(\hbar\omega/(k_\beta T))} - 1} d\omega, \tag{B.17}$$

and, the specific heat turns in

$$C_v(T) = k_\beta \int G(\omega) \left(\frac{\hbar\omega}{k_\beta T}\right)^2 \frac{e^{\hbar\omega/(k_\beta T)}}{\left(e^{\hbar\omega/(k_\beta T)} - 1\right)^2} d\omega \tag{B.18}$$

$$= 9nk_\beta \left(\frac{T}{\theta_D}\right)^3 \int_0^{\theta_D/T} \frac{x^4 e^x}{(e^x - 1)^2} dx. \tag{B.19}$$

Here x representing the variable $\hbar\omega/(k_\beta T)$.